DISSERTATION

MICROPHYSICAL AND MACROPHYSICAL RESPONSES OF MARINE

STRATOCUMULUS POLLUTED BY UNDERLYING SHIPS

Submitted by

Matthew Wells Christensen

Department of Atmospheric Science

In partial fulfillment of the requirements

For the degree of Doctor of Philosophy

Colorado State University

Fort Collins, Colorado

Summer 2012

Doctoral Committee:

    Advisor: Graeme Stephens

    Christian Kummerow
    Susan C. van den Heever
    Steven Reising

ABSTRACT

MICROPHYSICAL AND MACROPHYSICAL RESPONSES OF MARINE

STRATOCUMULUS POLLUTED BY UNDERLYING SHIPS

Multiple sensors flying in the A-train constellation of satellites were used to determine the extent to which aerosol plumes from ships passing below marine stratocumulus alter the microphysical and macrophysical properties of the clouds. Aerosol plumes generated by ships sometimes influence cloud microphysical properties (effective radius) and, to a largely undetermined extent, cloud macrophysical properties (liquid water path, coverage, depth, precipitation, and longevity). Aerosol indirect effects were brought into focus, using observations from the Cloud-Aerosol Lidar with Orthogonal Polarization (CALIOP) and the 94-GHZ radar onboard CloudSat. To assess local cloud scale responses to aerosol, the locations of over one thousand ship tracks coinciding with the radar were meticulously logged by hand from the Moderate Resolution Imaging Spectroradiometer (MODIS) imagery. MODIS imagery was used to distinguish ship tracks that were embedded in closed, open, and unclassifiable mesoscale cellular cloud structures. The impact of aerosol on the microphysical cloud properties in both the closed and open cell regimes were consistent with the changes predicted by the Twomey hypothesis. For the macrophysical changes, differences in the sign and magnitude of these properties were observed between cloud regimes. The results demonstrate that the spatial extent of rainfall (rain cover fraction) and intensity decrease in the clouds contaminated by the ship plume compared to the ambient pristine clouds. Although reductions of precipitation were common amongst the clouds with detectable

rainfall (72% of cases), a substantial fraction of ship tracks (28% of cases) exhibited the opposite response. The sign and strength of the response was tied to the type of stratocumulus (e.g., closed vs open cells), depth of the boundary layer, and humidity in the free-troposphere.

When closed cellular clouds were identified, liquid water path, drizzle rate, and rain cover fraction (an average relative decrease of 61%) was significantly smaller in the ship-contaminated clouds. Differences in drizzle rate resulted primarily from the reductions in rain cover fraction (i.e., fewer pixels were identified with rain in the clouds polluted by the ship). The opposite occurred in the open cell regime. Ship plumes ingested into this regime resulted in significantly deeper and brighter clouds with higher liquid water amounts and rain rates. Enhanced rain rates (average relative increase of 89%) were primarily due to the changes in intensity (i.e., rain rates on the 1.1 km pixel scale were higher in the ship contaminated clouds) and, to a lesser extent, rain cover fraction. One implication for these differences is that the local aerosol indirect radiative forcing was more than five times larger for ship tracks observed in the open cell regime (-59 W m^{-2}) compared to those identified in the closed cell regime (-12 W m^{-2}). The results presented here underline the need to consider the mesoscale structure of stratocumulus when examining the cloud dynamic response to changes in aerosol concentration.

In the final part of the dissertation, the focus shifted to the climate scale to examine the impact of shipping on the Earth's radiation budget. Two studies were employed, in the first; changes to the radiative properties of boundary layer clouds (i.e., cloud top heights less than 3 km) were examined in response to the substantial decreases

in ship traffic that resulted from the recent world economic recession in 2008. Differences in the annually averaged droplet effective radius and top of atmosphere outgoing shortwave radiative flux between 2007 and 2009 did not manifest as a clear response in the climate system and, was probably masked either due to competing aerosol cloud feedbacks or by interannual climate variability. In the second study, a method was developed to estimate the radiative forcing from shipping by convolving lanes of densely populated ships onto the global distributions of closed and open cell stratocumulus clouds. Closed cells were observed more than twice as often as open cells. Despite the smaller abundance of open cells, a significant portion of the radiaitve forcing from shipping was claimed by this regime. On the whole, the global radiative forcing from ship tracks was small (approximately -0.45 mW m^{-2}) compared to the radiative forcing associated with the atmospheric buildup of anthropogenic CO_2.

ACKNOWLEDGEMENTS

I owe a debt a gratitude to many of the reviewers who diligently read and contributed valuable feedback during the process of publishing. Amongst those, I would like to thank: Rob Wood, Jim Coakley, Bruce Albrecht, and those that remain anonymous.

I would also like to express gratitude to my friends and family who encouraged me to excel in school and pursue my dreams. Most of all, I would like to thank my fiancée Alaina Steiner for her continuous support, compassion, and love, and who made it all worthwhile.

TABLE OF CONTENTS

LIST OF TABLES

LIST OF FIGURES

PART I: INTRODUCTION TO THE DISSERTATION

This dissertation is a compilation of many parts that build together to form a cohesive understanding of the effects of aerosols on the radiative properties of marine stratocumulus clouds. Ship tracks were used to investigate the microphysical and macrophysical responses that shape the sign and strength of the aerosol indirect effect. Physical transformation of marine stratocumulus by the effluents from ships was carefully examined on a case-by-case basis to investigate aspects of the aerosol-cloud problem that cause a great deal of uncertainty in projections of global warming; that is, the cloud albedo and cloud lifetime effects. In the final part of the dissertation, the magnitude of these local scale effects was projected onto the global distributions of ship emissions to determine their significance on the climate scale.

In Part II, the interaction of aerosol effects on cloud depth and albedo was explored using several hundred ship tracks in a region off the west coast of the United States. Care was taken to classify the spatial pattern of stratocumulus corresponding to the domain of each ship track. The Cloud-Aerosol Lidar and Infrared Pathfinder Satellite Observations (CALIPSO) was used to accurately measure the altitude across the tops of ship tracks to test the hypothesis that an increase in the concentration of aerosol leads to cloud deepening. Part II was published in the *Journal of Geophysical Research* (*JGR*) – Atmospheres in the form presented in this dissertation.

In Part III, the role of precipitation in cloud-aerosol interactions was explored using measurements from the CloudSat space-based radar. Due to observing limitations, the characteristics of precipitation could only be assessed from a few of the ship tracks in the database of Part II. Therefore, the number of ship tracks were greatly expanded upon in Part III by locating them in multiple geographic regions spanning several years of

2

observations. This 'painstaking' search yielded the largest database of ship tracks observed using active space-based sensors. The goals of Part III were to answer the following questions: How often is rainfall suppressed in ship tracks? Which clouds are most susceptible to changes in precipitation? Is the precipitation response forced by microphysical or macrophysical changes? Part III will appear in a manuscript that was recently accepted for publication through *JGR – Atmospheres* in the form presented in this dissertation.

In contradiction to the expectation that cloud brightening ought to occur by increasing the concentration of cloud condensation nuclei, the opposite was identified in some ship tracks. Therefore, the goals of Part IV were to determine the potential causes of this effect. To accomplish this, the cloud albedo was inferred from the optical properties derived from MODIS and the data was composited and analyzed by the sign of the cloud albedo response. In addition, in situ observations of ship tracks recently measured in the Eastern Pacific Emitted Aerosol Cloud Experiment (E-PEACE) campaign were incorporated as a means of validating the satellite observations and theory of aerosol-cloud brightening.

Parts II – IV were primarily focused on the local cloud scale interaction of the aerosol with the microphysical and dynamical changes of the clouds. In Part V, the focus shifted to the global scale to estimate the indirect radiative forcing from the emissions of ships and ship tracks. This was achieved using the susceptibilities derived from Parts II—IV for the distributions of closed and open cell stratocumulus clouds. Global distributions of ship emissions and mesoscale stratocumulus cloud types were determined from an Automated Mutual-Assistance Vessel Rescue System (AMVER) ship inventory database

and a cloud type-detecting algorithm, respectively. A convolution of these distributions was performed to provide the first estimate of the global aerosol indirect forcing of ship tracks sorted by cloud type. Ship tracks provide a glimpse at the complex nature of indirect effects on low clouds, the consequences of which reveal that aerosol may have a smaller curbing effect on global warming than that previously estimated in climate models. A summary of the dissertation and implications of these results are discussed in Part VI.

Several key results are presented in this dissertation. First, the increased concentration of cloud condensation nuclei introduced by ships always acts to decrease the size of the cloud droplets when ship tracks are observed. Second, drizzle rate, cloud thickness, and cloud liquid water path rarely remain the same between the polluted and nearby unpolluted clouds and, this response is primarily tied to the mesoscale convection of the stratocumulus clouds (e.g., closed vs open cells). One implication for these differences is that the local aerosol indirect radiative forcing is more than five times larger for ship tracks observed in the open cell regime (-59 W m^{-2}) where, cloud thickness and liquid water paths substantially increase in the polluted clouds compared to those identified in the closed cell regime (-12 W m^{-2}) where, the opposite generally occurred. By integrating the local scale radiative effects over the ensemble of ship tracks that cover the Earth (roughly 0.004%), the strength of the forcing was negligible compared to that due to the buildup of anthropogenic CO_2.

PART II: EVIDENCE OF CLOUD DEEPENING

CHAPTER 1

INTRODUCTION

Observations of ship tracks continue to provide evidence that suggests higher

concentrations of cloud condensation nuclei (CCN) strongly modulate the microphysical,

macrophysical, and radiative properties of marine stratocumulus. Ship tracks are a

phenomenon that provides a unique way of studying aerosol effects on clouds because

the regions of clouds that are heavily contaminated by pollution can be separated from

adjacent regions of clean clouds. Satellite [Coakley and Walsh, 2002], in situ [Durkee et

al., 2000a], and numerical modeling [Ackerman et al., 1995] studies of ship tracks all

confirm Twomey's original hypothesis [Twomey, 1974], whereby increased

concentrations of CCN induce a microphysical response which manifests itself through

an increase in cloud droplet concentration and decrease in cloud droplet size. Because the

total amount of liquid water condensate is shared amongst the additional activated cloud

droplets, the total surface area of the cloud increases, thereby scattering a larger fraction

of sunlight, which subsequently enhances the albedo of the cloud [Twomey, 1974]. A

conceptual diagram illustrating this process in relationship to the emissions from an

oceangoing vessel is shown in Figure 1.1a. Albrecht [1989] pointed out that

microphysical changes to the clouds can lead to macrophysical responses through

increases in cloud liquid water, cloud cover fraction, and cloud lifetime caused by the

suppression of drizzle induced by a less efficient collision coalescence process. To spread

out the additional cloud liquid water that would have been removed due to precipitation,

polluted clouds not only grow in the horizontal extent by increasing cloud cover fraction,

but they can also deepen vertically [Pincus and Baker, 1994] depending on the thermodynamic conditions of the atmosphere [Wood, 2007]. Such an increase in cloud water would result in even more reflective clouds, as well as higher cloud cover fractions, and longer cloud lifetimes, further increasing the indirect forcing (see Figure 1.1b).

In situ observations of ship tracks analyzed from the Monterey Area Ship Track (MAST) and the Marine Stratus/ Stratocumulus Experiment (MASE) experiments found evidence of drizzle reduction in clouds at elevated levels of aerosol number concentration, but concurrent increases in liquid water amounts were not always observed in the ship tracks ([Ferek et al., 2000]; [Lu et al., 2007]). Satellite observations taken from several hundred ship tracks show that clouds polluted by ships generally have smaller liquid water paths compared to nearby uncontaminated clouds ([Coakley and Walsh, 2002]; [Segrin et al., 2007]). Based on the results of large-eddy simulations (LES), Ackerman et al. [2004] attributed the losses in liquid water amounts to the enhanced entrainment of sufficiently dry overlying free-tropospheric air in polluted clouds with smaller droplets (see Figure 1.1c). Even though polluted clouds initially have reduced liquid water amounts, liquid water amounts diminished more rapidly in nearby unpolluted clouds between the morning and afternoon MODIS observations of ship tracks [Christensen et al., 2009], which demonstrates that polluted clouds may indeed have longer lifetimes. Using an LES model of trade wind cumuli, Xue et al. [2008] demonstrated that the enhanced entrainment of dry air could overwhelm the liquid water path to the extent that an opposite macrophysical response occurs wherein liquid water amounts, cloud cover fractions, and cloud depths decrease. The ambiguity of these results

7

demonstrates the need to examine aerosol indirect effects in a range of atmospheric conditions in order to ascertain the cloud macrophysical responses to aerosol.

Ship tracks are linear features formed by the polluted exhaust from oceangoing vessels underlying marine stratus clouds. They frequently occur during the summer months in clouds lower than 1 km [Coakley et al., 2000] capped by a strong temperature inversion. Because the heat and water vapor released from the ship stack rapidly dissipate into the marine boundary layer, the added buoyancy has an insignificant effect on the boundary layer dynamics and cloud microphysics and thus does not contribute to deepening the cloud layer [Hobbs et al., 2000]. During the MAST experiment, evidence of elevated cloud tops in a ship track were observed less than an hour downwind of the Sanko Peace (a merchant vessel) [Taylor and Ackerman, 1999]. Cloud tops along the ship track were elevated 100 m above the surrounding deck of shallow broken clouds (300 m deep). Using a one-dimensional cloud model, Taylor and Ackerman [1999] demonstrated that the elevated cloud layer resulted from the injection of CCN into a collapsed marine boundary layer (longwave cooling at cloud top is insufficient to maintain a well-mixed layer). An increase in cloud droplets in this environment enhanced the longwave cooling at cloud top, which subsequently increased the buoyant forcing enough to deepen the boundary layer in the ship track. The cloud height response from ships was investigated by Segrin et al. [2007] using the passive remote sensor onboard MODIS, where they found no change in cloud top height between the ship tracks and surrounding uncontaminated clouds. This result, however, was likely due to their observations being limited to ship tracks observed in completely overcast conditions where the entrainment of dry air above the boundary layer was presumed to be larger

than that for partly cloudy conditions [Ackerman et al., 2003]. Regions of stratocumulus in which the clouds are broken are often associated with open cellular convection. Because regions of open cells typically have a cloud dynamic and thermodynamic environment very different from nearly overcast closed cell convective clouds [Wood and Hartmann, 2006], the response to aerosol is generally quite different between the two regimes [Wang and Feingold, 2009] and should therefore be accounted for when analyzing aerosol indirect effects.

The purpose of this study is to examine the macrophysical and optical properties of polluted clouds using multiple sensors from the afternoon train (A-Train) constellation of satellites. These observations provide accurate measurements of cloud top height, precipitation rate, and the optical properties of clouds. Ship tracks are examined in both overcast and broken cloudy conditions and composited by atmospheric stability and moisture above the boundary layer in order to account for a wide range of atmospheric conditions which likely contribute differently to the macrophysical responses of polluted and unpolluted clouds. This part of the dissertation examines the differences in cloud top height and optical property responses to aerosol between closed and open cell mesoscale cloud regimes. In Part III of the dissertation, the role of precipitation on the cloud property responses to changing aerosol loading is examined.

a) Indirect effect for clouds with fixed water amounts (cloud albedo effect)
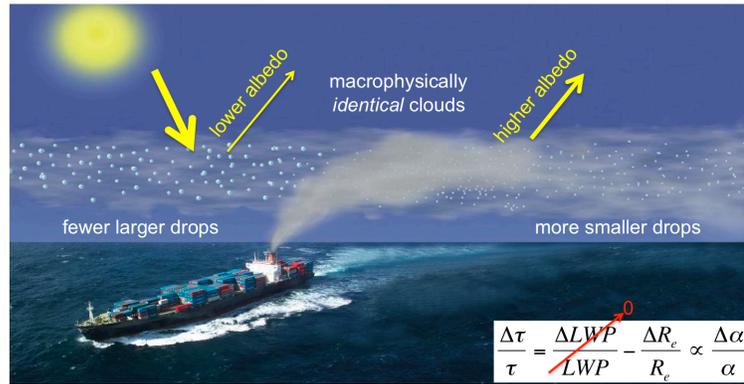
b) Indirect effect for clouds with varying water amounts (cloud lifetime effect)
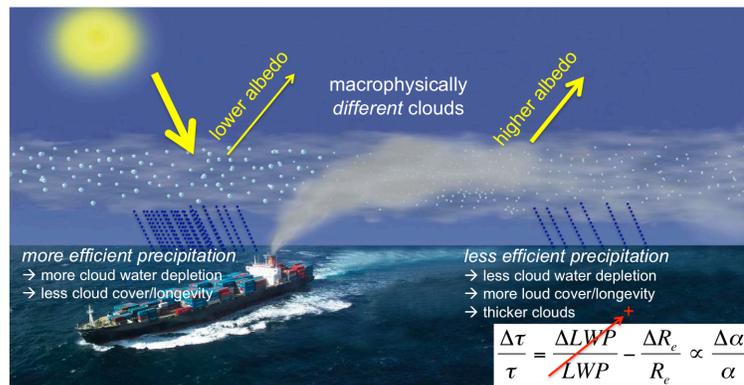
c) Indirect effect for clouds with varying thermodynamic conditions (entrainment effect)
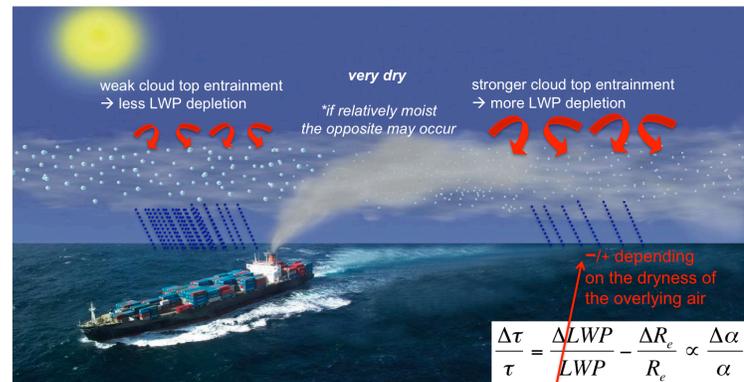
Figure 1.1. Conceptual diagrams illustrating various cloud feedbacks (a – c) associated with increasing the concentration of cloud condensation nuclei from the exhaust plume of an oceangoing vessel. Equation (4) shows how changes in effective radius or liquid water path can influence the strength of the cloud albedo effect. Image was obtained from the NASA website.

CHAPTER 2

DATA AND ANALYSIS PROCEDURES

2.1. Data sources

Cloud top layer height was analyzed for ship tracks and nearby surrounding

clouds using observations from the Cloud-Aerosol Lidar with Orthogonal Polarization

(CALIOP). The observations covered daytime passes off the west coast of North America

20°–60°N and 150°–110°W starting from June 2006 to coincide with the first

observations from CALIOP through December 2008. Ship tracks intersecting the Cloud-

Aerosol Lidar and Infrared Pathfinder Satellite Observations (CALIPSO) orbit were

identified by visual inspection using near infrared moderate resolution imaging

spectroradiometer (MODIS) 1 km imagery from the NASA Aqua satellite. An automated

pixel identification scheme based on the method described by Segrin et al. [2007] was

developed to identify clouds polluted by underlying ships and for selecting nearby

unpolluted clouds as controls (discussed in section 2.2). Polluted and nearby unpolluted

clouds identified from the MODIS 1 km imagery were collocated to the nearest

observations from CALIOP and cloud profiling radar (CRP) on CloudSat. Below 8 km,

CALIOP resolves cloud layers with a vertical resolution of thirty meters sampled along

the orbit every 333 m. Cloud top layer height was obtained from the light detection and

ranging (lidar) level 2 cloud layer product (version 3.01). The selective iterative boundary

location (SIBYL) algorithm [Vaughan et al., 2005] was used to retrieve cloud top layer

heights in this product. The measurement uncertainty in cloud top height assessed using

the SIBYL algorithm was less than ±30 m, which is small compared to the uncertainty

assessed from MODIS cloud top height (±200–300 m [Wood and Bretherton, 2004]).

Cloud effective radius, cloud optical thickness, and liquid water path analyzed at a 1 km

horizontal resolution were obtained from the MODIS cloud layer product (MYD06).

Vertical profiles of temperature, specific humidity, and pressure were obtained from the

ECMWF-AUX product collocated to the CloudSat orbit.

The atmospheric environment is defined from the ECMWF analysis in terms of

composites of lower troposphere stability (LTS) and the amount of moisture above the

boundary layer. Lower troposphere static stability was calculated by taking the difference

in potential temperature between the surface and 700 hpa ($LTS = \theta_{700} - \theta_{sfc}$). Moisture

above the boundary layer was calculated by averaging the dewpoint depression

measurements in the profile derived from the ECMWF product from the top of the

temperature inversion to 700 hpa (typically 3 – 5 samples make up the average). The base

of the inversion was determined as the height above mean sea level where the

temperature lapse rate between vertical bins (240 m) maximized between the surface and

700 hpa. Once the base of the inversion was determined, the top of the inversion was

simply identified as the height where the maximum air temperature occurred in the

profile.

Figure 2.1 (left) is a vertical cross section of the attenuated backscatter at 532 nm

across a ship track obtained from the level 1 backscattered lidar data obtained from

CALIOP and projected onto a two-dimensional MODIS infrared image. The image

clearly shows that, where ship tracks are present, the cloud layer is elevated in height

compared to the surrounding clouds. This provides evidence that clouds contaminated by

the aerosol plumes from ships can induce a macrophysical response that manifests as deeper clouds. By contrast, the ship tracks in Figure 2.1 (right) do not appear to be elevated above the ambient clouds. In order to understand why the cloud tops were elevated in response to the ship plume in Figure 2.1 (left) and not in Figure 2.1 (right), several hundred ship tracks were 'painstakingly' logged-by-hand to provide a sufficient number of cases to analyze the response under a wide range of meteorological conditions.
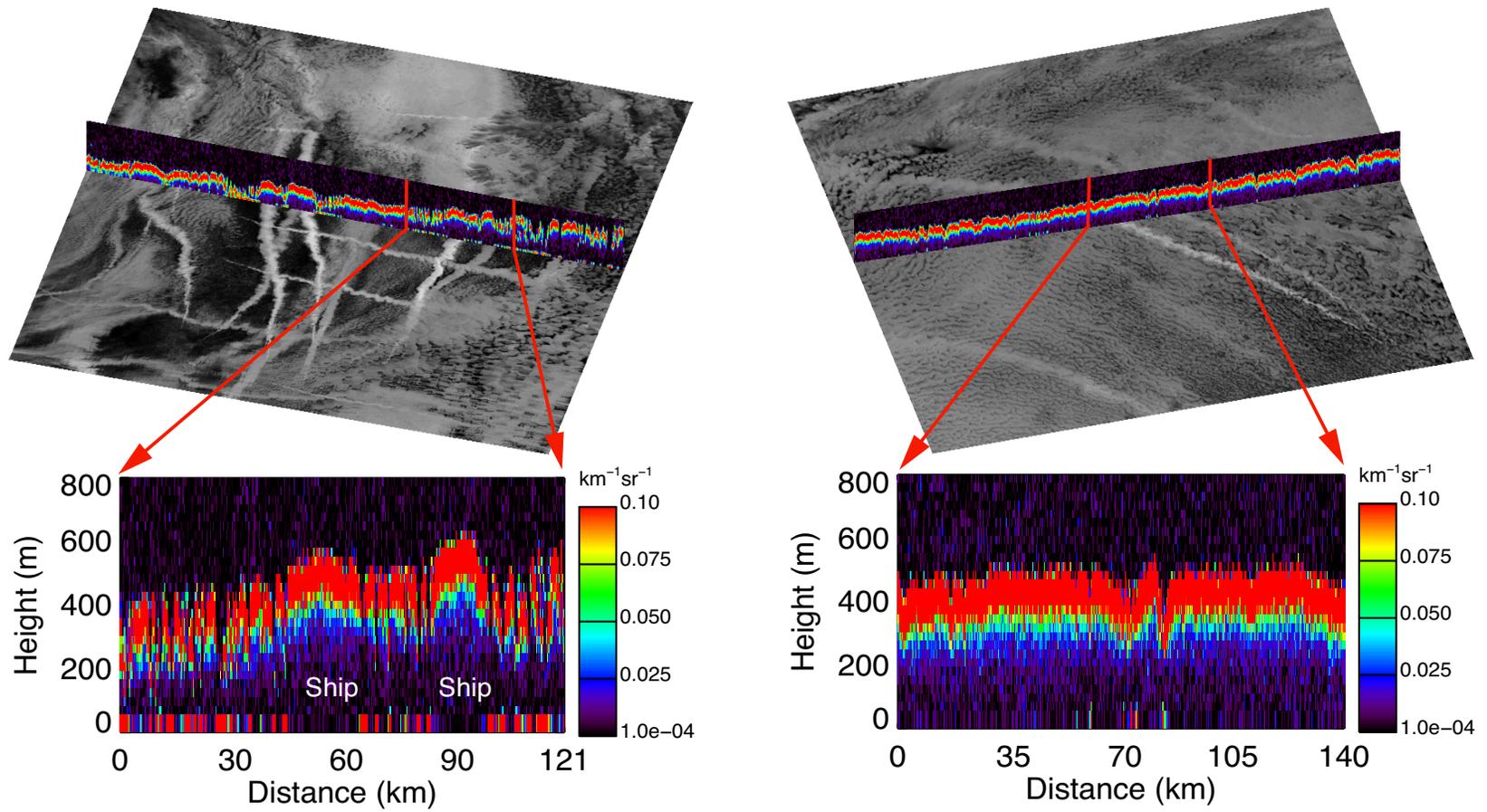
Figure 2.1. Vertical cross section of the attenuated backscatter at 532 nm obtained from the CALIOP projected onto a two-dimensional MODIS 2.1-μm image off the west coast of the United States on (left) 8 August 2007 at 2255 UTC and (right) 23 August 2007 at 2215 UTC.

2.2. Ship track identification

The protocols used for identifying ship tracks were the same as those described by Coakley and Walsh [2002]. Ship track were used if they had a well-defined head (the start of the source region nearest the ship) and remained intact from the head through the intersection with the CALIPSO orbit. Because gravity waves in the marine boundary layer can often take the appearance and be disguised as ship tracks, a discernible head was required so as to not mistake ship tracks with gravity waves [Coakley and Walsh, 2002]. Sometimes ship tracks appear discontinuous or broken (especially in open cell convection) near the boundaries of cloud cells. Cases in which the CALIOP observations fell on the edges or between cloud cells where the air was cloud-free were typically not analyzed due to failures in the automated pixel identification scheme caused by the lack of signal-to-noise from the retrieved radiances. However, if the retrievals succeeded and the overall shape the ship track remained intact despite discontinuities at mesoscale lengths (less than ~50 km) caused by the cellular structure, it was used in the analysis. An additional criterion was established to ensure that the controls from an identified ship track were not contaminated by nearby ship plumes. Because ship vessel traffic often follows similar trajectories, the concentrations of ship tracks can be dense at times. Therefore, in order to ensure that the pollution plume from adjacent ship tracks did not contaminate the controls, cases were removed if the controls from one ship track were placed over a nearby ship track.

Microphysical and macrophysical responses of the clouds were investigated by cloud type. The cloud type distinction was used because large differences typically exist in the cloud properties between open and closed cell clouds [Wood and Hartmann, 2006].

Distinguishing the cloud regime provides two distinct and separate environments to analyze the aerosol indirect effect. The mesoscale cellular cloud structure in which ship tracks were embedded was identified as either closed, open, or undefined. While stratocumulus cloud features encompass many types, only ship tracks found in a closed or open cellular mesoscale environment were used for analysis. Figure 2.2 demonstrates the differences between ship tracks embedded in closed (left) and open cell convective clouds (Figure 2.2, right). The image was constructed from MODIS 1 km visible (0.64 μm) reflectances with the 3.7 μm reflected radiances displayed over the visible image to increase the contrast between the ship tracks and surrounding clouds. Determination of the cloud type was distinguished through subjective analysis of MODIS visible imagery. The cloud regime was distinguished as closed cell if the cloud cover fraction was relatively high (i.e., the cloud cover fraction was higher than 0.9) and consistent over a 100 km^2 region in which the clouds had a honeycomb or hexagonal like pattern with the brightest part of the cloud being in the center of the cell surrounded by cloud-free or darker cloudy edges. In contrast, the cloud regime was identified as open cell if the region had relatively low cloud cover fraction with narrow cell walls separated by large regions of honeycomb like cloud-free air. Regions of clouds that exhibited a mixture of both cloud types or did not hold to these descriptions were flagged as undefined.

The automated detection scheme used for identifying polluted and nearby unpolluted pixels was based primarily on the procedures described by Segrin et al. [2007]. The detection scheme used by Segrin et al. [2007] was modified due to the constraints imposed by the orientation of 1 km MODIS pixels along the CALIOP orbit with respect to the ship tracks. Figure 2.3 demonstrates the procedure used to identify

16

pixels comprising polluted (ship track) and nearby unpolluted clouds. Ship tracks were first identified by visually inspecting MODIS near infrared images in regions where the CALIOP observations (yellow line) coincided with ship tracks. Because ship tracks stand out from the ambient clouds at near infrared wavelengths [Coakley et al., 1987], MODIS radiances at 2.1 and 3.7 μm were used to detect polluted (Ship) and unpolluted (Controls) clouds. Pixels that were polluted (Figure 2.3, red line) by the ships exhaust were obtained using a simple threshold test of the near infrared radiances. The radiances spanned 100 km domains centered over each ship track along pixels coincident with the CALIPSO orbit (Figure 2.3, pink box). Since the average width of a ship track is approximately 9 ± 5 km [Durkee et al., 2000b], the size of the domain was chosen to span very wide or highly tilted ship tracks with respect to the CALIPSO orbital path. Figure 2.3b shows a linear least squares fit (solid line) to the pixel radiances from the domain shown in Figure 2.3a. The fit was used to adjust for gradients in the background noise while pixel radiances that stood out more than three standard deviations above this fit (Figure 2.3b, dashed line) were found to be polluted by the underlying ship. The center of each ship track was identified through visual inspection while the sides (defining its width) were automatically detected by comparing the measured radiance along the domain until the radiance fell 3 standard deviations below the least squares fit line. Single 1 km MODIS pixels on the sides of each ship track were removed to prevent any contamination of partially polluted pixels. The unpolluted clouds that serve as controls for the analysis were then selected by overlaying the width above and below the sides of the ship track. This method ensured that the width of each control (Figure 2.3a, blue and green lines) was equal to the width of the ship track (Figure 2.3a, red line) with the controls being

separated by two MODIS pixels and having the same number of observations as in the ship track.

After the automated detection scheme successfully identified the pixels comprising each ship track, cloud top height measurements from CALIOP were collocated to the MODIS pixels defining the location of the ship track. Figure 2.3c shows coincident observations of cloud top height measured from CALIOP (Figure 2.3c, solid line and pluses for the retrievals used in the analysis) corresponding to the polluted (Ship) and unpolluted (Control 1 and Control 2) cloudy regions as identified in the MODIS imagery (Figure 2.3a). CALIOP observations were screened to include only single-layer clouds below 2 km. In this example, it is clear that the clouds contaminated by the ship are on average higher than the surrounding unpolluted clouds by approximately 160 m. Also, this example demonstrates the structural changes associated with the ship track, which is reflected by the variability in cloud top height in the ship track compared to the surroundings.

To produce representative averages of the cloud optical properties derived from MODIS, a sufficient number of pixels were needed for each ship track. Figure 2.3d shows groupings of polluted (red) and nearby unpolluted (blue and green) cloudy pixels along a 20 km portion of the ship track using the automated pixel identification scheme. Segments were centered over each ship track and were included in the analysis if they contained at least twenty 1 km pixels that were identified as containing polluted clouds and at least twenty pixels from either side of the ship track that were identified as containing unpolluted clouds. MODIS pixels were screened using MYD06 to include only single-layer (cloud multilayer flag = 1) low-level (cloud top pressure greater than

18

500 hpa) warm clouds (cloud top temperature greater than 273 K). Unfortunately, the cloud cover fraction obtained from MYD06 used a coarser resolution (5 km) than the cloud optical property retrievals (1 km pixel scale). As a consequence, changes in cloud amount caused by the ship could not be resolved in this study and larger domains were substituted instead to assess the cloud cover fraction averaged over 100×100 km square regions (depicted by the pink box in Figure 2.3a).

In the current study, cloud droplet radii and liquid water paths were derived using the 3.7 μm reflectances. Absorption by water droplets is greater at 3.7 μm than at the 2.1 μm channel used to retrieve droplet radii. The stronger absorption decreases the mean-free paths of photons in the clouds [Platnick, 2000], thereby reducing the likelihood that the observed radiances would be as strongly affected by 3D cloud effects such as photon leakage through the sides of clouds.

In total 432, ship tracks were identified off the west coast of North America occurring in the period from June 2006 through December 2008 through the visual inspection of MODIS infrared imagery at intersections with the CALIPSO orbit. After screening pixels for single layer low-level warm water clouds and contamination by adjacent ship tracks, 318 ship tracks were deemed suitable for the analysis. Thus, screening removed about one quarter of the ship track cases from the analysis. From the screened data, 132 ship tracks were identified in closed cellular clouds while 36 ship tracks were identified in open cellular clouds with the rest of the ship tracks falling into an undefined cloud regime. Because ship tracks were only observed along the nadir viewed CALIPSO orbit, the higher occurrence of ship tracks in closed cellular clouds may not necessarily reflect physical mechanisms aiding to the production of ship tracks

19

in these environments. A significantly larger database would likely be required in order to determine the favorable mesoscale cloud regime for ship track formation. Such a database is currently under construction.
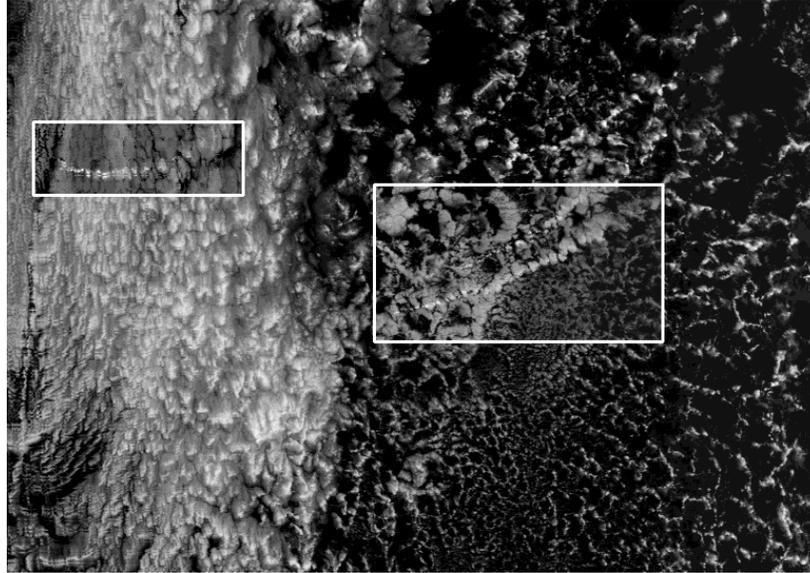
Figure 2.2. Image constructed from the MODIS 0.64 μm channel with outlined sections of the 3.7 μm reflected radiances in regions with ship tracks. The image was taken on 6 May 2007 at 2240 UTC. Closed cellular convective clouds are primarily located on the left-hand side of the image while open cell convective clouds are primarily located on the right-hand side of the image. A region containing a mixture of closed and open cells is considered undefined.

a)

b)

c)

d)

e)

10   R_e (3.7 μm)   25
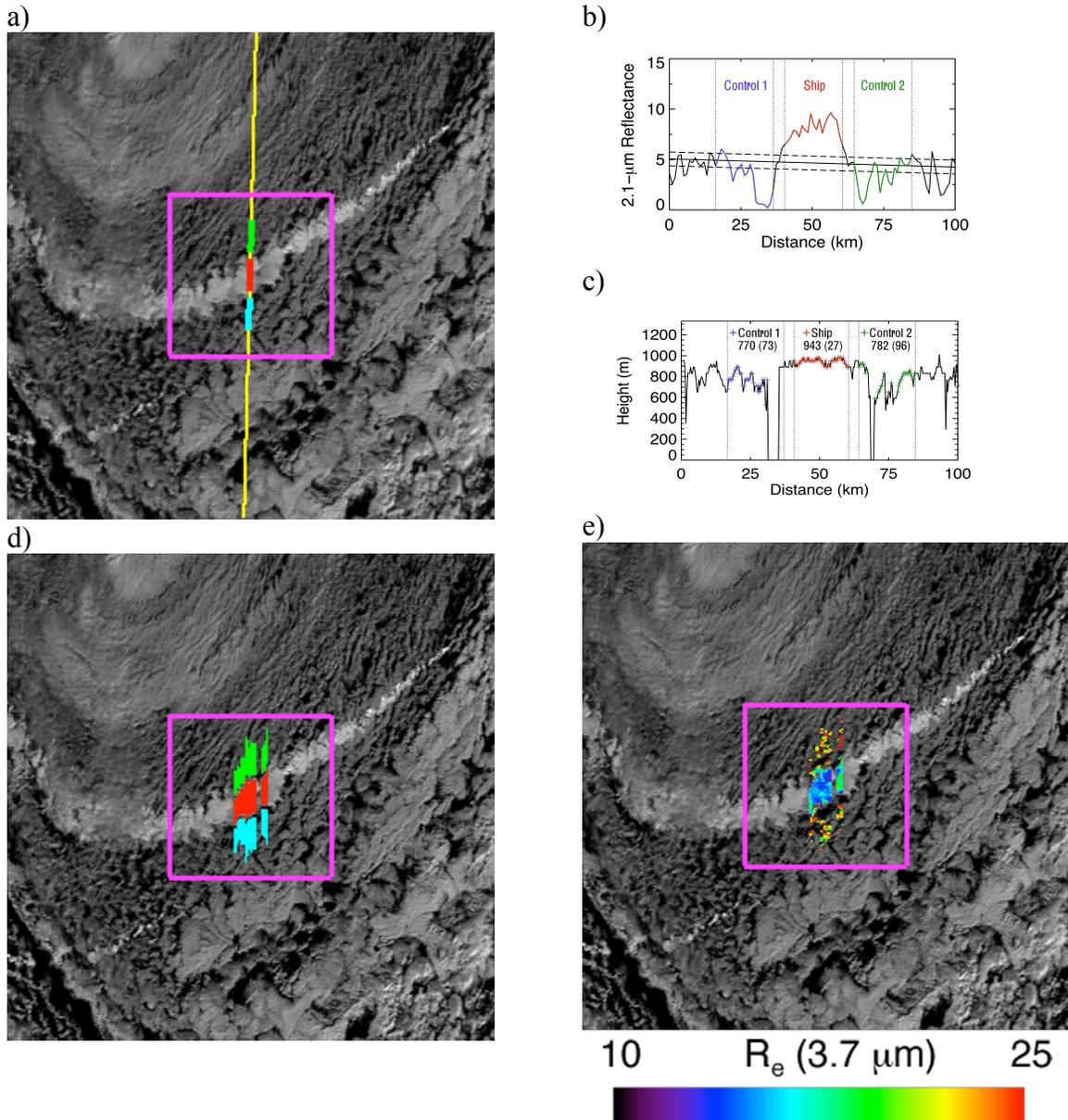
Figure 2.3. (a) The red solid line represents pixels that were contaminated by the ship, and the blue and green lines represent pixels that were uncontaminated and coincident with the observations from CALIOP (yellow line). (b) Ship and control pixels were obtained from a 3 standard deviation threshold test: the solid line gives the trend in the background 2.1 μm reflectance, and the dashed lines are displaced from the best fit trend by plus and minus 3 standard deviations. (c) The pluses represent cloud top height estimates from CALIOP for the polluted (Ship) and unpolluted (Control 1 and Control 2) clouds. Means and standard deviations are given. (d) Shaded regions are the identified polluted (red) and unpolluted (blue and green) pixels along a 20 km wide section of the ship track. (e) Droplet effective radii retrieved using 3.7 μm radiances for the identified pixels composing the segment.

CHAPTER 3

RESULTS

3.1. *Cloud top height responses*

Cloud top altitude measurements from CALIOP were averaged for the clouds contaminated by ships (containing at least two measurements) and for the ambient clean clouds (containing at least two measurements from each control). Nearly all of the observations in the open cell regime were of polluted clouds with higher cloud tops than nearby unpolluted clouds, each with a statistical significance above the 95th percentile. Aerosol from ship plumes increase cloud top heights by 16% in the open cellular regime (from CON = 835 m to SHIP = 966 m), while in the closed cellular regime the changes were statistically insignificant (from CON = 783 m to SHIP = 789 m). These comparisons provide physical evidence that aerosol plumes from ships induce a macrophysical response to marine stratocumulus clouds by increasing their height. However, the magnitude of this response will be shown to depend on the mesoscale organization of the clouds, atmospheric stability, and, to a lesser extent, the amount of moisture in the free troposphere.

Figure 3.1 shows the difference in mean cloud top height between the polluted (SHIP) and unpolluted (CON) clouds as a function of lower troposphere stability (Figure 3.1, left), dewpoint depression (Figure 3.1, middle), and regional cloud cover fraction (Figure 3.1, right) for ship tracks identified in closed (×) and open (squares) cellular regimes; the undefined regime is not shown. As the atmospheric stability increased, the height differences between the polluted and unpolluted clouds decreased. This response

was likely due to the suppression of vertical cloud development caused by a stronger temperature inversion as the stability increased regardless whether the clouds were polluted. As the atmosphere became increasingly unstable (decreasing the LTS), height differences between the polluted and unpolluted clouds increased. This increase primarily occurred when ship tracks were identified in an open cellular regime. The correlation coefficient for the open cell cases in Figure 3.1 (left) was −0.5 and the regression (change in cloud top height with LTS) was statistically significant at the 99th percentile. As the moisture above the inversion increased (smaller dew point depressions), differences between the polluted and unpolluted cloud top heights increased marginally. While the open cellular clouds in Figures 3.1 (left) and 3.1 (middle) generally resided in an unstable and moist atmosphere, closed cellular clouds appear to span all levels of stability and free-tropospheric moisture. Interestingly, the cloud height response almost exclusively arose for polluted clouds identified in the open cellular regime. Observations of closed cells at low stability may indicate errors in the stability calculated from the coarse vertical resolution data in the ECMWF model data over the oceans or because the observations were instantaneous shots and may have been caught during a transition (either decaying or developing) to an open cell regime.

As regional cloud cover fraction increased, the cloud top height response decreased. This response may have arose because the regionally averaged cloud top radiative cooling intensifies as cloud coverage increases thereby sharpening the temperature inversion and preventing strong gradients in cloud top altitude. Consistent with the findings from Segrin et al. [2007], differences in cloud top height between the polluted and unpolluted clouds were insignificant when observed in overcast conditions

(closed cell regime). In partly cloudy conditions (open cell regime), clouds polluted by underlying ships frequently exhibited elevated cloud tops compared to the surrounding unpolluted clouds. As a result, open cell clouds in the more unstable and moist atmosphere were likely more susceptible to changes in cloud height by aerosol loading compared to closed cell clouds.

Tests were performed to ensure that the cloud top height response was caused solely by the underlying ships. Table 3.1 lists the means and standard errors of the means for the differences in cloud top height between each control and between the ship and combined controls. In the closed cell regime, differences in cloud top height between the controls was just as large as that between the ship and controls. However, in the open cell regime, the height response caused by the ship was four times larger than that between the controls. Evidently, ships underlying open cellular clouds increase the cloud top height significantly above the background noise in cloud top altitude. Further tests were performed to investigate the structural differences in cloud top height between ship tracks and the control clouds by assessing the variability in cloud top altitude between them. Table 3.1 also lists the average standard deviation from the ensembles of the polluted and unpolluted clouds for each regime. In the closed cell regime, the variability in cloud top altitude was roughly constant (less than the height of one vertical bin measured by CALIOP) across the cloud deck regardless if underlying ships were present. In the open cell regime, the variability in cloud top height was much larger across the cloud deck except in the clouds contaminated by the underlying ship. Changes in the cloud top height variance associated with the ship suggest changes to the horizontal and vertical extents of the clouds, a phenomenon also identified in numerical simulations of ship

tracks in open cell environments [Wang and Feingold, 2009]. The structural changes associated with ship tracks became more pronounced as the regional cloud cover fraction decreased (not shown), which suggests that the plumes from ships increased horizontal and vertical cloud coverage (an example of this can be seen Figure 2.3c).

3.2. Cloud optical property responses

In order to understand why open cellular clouds were more susceptible to the effects of aerosol on cloud height, both microphysical and macrophysical changes in response to aerosol were examined using the cloud optical properties derived from MODIS. Figure 3.2 shows the change in droplet effective radii, cloud visible optical depths, and liquid water amounts for the closed (solid line) and open cell regimes (dashed line). Table 3.2 lists the means and standard deviations of the cloud properties calculated from the ensembles of ship tracks examined in the closed and open cell regimes. Also shown in the table are the means and standard errors of the means for the differences between the polluted and unpolluted clouds (Ship – Controls). Here, the number of observations was reduced from 132 to 128 in the closed cell regime and from 36 to 34 in the open cell regime by the additional requirements imposed by the collection of MODIS derived cloud properties.

Droplet effective radius was smaller in polluted clouds for both the closed and open cell cloud regimes. Ships underlying open cellular clouds decreased the average size of the droplets nearly two times more than in the closed cell regime. In addition, the open cell clouds unaffected by the ship were observed to have larger cloud droplets compared

to the unaffected clouds in the closed cell regime. Lower concentrations of CCN have readily been observed in regions of open cells adjacent to closed cells [Stevens et al., 2005; Wood et al., 2008]. Larger and fewer cloud droplets in open cells likely arose from less competition for vapor from reduced concentrations of activated drops as a result of the smaller concentrations of CCN. Consequently, open cell clouds were likely more susceptible to a microphysical response from increasing aerosol, as discussed by Platnick and Twomey [1994], than closed cell clouds.

Opposite liquid water path responses in ship tracks occurred depending on the mesoscale convective environment in which they were observed. Liquid water paths were smaller in the polluted clouds by 6% in the closed cell regime (this result was not statistically significant), while in the open cell regime they were significantly larger by 39% than in the unpolluted clouds. Smaller liquid water amounts in ship tracks embedded in overcast conditions (closed cells; here) have been observed in multiple ship track studies [Coakley and Walsh, 2002; Segrin et al., 2007; Christensen et al., 2009] and the cause has been deduced to result from the enhanced entrainment of dry air caused by the smaller droplets in the polluted clouds [Ackerman et al., 2004]. Optical depths increased in the polluted clouds compared to unpolluted clouds for both the closed and open cell regimes, and the increases were more than four times larger in the open cell regime. The larger optical depth and liquid water path responses in the open cell regime were most likely exaggerated due to biases in the retrieved cloud properties stemming from differences in the pixel-scale cloud coverage between polluted and unpolluted clouds. Partly cloudy pixel retrievals applied to MODIS 1 km pixels [Coakley et al., 2005; Segrin et al., 2007] reveal that ship tracks found in regions of broken marine stratus generally

27

have greater pixel-scale cloud cover than do the surrounding unpolluted clouds. A classic

example of this phenomenon is the ship track that transects a region of broken clouds and

then enters an otherwise cloud-free region where the surrounding clouds are no longer

able to survive [Scorer, 1987]. Because of the greater pixel-scale cloud cover, the

polluted clouds generally have larger optical depths and liquid water amounts than do the

surrounding broken clouds. These pixel-scale differences reflect observations at regional

scales. Pixels in 50-km-scale regions overcast by marine stratus have larger optical

depths than do the overcast pixels in regions where the stratus layer has breaks [Hayes et

al., 2010]. Since cloud albedo is proportional to cloud optical depth (shown in section

3.3), the largest impact on the reflected shortwave radiation to space arose from polluted

clouds in an open cell regime where the ship stood a better chance of increasing the pixel-

scale cloud cover fraction.

3.3. Implications for aerosol indirect forcing

How do the microphysical changes to the fractional change in albedo compare

with the macrophysical changes in response to underlying ships? Based on the Eddington

approximation for a nonabsorbing medium cloud albedo is approximately given by [e.g.,

Stephens, 1994, equation 6.59a]

$$\alpha_C = \frac{(1-g)\tau_c}{2 + (1-g)\tau_c} \, , \qquad\qquad (1)$$

where α_c is the cloud albedo, τ_c is the cloud optical depth, and g is the asymmetry parameter, which for warm clouds is equal to ~0.85. The change in cloud albedo ($\Delta\alpha_c$) simply follows from (1) as

$$\frac{\Delta\alpha_C}{\alpha_c} = (1 - \alpha_c)\frac{\Delta\tau_C}{\tau_c}, \tag{2}$$

where the change in cloud albedo between the polluted and unpolluted clouds was estimated to be 0.03 and 0.15 for the closed and open cell regimes, respectively. These changes in cloud albedo for the overcast conditions (closed cell regime) were the same as those given by Segrin et al. [2007]. The backscattered radiative flux at the top of the atmosphere from the polluted clouds was estimated to be 12 W m^{-2} larger in the closed cell regime and 59 W m^{-2} larger in the open cell regime than the flux estimated from the unpolluted clouds. This assumes an incident solar flux of 400 W m^{-2}, which is a typical value of the daily mean insolation during the summer months for this region. This range in the aerosol indirect forcing estimated from ship tracks is consistent and within the range found by Schreier et al. [2007]. Since the change in cloud albedo is related to the fractional change in optical depth (2), the fractional change in optical depth can be derived from [Stephens, 1978]

$$\tau_c = \frac{3}{2}\frac{LWP}{\rho_l R_e}, \tag{3}$$

where LWP is the liquid water path, R_e is the effective radius, and ρ_l is the density of water. The fractional change in optical depth follows (3) as

$$\frac{\Delta\tau_c}{\tau_c} = -\left(\frac{\Delta R_e}{R_e} - \frac{\Delta LWP}{LWP}\right) \propto \frac{\Delta\alpha_c}{\alpha_c}, \tag{4}$$

where (4) relates the microphysical $\left(\dfrac{\Delta R_e}{R_e} \right)$ and the macrophysical $\left(\dfrac{\Delta LWP}{LWP} \right)$ terms to the

fractional change in cloud optical depth, which is proportional to the fractional change in

cloud albedo. In the closed cell cloud regime, the fractional change in effective radius and

liquid water path was −0.18 and −0.06, respectively; thus, the contribution to changes in

cloud albedo by aerosol primarily derived from microphysical changes as Twomey

hypothesized for these cloud conditions. In the open cell cloud regime, the fractional

change in effective radius and liquid water path was −0.22 and +0.39, respectively; thus,

macrophysical changes contributed more to the changes in cloud albedo caused by the

ship. Interestingly, the contributions from the fractional change in effective radius and

liquid water path summed to equal the fractional change in optical depth defined by (4)

for the closed cell regime. The unbalanced equation suggests that there is a residual bias

in the retrieved cloud optical properties that could contribute to either the effective radius

or liquid water path fractional changes. The residual bias in the open cell regime was

0.22, which is roughly the same magnitude as the $\left(\dfrac{\Delta R_e}{R_e} \right)$ and $\left(\dfrac{\Delta LWP}{LWP} \right)$ terms. Consistent

with Hayes et al. [2010], the cloud property biases were found to be strongly correlated

with cloud cover fraction with larger residual biases as regional cloud cover fraction

decreased. This result also suggests that the 3D structure of the clouds might be a source

of bias for the cloud optical properties [Marshak et al., 2006] in the open cell regime,

while in the closed cell regime the optical properties were largely unbiased to the same

extent because the clouds closely resembled plane parallel clouds. Despite the biases

attributed to 3D effects and pixel-scale differences in cloud cover fraction, macrophysical

changes to the clouds potentially contribute just as much to the fractional change in cloud albedo as the microphysical changes due to aerosol plumes emitted from ships.

Because ship tracks were identified in multiple seasons, tests were performed to ensure that the differences between the polluted and unpolluted cloud properties were not biased by seasonal variability. The root mean square differences in the cloud properties between seasons were less than half of the differences found between the polluted and unpolluted clouds. Wintertime clouds were on average more than 400 m higher than summertime clouds, which is consistent with the results found by Lin et al. [2009] for the same region analyzed here. However, the differences in cloud height (between ship and controls) between winter ($\Delta h = 12$ m) and summer ($\Delta h = 18$ m) were much smaller than the changes in cloud height due to the aerosol plume in the open cell regime ($\Delta h = 131$ m). As a result, the impact of underlying ships on the cloud properties between seasons was deemed to be small in comparison with differences in the cloud properties between the polluted and unpolluted clouds reported here.

Table 3.1. Cloud top altitude statistics[a]

	Closed Cell Clouds	Open Cell Clouds
CON1 – CON2 (m)	5(3)	40(30)
SHIP-CONS (m)	5(2)	131(15)
σ_{SHIP} (m)	17	51
σ_{CONS} (m)	25	128

[a]Listed are the means and standard errors of the means for the differences in cloud top height between each control (CON1 – CON2) and between the ship and combined controls (SHIP – CONS). Also listed is the ensemble average standard deviation for the polluted (σ_{SHIP}) and unpolluted clouds (σ_{CONS}).

Table 3.2. Comparisons between closed and open cell cloud properties[a]

	Closed Cell Clouds			Open Cell Clouds		
	Ship	Controls	Ship-Controls	Ship	Controls	Ship-Controls
R_e (3.7 μm)	10.2 (1.9)	12.3 (2.8)	−2.2 (0.1)	14.8 (2.9)	18.9 (3.3)	−4.1 (0.5)
3.7-μm LWP (g m^{-2})	99 (55)	106 (63)	−6 (2)	145 (66)	104 (42)	41 (10)
Optical Depth	14.0 (5.9)	12.4 (6.0)	1.6 (0.2)	14.3 (5.4)	7.8 (2.7)	6.5 (0.9)
Cloud Top Height (m)	789 (254)	783 (256)	5 (2.0)	966 (285)	835 (262)	131 (15)

[a]Listed are the means and standard deviations of *Ship* and *Controls* and the means and standard errors of the means for *Ship – Controls* for droplet effective radius (R_e (3.7 μm)), liquid water path (3.7-μm LWP (g m^{-2})), visible cloud optical depth, and cloud top height (measured by CALIOP). Standard deviations and standard errors of the mean are given in parentheses.
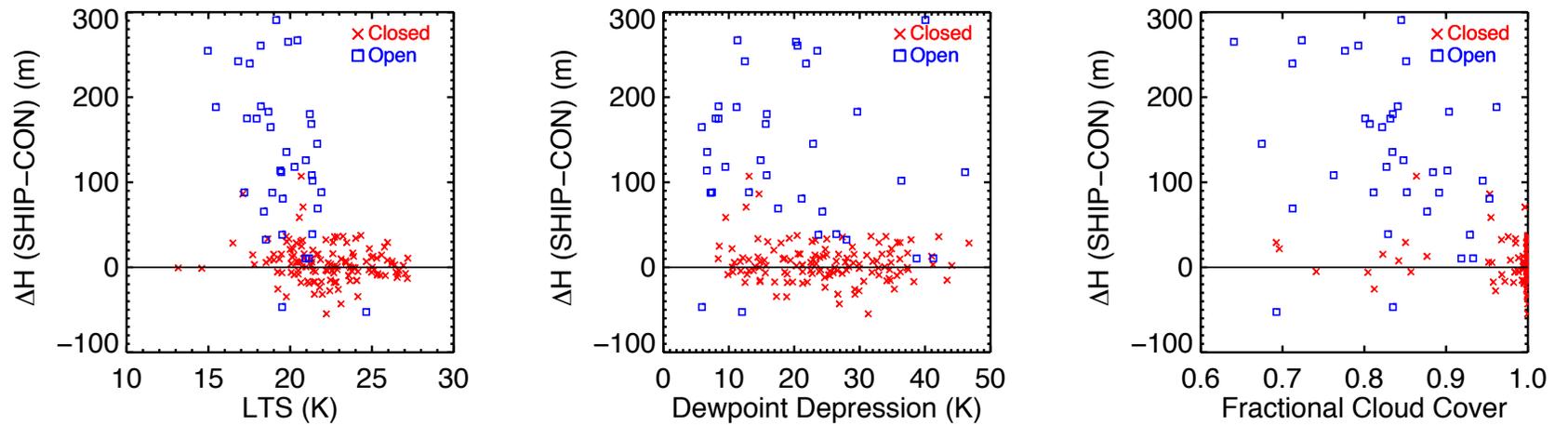
Figure. 3.1. Differences in mean cloud top height derived from CALIOP between polluted and unpolluted clouds (*SHIP − CON)* plotted against (left) lower troposphere stability (LTS), (middle) dewpoint depression, and (right) fractional cloud cover with 132 ship tracks identified in the closed cell regime and 36 ship tracks identified in the open cell regime.
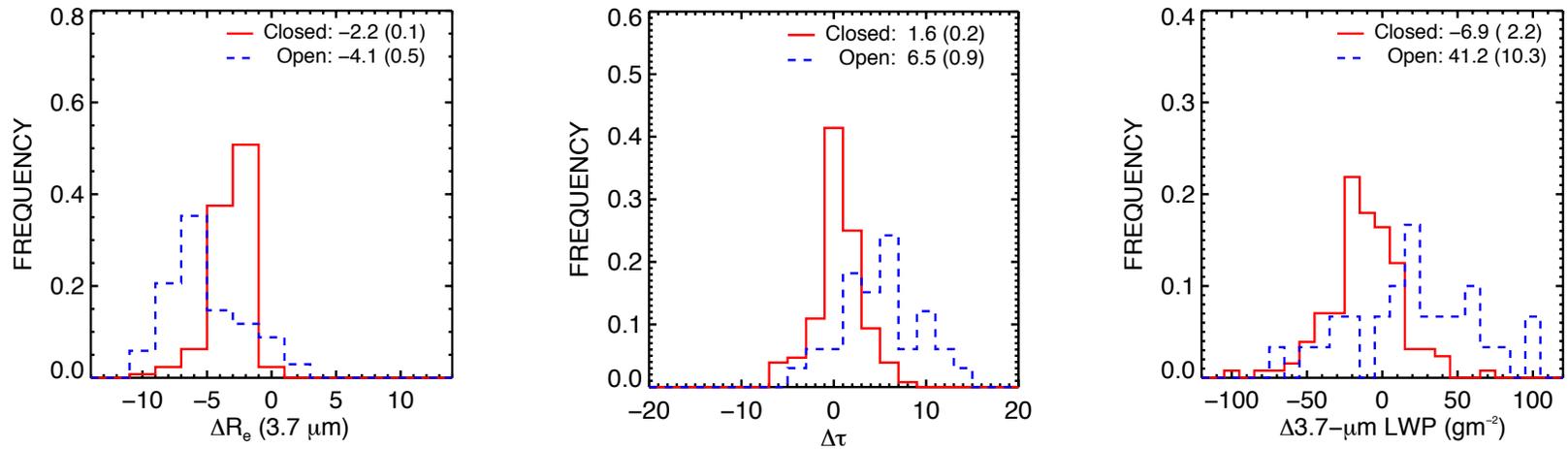
Figure. 3.2. Differences in (left) droplet radii ΔR_e, (middle) cloud optical depths $\Delta\tau$, and (right) liquid water paths ΔLWP between the polluted and unpolluted clouds. The ensemble consists of 128 observations in which ship tracks were identified in a closed cell regime (solid red line) and 34 observations for which they were identified in an open cell regime (blue dashed line). Means and standard errors of the means are given.

CHAPTER 4

CONCLUSIONS

Ship tracks continue to provide essential clues for unlocking the mysteries of particle pollution on clouds. The analysis described in this study spanned two years of ship track observations (June 2006 – December 2008) off the West Coast of the United States. By making use of the CALIOP on CALIPSO and the MODIS on Aqua, highly accurate measurements of cloud top height and the optical properties of clouds were used to examine the microphysical and macrophysical changes to marine boundary layer clouds polluted by underlying ships. The main findings from this study include the following:

1. Observations from CALIOP provide the first spaceborne evidence that aerosol emissions from ships correlate with an observed macrophysical response in low-level marine stratocumulus in the form of increasing cloud top height. We interpret this change as a response of the cloud to the change in aerosol introduced by ships. However, the magnitude of this response primarily depends on the mesoscale organization of the clouds and marginally on the atmospheric stability, as has also been suggested in modeling and observational studies [Wang and Feingold, 2009; Lebsock et al., 2008]. Open cell clouds, primarily observed in relatively unstable and moist atmospheric conditions, exhibited the largest variability in cloud top height across the cloud deck except in regions polluted by the ship where cloud tops were more uniformly distributed and elevated (131 m, roughly a 16% increase) in response to underlying ships. While closed cell clouds, primarily

observed in relatively stable and dry atmospheric conditions, exhibited no structural changes in cloud top altitude due to underlying ships.

2. Microphysical responses manifest through changes in CCN, droplet number concentration, and droplet effective radius. Only the changes to the droplet effective radius were measured in this study. Changes in droplet effective radius reported here were consistent with numerous other studies of ship tracks [Coakley et al., 1987; Hobbs et al., 2000; Christensen et al., 2009]. Differences in droplet effective radius were largest in regions of open cellular clouds where the droplets were larger and presumably more susceptible to aerosol indirect effects due low concentrations of CCN [Wood et al., 2008].

3. Macrophysical responses occur in the form of changes in precipitation rates, cloud coverage, liquid water amounts, and cloud depths. Only the changes in liquid water amounts and cloud depths were measured in this study. Opposite macrophysical responses occurred depending on whether the clouds were observed in a closed or an open cell regime. Clouds contaminated by the ships acquired significantly more liquid water (39%), as consistent with LES simulations of ship tracks [Wang and Feingold, 2009], and achieved higher cloud tops in the open cell regime. However, in the closed cell regime clouds perturbed by aerosol ended up losing liquid water amounts (a relative difference of −6%) and exhibited no changes in cloud top altitude. The changes reported here for overcast conditions (closed cell clouds) were the same as those identified by Segrin et al. [2007].

4. Contributions from both the microphysical and macrophysical properties of the clouds determine the albedo and the amount of subsequent reflected shortwave radiation

37

to space. Changes in cloud optical depth between polluted and unpolluted clouds were more than four times greater in the open cell regime compared to the closed cell regime. Because the fractional change in cloud optical depth is proportional to the fractional change in cloud albedo, we infer that the cloud albedo response to aerosol was much larger in the open cell regime. Cloud albedo increased in the polluted clouds for both the closed and open cell regimes, which resulted in an aerosol indirect localized radiative forcing of -12 W m^{-2} and -59 W m^{-2} for each regime, respectively. This range in the aerosol indirect forcing estimated for ship tracks is consistent and within the range found by Schreier et al. [2007]. In the closed cell regime, the microphysical contribution was two times larger than the macrophysical contribution to the aerosol indirect forcing. In the open cell regime, the reverse was true wherein the macrophysical contribution was larger than the microphysical contribution to the aerosol indirect forcing, where presumably, the open cellular clouds were more susceptible to aerosol and the biases inherent in the MODIS cloud retrievals. Despite the biases in the retrieved properties from partly cloud pixels, microphysical changes to the radiative properties of the clouds are likely to be as important as the macrophysical changes for determining the aerosol indirect forcing from open cellular clouds.

Ship tracks provide a unique opportunity to examine the localized effects of aerosol on low boundary layer clouds and thus provides a glimpse at the possible nature of aerosol indirect effects on low clouds. The results presented in this study highlight the distinct differences in the susceptibility of clouds to changing aerosol and we have provided a simple assessment of this susceptibility in terms of the local cloud albedo and solar forcings. Since the response of these clouds to aerosol varies according to the type

of convective regimes that influence them, it is essential to determine the global extent of

open and closed cell low clouds when making estimates of the global aerosol indirect

forcing from boundary layer clouds. Projection of the results of this study onto estimates

of global aerosol indirect forcings is the topic of an ongoing study.

Unfortunately, measurements of precipitation were not included in this study due

to an inadequate number of ship track cases detected by the CPR on CloudSat. Roughly

90% of the cases went undetected because the height of the clouds frequently occurred at

levels below the detection limit of the CPR (cloud layers less than about 0.75 km).

Accurate measurements of precipitation from CloudSat are needed to investigate the role

of precipitation on the microphysical and macrophysical properties of clouds in response

to changing aerosol. In order to increase the number of CloudSat observations, ship

tracks were identified from other regions dominated by marine stratocumulus. These

results will be presented in Part III of the dissertation, "Impacts of haze on precipitating

clouds."

REFERENCES

Ackerman, A. S., O. B. Toon, and P. V. Hobbs (1995), Numerical modeling of ship tracks produced by injection of cloud condensation nuclei into marine stratiform clouds, J. Geophys. Res., 100, 7121–7133.

Ackerman, A. S., O. B. Toon, D. E. Stevens, and J. A. Coakley Jr. (2003), Enhancement of cloud cover and suppression of nocturnal drizzle in stratocumulus polluted by haze, Geophys. Res. Lett., 30(7), 1381, doi:10.1029/2002GL016634.

Ackerman, A. S., M. P. Kirkpatrck, D. E. Stevens, and O. B. Toon (2004), The impact of humidity above stratiform clouds on indirect aerosol climate forcing, Nature, 432, 1014–1017.

Albrecht, B. A. (1989), Aerosols, cloud microphysics, and fractional cloudiness, Science, 245, 1227–1230.

Christensen, M. W., J. A. Coakley Jr., and W. R. Tahnk (2009), Morning-to-afternoon evolution of marine stratus polluted by underlying ships: Implications for the relative lifetimes of polluted and unpolluted clouds, J. Atmos. Sci., 66, 2097–2106.

Coakley, J. A., Jr., and C. D. Walsh (2002), Limits to the aerosol indirect radiative effect derived from observations of ship tracks, J. Atmos. Sci., 59, 668–680.

Coakley, J. A., Jr., R. L. Bernstein, and P. A. Durkee (1987), Effect of ship stack effluents on cloud reflectivity, Science, 237, 1020–1022.

Coakley, J. A., Jr., et al. (2000), The appearance and disappearance of ship tracks on large spatial scales, J. Atmos. Sci., 57, 2765–2778.

Coakley, J. A., Jr., M. A. Friedman, and W. R. Tahnk (2005), Retrieval of cloud properties for partly cloudy imager pixels, J. Atmos. Oceanic Technol., 22, 3–7.

Durkee, P. A., K. J. Noone, and R. T. Bluth (2000a), The Monterey area ship track experiment, J. Atmos. Sci., 57, 2523–2541.

Durkee, P. A., R. E. Chartier, A. Brown, E. J. Trehubenko, S. D. Rogerson, C. Skupniewicz, and K. E. Nielsen (2000b), Composite ship track characteristics, J. Atmos. Sci., 57, 2542–2553.

Ferek, R. J., et al. (2000), Drizzle suppression of ship tracks, J. Atmos. Sci., 57, 2707–2728.

Hayes, C. R., J. A. Coakley Jr., and W. R. Tahnk (2010), Relationships among properties of marine stratocumulus derived from collocated CALIPSO and MODIS observations, J. Geophys. Res., 115, D00H17, doi:10.1029/2009JD012046.

Hobbs, P. V., et al. (2000), Emissions from ships with respect to their effects on clouds, J. Atmos. Sci., 57, 2570–2590.

Lebsock, M. D., G. L. Stephens, and C. Kummerow (2008), Multisensor satellite observations of aerosol effects on warm clouds, J. Geophys. Res., 113, D15205, doi:10.1029/2008JD009876.

Lin, W., M. Zhang, and N. G. Loeb (2009), Seasonal variation of the physical properties of marine boundary layer clouds off the California coast, J. Clim., 22, 2624–2638, doi:10.1175/2008JCLI2478.1.

Lu, M-L., W. C. Conant, H. H. Jonsson, V. Varutbangkul, R. C. Flagan, and J. H. Seinfeld (2007), The Marine Stratus/Stratocumulus Experiment (MASE): Aerosol-cloud relationships in marine stratocumulus, J. Geophys. Res., 112, D10209, doi:10.1029/2006JD007985.

Marshak, A., S. Platnick, T. Varnai, G. Wen, and R. F. Cahalan (2006), Impact of three-dimensional radiative effects on satellite retrievals of cloud droplet sizes, J. Geophys. Res., 111, D09207, doi:10.1029/ 2005JD006686.

Pincus, R., and M. B. Baker (1994), Effect of precipitation on the albedo susceptibility of clouds in the marine boundary layer, Nature, 372, 250–252.

Platnick, S. (2000), Vertical photon transport in cloud remote sensing problems, J. Geophys. Res., 105, 22,919–22,935.

Platnick, S., and S. Twomey (1994), Determining the susceptibility of cloud albedo to changes in droplet concentration with the advanced very high resolution radiometer, J. Appl. Meteorol., 33, 334–347.

Schreier, M., H. Mannstein, V. Eyring, and H. Bovensmann (2007), Global ship track distribution and radiative forcing from 1 year of AATSR data, Geophys. Res. Lett., 34, L17814, doi:10.1029/2007GL030664.

Scorer, R. S. (1987), Ship trails, Atmos. Environ., 21, 1417–1425.

Segrin, M. S., J. A. Coakley Jr., and W. R. Tahnk (2007), MODIS observations of ship tracks in summertime stratus off the west coast of the United States, J. Atmos. Sci., 64, 4330–4345. Stephens, G. L. (1978), Radiation profiles in extended water clouds. Part II: Parameterization schemes, J. Atmos. Sci., 35, 2123–2132.

Stephens, G. L. (1994), Remote Sensing of the Lower Atmosphere: An Introduction,

Oxford Univ. Press, Oxford, U. K.

Stevens, B., G. Vali, K. Comstock, R. Wood, M. C. van Zanten, P. H. Austin, C. S. Bretherton, and D. H. Lenschow (2005), Pockets of open cells and drizzle in marine stratocumulus, Bull. Am. Meteorol. Soc., 86, 51–57.

Taylor, J. P., and A. S. Ackerman (1999), A case-study of pronounced perturbations to cloud properties and boundary-layer dynamics due to aerosol emissions, Q. J. R. Meteorol. Soc., 125, 2643–2661, doi:10.1002/qj.49712555915.

Twomey, S. (1974), Pollution and the planetary albedo, Atmos. Environ., 8,1251–1256.

Vaughan, M. A., D. M. Winker, and K. A. Powell (2005), Part 2: Feature detection and layer properties algorithms, CALIOP Algorithm Theor. Basis Doc. PC-SCI-202.01, 87 pp, NASA GSFC, Greenbelt, Md. (Avail- able at http://www-calipso.larc.nasa.gov/resources/pdfs/)

Wang, H., and G. Feingold (2009), Modeling mesoscale cellular structures and drizzle in marine stratocumulus. Part II: The microphysics and dynamics of the boundary region between open and closed cells, J. Atmos. Sci., 66, 3257–3275.

Wood, R. (2007), Cancellation of aerosol indirect effects in marine stratocumulus through cloud thinning, J. Atmos. Sci., 64, 2657–2669.

Wood, R., and C. S. Bretherton (2004), Boundary layer depth, entrainment and decoupling in the cloud-capped subtropical and tropical marine boundary layer, J. Clim., 17, 3576–3588.

Wood, R., and D. L. Hartmann (2006), Spatial variability of liquid water path in marine low cloud: The importance of mesoscale cellular convection, J. Clim., 19, 1748–1764.

Wood, R., K. K. Comstock, C. S. Bretherton, C. Cornish, J. Tomlinson, D. R. Collins, and C. Fairall (2008), Open cellular structure in marine stratocumulus sheets, J. Geophys. Res., 113, D12207, doi:10.1029/ 2007JD009371.

Xue, H., G. Feingold, and B. Stevens (2008), Aerosol effects on clouds, precipitation, and the organization of shallow cumulus convection, J. Atmos. Sci., 65, 392–406.

PART III: IMPACTS OF HAZE ON PRECIPITATING CLOUDS

CHAPTER 1

INTRODUCTION

The aerosol indirect forcing ranks among the largest single sources of uncertainty in projections of global warming [IPCC, 2007]. Lying at the heart of the problem is the complex way aerosols affect cloud via processes that operate along different pathways. Many of the processes influenced by aerosol are also of central relevance to our understanding of the cloud-climate feedback problem [Stephens, 2005].

Much of the discussion of both cloud feedback and aerosol indirect effects focuses on marine stratocumulus clouds largely because of the amount of solar energy these clouds reflect to space. Marine stratocumulus, covering roughly one-third of the global oceans [Warren et al., 1988], act as 'air conditioners' to the climate system [Stephens and Slingo, 1992], providing a cooling effect through this solar reflection. Because of their large impact on the Earth's net radiation budget, relatively small changes in marine stratocumulus could have major effects on the global climate system.

The past decade of research on the aerosol indirect effects has employed a mix of in situ, satellite, and models in an attempt to derive some understanding of this phenomenon. The results generally reveal a confusing degree of disagreement regarding the magnitude and even sign of the aerosol indirect forcing (e.g., observational estimates from [Quaas etal., 2008] and [Lebsock et al., 2008] are nearly an order of magnitude smaller than that estimated from the global climate models reported in the IPCC report) from observations of warm, low-level water clouds. A number of hypotheses (i.e., "cloud albedo effect" [Twomey, 1974], "cloud lifetime effect" [Albrecht, 1989], "semi-direct

44

effect" [Ackerman etal., 2000]) have been constructed, although meaningful relationships among the aerosol, clouds, and precipitation remain elusive [Stevens and Feingold, 2009], and the approach to incorporate these effects in global models is questionable at best.

The magnitude and sign of the aerosol indirect forcing involves both microphysical (cloud particle size and concentration) and macrophysical (cloud water content, cloud depth, cloud fraction, and drizzle) cloud property changes. Under the hypothetical assumption that the amount of liquid water remains constant as cloud condensation nuclei (CCN) are increased, microphysical changes result in higher concentrations of smaller cloud droplets with consequent increases in cloud albedo [Twomey, 1974]. Although this concept is simple and serves as a benchmark for understanding indirect effects, the constant liquid water amount assumption is rarely observed in nature. Because cloud albedo is intricately linked to the liquid water path [Stephens, 1978], changes to the amount of liquid water also determine the magnitude and possibly the sign of the aerosol indirect forcing [Lebsock et al., 2008].

In a study of ship tracks observed with a combination of sensors on the A-Train (Afternoon Train), Christensen and Stephens, [2011], hereafter Part II, were able to show how the sign of the liquid water path response and extent of the increases in cloud top height associated with the aerosol from ship effluents were largely a function of the mesoscale cellular structure of the clouds. This finding is consistent with a mounting body of work (e.g., [Wood and Hartmann, 2006]; [Savic-Jovcic and Stevens, 2008]; Wang and Feingold, 2009]; [Wang et al., 2010]) that points to the importance of mesoscale structures in shaping the water budget of these low clouds and, thus, cloud

albedo. For example, rain rates as light as 1 mm day^{-1} can modify the circulation in the boundary layer [Comstock et al., 2005] and, in some instances, transform a highly reflective region (several hundred square kilometers in area) of closed cell clouds into a darkened region of open cells. A change in the cloud structure from a closed to an open state decreases regional albedo, and the extent to which this or the opposite (from an open to closed cell state) is occurring on a global scale remains largely uncertain.

It is clear that aerosol indirect effects extend beyond the simple original ideas of Twomey and now include processes that influence cloud water path as well as microphysics through changes to processes like precipitation ([Wang and Feingold, 2009]; [Wood et al., 2009]) and evaporation ([Ackerman et al., 2004]) that alter the water budget of clouds. Although the effects of aerosol on precipitation have been studied in one form or another since the earliest cloud seeding experiments [Kraus and Squires, 1947], the importance of drizzle on low cloud properties like cloud albedo has become evident only more recently ([Baker and Charlson, 1990]; [Ackerman et al., 1993]; [Stephens et al., 2008]).

Ferek et al., [2000] observe a decrease in precipitation in the majority of ship tracks during the Monterey Area Ship Track (MAST). Similar results were also observed in the Marine Stratus/Stratocumulus Experiment (MASE) [Lu et al., 2009]. However, these studies were limited to a single field program lasting about one month, and the number of individual ship tracks used to quantify this effect was probably too small (less than 30) given the rich variety of atmospheric conditions and cloud types that extend over an annual cycle. While changes to the microstructure of the clouds exert some control over precipitation, the macrophysical properties of clouds also fundamentally determine

precipitation intensity and frequency. Macrophysical responses to changes in aerosol concentrations are complex and, to some degree, depend on the type of mesoscale convection in the boundary layer ([Wang and Feingold, 2009]; Part II), the degree of cloud coupling to surface moisture [Paluch and Lenschow, 1991], the macrophysical state of the clouds (raining/non-raining), the atmospheric stability [Lebsock et al., 2008], and the age. The extent to which the precipitation response is forced by microphysical or macrophysical changes also remains largely unknown. Analyzing these processes using a new generation of active remote sensors in the A-Train satellite constellation capable of accurately observing precipitation from an ensemble of ship tracks spanning multiple regions and annual cycles forms the impetus for the research conducted here.

Lidar observations of cloud top height across ship tracks were used in Part II to examine the cloud top altitude response to changes in aerosol concentration. That study confirmed the results of a ship track observed by in situ measurements in [Taylor and Ackerman, 1999] and those recently modeled in large eddy simulations [Wang and Feingold, 2009]. However, as Part II demonstrates, cloud top altitude was only found to increase for those ship tracks observed in broken cloudy conditions, which were generally associated with open cellular cloud forms. Aerosol ingested into a solid deck of stratus generally reduced liquid water amounts and had no impact upon cloud top altitude. Differences in the height response were likely the result of dissimilar thermodynamic structures and adjustment time scales of the boundary layer for closed and open cells ([Wood et al., 2011]; [Bretherton et al., 2010]). In closed cells, where the cloud coverage is high (extending over ~1000 km^2 region), radiative cooling at the cloud tops is uniformly distributed over the region. This cooling sharpens the temperature

contrast just above the stratus deck, creating a cap that prevents strong gradients in cloud top altitude. A similar argument can be used to describe the deepening of ship tracks in open cells where a relatively diffuse cap is maintained by comparatively weaker cloud top radiative cooling integrated over the region. Here, additional CCN from the ship plume increases cloud cover fraction, which rejuvenates the local cloud top radiative cooling and entrainment in the clouds polluted by the ship, allowing them to rise above the surrounding deck of cumulus clouds to the top of the boundary layer. The results from Part II suggest that cloud top height responses to aerosol strongly depend on the mesoscale stratocumulus regime. In addition, ship tracks observed in the open cell regime had larger liquid water amounts than the nearby-uncontaminated clouds. As a consequence, differences in the macrophysical responses between regimes strongly influence the magnitude of the adjusted aerosol indirect forcing (Part II) and, to an undetermined extent, precipitation, which is the primary focus of this study.

In this study, we extend the analysis of Part II to examine how drizzle changes in ship tracks. The database of Part II was greatly expanded upon to include ship tracks from several other regions on the globe (chapters 2 and 3), making use of measurements of light precipitation by CloudSat. This yielded the largest database of ship tracks observed synergistically by radar and lidar. The data were then screened to identify ship tracks (chapters 4 and 5) as described in Part II. Results, discussed in chapters 6, 7, and 8, address the following questions: How often is rainfall suppressed in ship tracks? Which clouds are most susceptible to changes in precipitation? Is the precipitation response forced by microphysical or macrophysical changes?

CHAPTER 2

DATA

Multiple sensors from the constellation of satellites in the A-Train were used to obtain accurate measurements of the cloud optical properties, cloud top altitudes, and rain rates observed in ship tracks and nearby uncontaminated clouds. Using the same methodology as Part II, the cloud optical properties were obtained from the Moderate Resolution Imaging Spectroradiometer (MODIS) cloud product on the Aqua satellite (MYD06). Cloud top layer height was obtained from the Cloud-Aerosol Lidar and Infrared Pathfinder Satellite Observations (CALIPSO) level 2 cloud layer product (version 3.01). The current study incorporates rain rate and radar reflectivity to diagnose precipitation responses in ship tracks. These were derived from the observations of the 94-GHz Cloud Profiling Radar (CPR) onboard CloudSat. Radar reflectivity and cloud mask identification were obtained from 2B-Geoprof [Marchand et al., 2008], and column averaged rain rates were obtained from the 2C-Column-Precipitation products [Haynes et al., 2009]. Here, the column average rain rate refers to an average rain rate between the base and top of the cloud layer as identified in the CPR cloud mask. The methodology and uncertainty of the rain rate retrieval are discussed in the following paragraphs.

The CPR provides a curtain view of radar reflectivity with vertical profiles spaced every 1.1 km and vertically sampled at 240 meters. Because the CPR's minimum detectable signal is –28 dBZ, it has the remarkable capability to detect both cloud-and precipitation-sized particles. Compared to other space borne radars (e.g. The Tropical Rainfall Measuring Mission [TRMM] has a minimum detectable signal of +17 dBZ),

very light rain rates as low as 0.5 mm day^{-1} can be detected by the CPR, making it an excellent tool to analyze the drizzle process in clouds. In this study, rain rate is retrieved from the path-integrated attenuation (PIA) of the radar beam. Unlike radar reflectivity, PIA is calculated from the surface reflection alone and is unaffected by ground clutter below 720 m. Observations of the normalized backscattering cross section of the surface, σ_o relative to the clear sky, unattenuated value of this quantity, σ_{clr} and gaseous attenuation are used to determine the PIA (details are described in [Haynes et al., 2009]). ECMWF fields of temperature and humidity, sea surface temperature, and wind are used in the calculations of σ_o and σ_{clr}. Given their uncertainties, this results in the ability to estimate PIA to within approximately 2 dB, which is sufficient to detect the light rainfall rates observed from the low-clouds analyzed in this study. Other studies have used slightly modified methodologies to obtain more accurate measures of σ_o and σ_{clr}, thereby reducing the sensitivity to 0.5 dB and enabling even the detection of cloud water from clouds less than 1 km (e.g. Lebsock et al., [2011] and Hawkness-Smith [2010]).

The radar reflectivity of targets is used primarily as a classification — that unattenuated near-surface reflectivity above some threshold (−15 dBZ) is considered as rain. Hydrometeors residing within the lowest range gates near the ocean surface generally go undetected due to the diminished sensitivity of the radar reflectivity caused by ground clutter. Ground clutter arises due to the large surface return by the Earth's surface, which magnifies the reflectivity echo and noise in the instrument's lowest range gates, the strength of which depends to some degree on the satellite zenith angle [Marchand et al., 2008]. Preceding epoch three (August 15th, 2006), the zenith angle was moved slightly off nadir to reduce the specular reflection from the surface and increase

the sensitivity of radar reflectivity below 1 km. Despite ground clutter, even in the lowest range gates, the noise floor (no longer the –28 dBZ as it is above 1 km) is also not so large that bright targets (like rain) go undetected. For example, the second range bin above the surface (preceding epoch three) provides sufficient return power above the radar noise floor (0 dBZ) to detect heavy drizzle at 480 m and moderate drizzle (noise floor –10 dBZ) in the third bin (720 m).

The CPR onboard CloudSat is able to provide reliable information about column average rainfall from shallow clouds even when the reflectivity is contaminated by ground clutter. Reflectivity, only used as a discriminator for rainfall, is not used to calculate rain rate and the PIA approach is sensitive enough to detect even cloud water in clouds below 1 km. Clearly, some precipitation will be missed, especially for rain rates below about $0.5 - 1.2$ mm day^{-1}, which is estimated to be the lower limit of detection by the method. Because the majority of the clouds from this study reside below 1 km, we recognize using a reflectivity threshold as a discriminator for rainfall may remove cases in which the clouds are actually drizzling.

To assess the fraction of clouds that were missed by the CPR, Figure 2.1 shows the distributions of cloud layers that were detected using the 2B-Geoprof product and those using the Cloud-Aerosol Lidar with Orthogonal Polarization (CALIOP). With higher vertical resolution (30 m) and sensitivity to cloud layers, CALIOP provides highly accurate measurements of cloud top altitudes from all levels in the troposphere, provided the backscatter does not become attenuated from other overlaying features. As shown in Figure 2.1, cloud top heights ranging from 400 to 700 meters exhibit the highest occurrences; as a consequence, the CPR missed about three quarters of the cloud layers

51

due to ground clutter. For most of these low-level clouds, drizzle rates were not provided in the precipitation product, and for the purposes of this study, they were considered non-raining. As stated in Part II, precipitation responses were not assessed because the ensemble of ship tracks having detectable rain rates was too small. Therefore, the database was expanded for the current study.
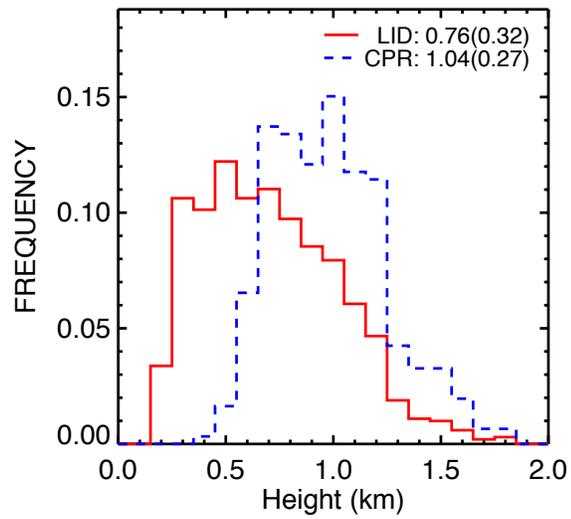
Figure 2.1. Mean cloud top altitude (estimated from CALIOP) of unpolluted cloud segments for the ensemble of lidar (solid line) and radar detected (dashed line) cloud layers. Segments from all of the combined regions occur during the period of June 2006 through December 2009. Standard deviations are given in parenthesis.

CHAPTER 3

SHIP TRACK DATABASE

Starting with the launch of CALIPSO and CloudSat, ship tracks were logged for the period of June of 2006 through December of 2009. In order to expand the database, several regions were selected as hunting grounds for ship tracks. Regions were selected based on the density of ship vessel traffic and the thermodynamic conditions conducive to the formation of ship tracks as inferred from previous studies (e.g.; [Conover, 1966]; [Coakley et al., 2000]; [Schreier et al., 2007]). Clearly, ship tracks will only form if ship vessels are being propelled under the clouds. However, much of the spatial variability in the global distributions of ship tracks is caused by the meteorology and not ship vessel traffic (i.e. ship density is correlated to ship tracks with a correlation coefficient of 0.5 as determined in Schreier et al., 2007]). Ship tracks are most often observed in low-level clouds (typically less than 1 km, [Coakley et al., 2000]) formed in a maritime subtropical air mass (mT) capped by a strong temperature inversion caused by upper-level subsidence. Atmospheric conditions such as these frequently occur along the western boundaries of continents where cold upwelling ocean currents cool the boundary layer, producing a stable layer. High static stability is a necessary condition in order to confine clouds to the boundary layer enabling aerosol to reach cloud base.

Figure 3.1 (top) shows the positions of all the identified ship tracks. In total, 1451 ship tracks were hand-logged from MODIS imagery using the protocols described in Part II. The highest density of ship tracks occurred in the Northeast Pacific (NEpac) region off the west coast of the U.S. during the period from June of 2006 through December of

2009, which is a result consistent with the global observations of [Schreier et al., 2007].

High occurrences of ship tracks were located here because the thermodynamic conditions

were conducive to the formation of ship tracks (as described in the next section) and the

ship vessel density was relatively high compared to the other selected regions. Of the four

regions considered in this study, the region with the fewest ship tracks was located in the

South Pacific Ocean off the coast of South America (Spac). While all regions exhibited

large seasonal changes in the number of observed ship tracks, the southern hemisphere

oceans tended to have the largest variability with virtually zero ship tracks being

observed for over half of the annual cycle. This is demonstrated in Figure 3.1 (bottom).

Far exceeding the other seasons, June, July, and August (JJA) exhibited the largest

number of observed ship tracks in all of the selected regions, a result consistent with

other global assessments of ship tracks ([Schreier et al., 2007]; [Campmany et al., 2009]).

To understand the regional and seasonal variability in the observations,

climatologies of the thermodynamic conditions and cloud properties were constructed for

each region and compared with those from the population of observed ship tracks. Means

and standard deviations of the atmospheric conditions for the population of ship tracks

are listed in Table 3.1; regional climatological statistics are listed in Table 3.2 for

comparison. Ship tracks were primarily observed with lower troposphere stabilities in the

range $18.4 \leq \text{LTS} \leq 25.4$ K, sea surface temperatures $283 \leq \text{SST} \leq 293$ K, cloud top

heights $0.45 \leq \text{CTOP} \leq 1.08$ km, and liquid water paths $52 \leq \text{LWP} \leq 162$ g m^{-2}. Figure

3.2 shows global mean distributions of lower troposphere stability (defined as the

difference in potential temperature between 700-hpa level and the surface), cloud top

height, sea surface temperature, and ship vessel traffic for JJA. Evidently, ship tracks

were abundantly observed in the selected regions that exhibited high stability, low sea surface temperatures, low cloud tops, and dense ship vessel traffic. The distribution of cloud top altitudes and lower troposphere stabilities was essentially the same for all of the analyzed regions. Each region exhibited a large fraction of low-level clouds (65% of cloud tops were less than 3 km) and high atmospheric stabilities (lower troposphere satiability was typically greater than 17.5 K). However, the distributions of sea surface temperature varied considerably between the regions. The annual average sea surface temperature across the NEpac region was 4 °C cooler on average than the regions in the Southern Hemisphere. While each region exhibited a strong cycle in sea surface temperature, regions in the southern hemisphere exceeded mean conditions from the ship track ensemble by approximately 5.5 K during DJF and MAM. Warmer sea surface temperatures during this period were associated with higher cloud top heights, where presumably, the deeper marine boundary layers were decoupled from the surface [Wood and Bretherton, 2004]. As a consequence, fewer ship tracks were probably observed because the effluents from the ships were dispersed/diluted in the decoupled subcloud layer before reaching the clouds [Liu et al., 2000].

Despite the smaller numbers of logged ship tracks during the DJF period, several tracks were identified in maritime polar (mP) and continental arctic (cA) air masses (as defined by Bergeron classification). Conducive to the formation of ship tracks, air masses behind polar fronts are generally associated with strong upper-level subsidence that cap a conditionally unstable shallow marine boundary layer to depths typically less than 3 km [Atkinson and Zhang, 1996]. Ship tracks forming in mP air masses were embedded in a variety of cloud types, most of which were classified as closed and open cellular cloud

forms. In addition, several ship tracks were spotted in cloud streets near the Kamchatka peninsula during DJF. Cloud streets, also known as horizontal roll vortices, are long counter rotating convective rolls (typically several hundred kilometers in length) approximately aligned with the surface wind flow typically forming in cold air outbreaks (typically colder than 273 K) over warmer sea surface temperatures. Ship tracks forming in these clouds present unique opportunities to investigate the role of aerosol in cold clouds (clouds containing ice). In total, 39 ship tracks were observed to have cloud top temperatures less than 265 K. However, CALIOP and MODIS observations indicate the presence of ice in only 10 of those cases. The vast majority of the MODIS and CALIOP retrievals for those cold cloud top clouds were flagged as warm phase (clouds composed entirely of water droplets). Given the limited number of cases, aerosol effects on cold clouds were not analyzed. To simplify the analysis, ice phase retrievals were ignored.

Using the same protocols as in Part II, clouds were classified subjectively as closed, open, or unclassifiable by visually inspecting the clouds in a MODIS image (0.64-µm channel) surrounding the ship track. However, a variety of cloud types were noted. Clouds were considered closed (493 cases), open (180 cases), rolled (i.e., cells are more elongated than wide; 133 cases), wavy (i.e., cells have an appearance of being twisted; 58 cases), uniform (i.e., clouds lack a cellular structure; 47), and streets (15) if that cloud structure remained uniform over a 100 km^2 region centered over the ship track. Clouds were considered unclassifiable (525 cases) if the cloud structure was incoherent or exhibited a mixture of cloud types over the same domain. Ship tracks observed in the unclassified cloud regime ranked among the largest compared to the others. The closed

cell regime were the next largest in number. Ship tracks identified in the open cell regime were less prevalent.

Higher numbers might suggest that ship tracks form more readily and/or exhibit longer lifetimes in closed cellular cloud systems. The numbers reported here may reflect the degree of boundary layer coupling. Using an LES simulation, Liu et al., [2000] demonstrated that ship effluents were prevented from reaching the base of a cloud when the boundary layer was decoupled from the surface. Open cellular clouds were often associated with decoupled boundary layers [Savic-Jovcic and Stevens, 2008]. Decoupling arises from a stable subcloud transitional layer that is produced by the evaporative cooling of drizzle and, in open cellular clouds this layer remains relatively undisturbed through weak turbulent mixing. Thus, fewer ship tracks may have arisen in the open cellular cloud regime because the boundary layer was presumably, often decoupled.

While ship tracks may have formed more readily in closed cell clouds, their lengths were considerably longer in open cells. In the open cell regime, the average length of ship tracks was 378 ±190 km, which was significantly longer (at the 95% confidence level) than those identified in closed cell clouds (by 50 km). The length of a ship track, defined here, is the entire length that extends from the head (first bright cloud nearest the ship) to the tail (the location at the end of the ship track where the bright polluted clouds become indiscernible from their surroundings). Thus, ship tracks may form more readily in the closed cell cloud systems that are commonly coupled to the surface when the boundary layer is shallow, but persist longer in open cells. However, without weighting the number of identified ship tracks to the relative areal coverage of each cloud regime, the actual prevalence of ship tracks by cloud type remains unknown.

A thorough study of the frequency of cloud regimes would be needed to characterize the evolution and persistence of ship tracks.
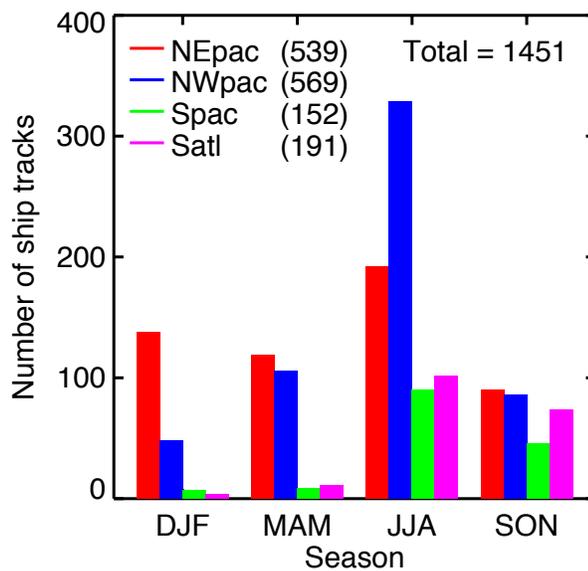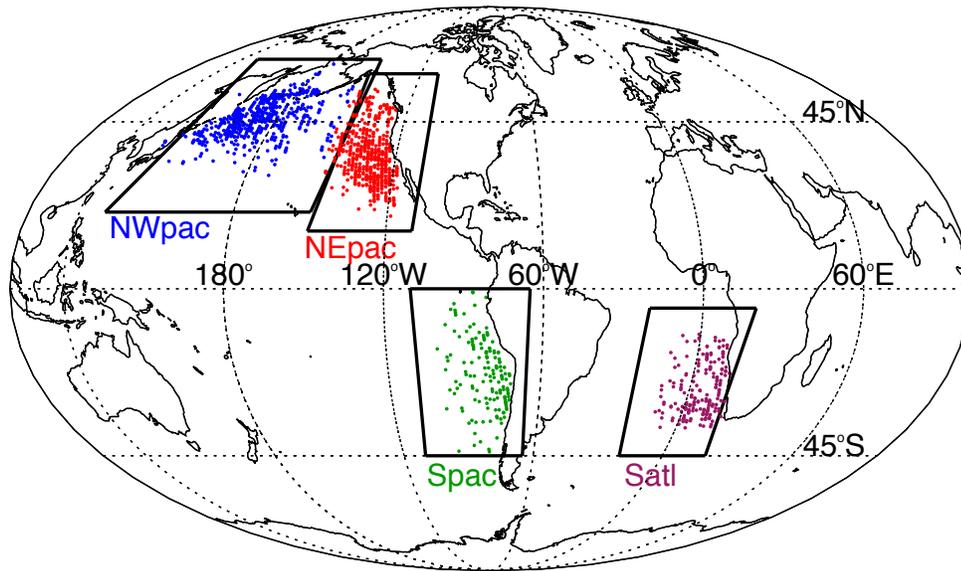
Figure 3.1. (top) Ship track locations identified in MODIS imagery and (bottom) number of ship tracks identified in each region are displayed as a function of season.

Table 3.1. Mean atmospheric conditions of ship tracks[a]

Cloud Top Height (m)	758 (317)
LTS (K)	21.9 (3.5)
SST (K)	288.1 (4.9)
LWP (g m^{-2})	107 (55)
Rain Rate (mm/day)	0.81 (2.7)
Rain Cover Fraction (%)	7.7 (18.9)

[a]Listed are the means and standard deviations (given in parenthesis) of the cloud top height (estimated from CALIOP), lower troposphere stability (LTS) and sea surface temperature (SST) (ECMWF reanalysis data), liquid water path (LWP) (MODIS), and rain rate and rain cover fraction (CloudSat) from the population of segments containing unpolluted clouds (985 cases).

Table 3.2. Regional climatological statistics[a]

	Northeast Pacific			
	DJF	MAM	JJA	SON
Cloud Top Height (km)	5.7 (4.5)	5.6 (4.7)	4.5 (4.7)	5.3 (4.7)
LTS (K)	16.7 (4.4)	17.9 (4.6)	19.1 (3.9)	16.6 (4.3)
SST (K)	287.9 (6.6)	287.6 (6.4)	290.6 (6.4)	291.1 (6.0)
Rain Rate (mm/day)	1.40 (7.4)	1.08 (6.6)	1.19 (5.7)	1.47 (7.7)
Rain Cover Fraction (%)	17.3	12.4	16.7	16.7
	Northwest Pacific			
Cloud Top Height (km)	5.1 (3.7)	6.3 (4.6)	6.7 (5.2)	6.0 (4.6)
LTS (K)	13.0 (4.9)	16.7 (4.2)	18.2 (4.1)	14.1 (4.0)
SST (K)	284.2 (9.6)	283.6 (9.1)	289.9 (8.0)	289.5 (8.5)
Rain Rate (mm/day)	1.29 (8.0)	1.24 (7.4)	1.04 (5.3)	1.58 (8.7)
Rain Cover Fraction (%)	12.2	11.6	14.7	15.8
	South Pacific			
Cloud Top Height (km)	4.8 (5.3)	5.2 (5.0)	4.2 (4.4)	3.9 (4.3)
LTS (K)	18.3 (3.4)	17.0 (3.7)	17.9 (4.7)	19.6 (4.7)
SST (K)	294.1 (3.9)	292.5 (4.5)	290.0 (4.5)	289.2 (4.1)
Rain Rate (mm/day)	0.96 (5.3)	1.25 (6.8)	1.56 (7.5)	1.48 (6.9)
Rain Cover Fraction (%)	14.2	17.7	24.5	22.7
	South Atlantic			
Cloud Top Height (km)	5.3 (5.4)	5.8 (5.3)	4.3 (4.3)	4.2 (4.4)
LTS (K)	17.8 (3.1)	16.2 (3.1)	16.6 (4.2)	18.4 (4.1)
SST (K)	294.1 (5.1)	292.2 (5.5)	290.1 (4.9)	289.7 (4.9)
Rain Rate (mm/day)	1.11 (5.9)	1.07 (6.1)	1.38 (7.7)	1.32 (6.8)
Rain Cover Fraction (%)	16.1	15.6	19.4	19.9

[a]Same as Table 1 (excluding LWP). Cloud top height was derived from the average of all layer cloud top altitudes detected by CALIOP in the region. Climatologies were constructed from three years (2007 — 2009) of data for each region and season.
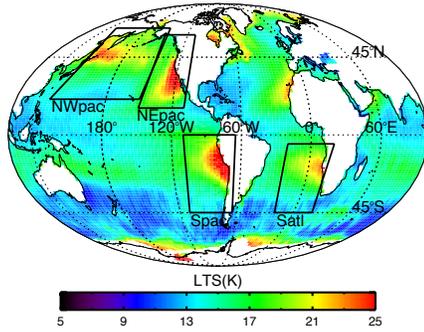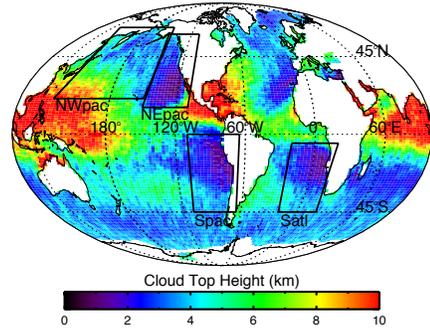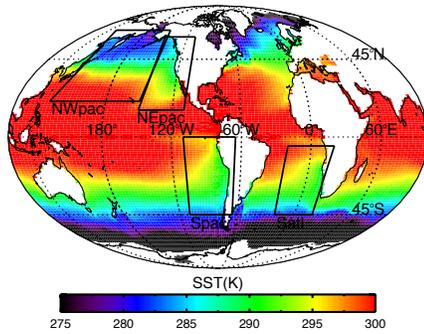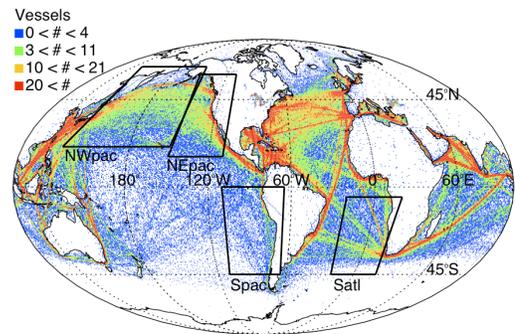
Figure 3.2. (a) Global distributions of lower troposphere stability (LTS); (b) cloud top height; (c) sea surface temperature (SST); (d) and ship vessel traffic assessed from Amver data (provided by the Amver Team USCG Operations Systems Center – www.amver.com); binned by 2.5° × 2.5° regions and averaged over three years (2007, 2008, and 2009) for JJA. ECMWF re-analysis data was used to obtain LTS and SST. Cloud top height was determined from the lidar observations in the 2B-Geoprof-Lidar CloudSat data product.

CHAPTER 4

ANALYSIS PROCEDURES

The procedure used to detect polluted and unpolluted pixels from ship tracks in

MODIS imagery and collocate them to CALIOP was the same as those described in Part

II. To investigate the influence of particle pollution on radar reflectivity and rain rate, the

observations from the CPR were collocated to the nearest one-kilometer pixel locations in

the MODIS imagery. This process is outlined in Figure 4.1. Figures 4.1a and 4.1b show

vertical cross sections of the lidar backscatter and radar reflectivity. The cross sections

span the polluted (red line indicates ship) and unpolluted pixels (blue and green lines

indicate con 1 and con 2, respectively) of the ship tracks shown in the top panel of Figure

4.1.

The algorithm used in 2B-Geoprof, detects clouds if they extend beyond the depth

of the ground clutter region (typically 3 vertical bins or 720 m) and have a significantly

higher target reflectivity return than that given by the background noise. The cloud mask

from this product was utilized to remove regions of clear sky and those contaminated by

the surface return. Cloud mask values range from zero to forty, with larger values

indicating a reduced probability of false detection. Values less than twenty typically have

numerous false positive cloud detections (44% assessed from CALIPSO comparison) due

to very weak echo signatures, which require along-track averaging to obtain a sufficient

signal in reflectivity [Marchand et al., 2008]. Cloud mask values above or equal to this

threshold have fewer false positives (less than 5%), thereby increasing the reliability of

hydrometeor layers detections. Therefore, measurements of radar reflectivity were used

in the analysis if a cloud mask value of twenty or greater was identified in the ship track domain. The results of the cloud screening are depicted in Figure 4.1b.

To ensure the success of retrieving cloud layers over the ship track domain, clouds were incorporated in the analysis if they were detected using CloudSat (2B-Geoprof) or CALIOP. Cloud layers were prescribed a precipitation rate, non-raining (flag = 0) or raining ($1 \leq$ flag ≤ 3; lower values indicating a smaller probability of precipitation in the profile), based on the value of the flag provided by the 2C-Precip product. As previously discussed, cloud layers missed by the CPR but captured by CALIOP were considered non-raining. The instruments have different spatial resolutions (three CALIOP profiles typically span a single CloudSat profile); therefore a low-cloud was deemed to exist in a CPR profile if it was either detected using the 2B-Geoprof product or if a cloud was identified in three coincident CALIOP profiles. Only profiles with clouds lower than 3 km were considered for analysis. Figure 4.1c shows the column-average rain rate over the low-clouds in the domain of the ship track. An analysis of these changes is described in further detail in chapter 5.2.

The precipitation response reported in this study is expressed as the difference in the rain rate between the clouds contaminated by ship plumes and the surrounding unpolluted clouds. Rain rates were spatially averaged over raining and non-raining profiles throughout the domains of ship tracks. As a consequence, spatially averaged precipitation rates were smaller than the rain rates that would be given from the raining profiles alone. Averaging the data in this way provides insight into the manner in which ship plumes modify the areal extent of rain cover and intensity. Here, rain cover fraction is given by the number of raining profiles divided by the total number of profiles

containing low-cloud observed by either the radar or the lidar (i.e. the fraction of the clouds that are raining in a segment). Thus, the rain rate averaged over a segment of clouds (the units are in mm/day) can be written as,

$$R = R_p A_r, \tag{1}$$

where the intensity averaged over the clouds that are raining is given by R_p and the fraction of clouds in the segment with detectable rainfall is given by A_r. The difference simply follows as,

$$\Delta R = R_p^{cons} \Delta A_r + A_r^{Ship} \Delta R_p, \tag{2}$$

where the first term represents the change in rainfall due to differences in rain cover fraction (ΔA_r) and the second term represents the change due to the difference in the intensity of rainfall (ΔR_p). Clearly, if all clouds were raining (i.e. rain cover fraction equals 1), changes in rainfall would be given by the changes due to the intensity alone ($\Delta R = \Delta R_p$). For many clouds, particularly those missed by the CPR, light drizzle may be occurring. As a consequence, the difference in rain cover fraction between the polluted and unpolluted clouds might more closely represent the difference in the occurrence of light drizzle. Contributions from each term are explored in the following sections.

CLOSED CELL REGIME / OPEN CELL REGIME

a) 532 nm Total Attenuated Backscatter (CALIPSO)

b) Radar Reflectivity (CloudSat 2B-Geoprof)

c) Column Average Rain Rate (CloudSat 2C-Precip-Column)
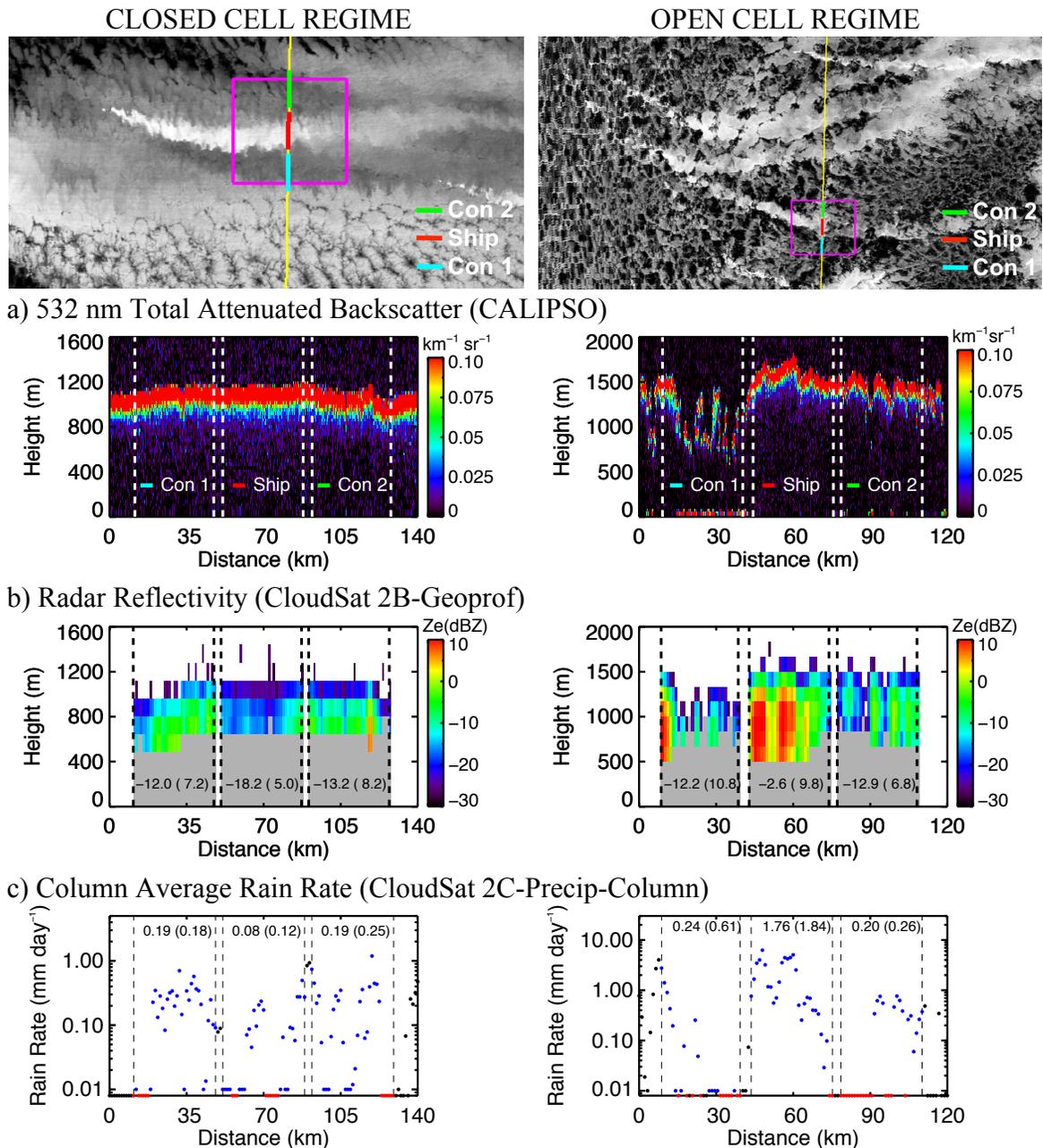
Figure 4.1. (left panel) Case study of a ship track observed in closed cell clouds on Feb. 3rd, 2008 and (right panel) open cell clouds on Jan. 11th, 2007. The red solid line represents pixels that were contaminated by the ship, and the blue and green lines represent unpolluted clouds collocated to the CALIPSO orbital track (yellow line). (a) Vertical profiles of total attenuated backscatter and (b) radar reflectivity were collocated to the pixels polluted by the ship (center of dashed lines) and their unpolluted counterparts. Radar reflectivity is displayed for sections where the cloud mask values were greater than or equal to twenty. Sections contaminated by ground clutter are gray. (c) Rainfall was averaged over the raining (blue circles) and non-raining (red circles) clouds. Means and standard deviations are given.

66

CHAPTER 5

SCREENING PROCEDURES

To serve as an independent sample, a sufficient number of measurements observed from MODIS, CALIOP, and the CPR were needed to exceed an effective sample size to represent statistically significant averages. Using the same criteria as in Part II, ship track cases were included in the analysis if the automated detection scheme identified at least twenty one-kilometer MODIS pixels polluted by the ship and at least twenty pixels, which serve as controls from either side of the ship track. MODIS pixels were included in the analysis if they were flagged as being low-level (cloud top pressure greater than 600 hPa), single layer, and composed of liquid water droplets as determined in the MODIS cloud product. Segments needed to have at least five cloud top altitude measurements (CALIOP) from the ship track and at least five from either control. To examine spatial fluctuations in precipitation, spatial auto-correlations of precipitation were assessed for ship track domains with at least ten profiles. On average, the auto-correlation value fell to below 1/e after a single lag (plot not shown) of 1.1 km (one horizontal CloudSat bin), which is in general agreement with the decorrelation scale spectrum having a weaker drop-off at small scales [Wood, 2005]. Thus, each measurement of precipitation constituted an independent sample, however it's likely that there is sub-footprint scale variability in precipitation within the CPR footprint. For some perspective, the spatial auto-correlations of the cloud optical properties derived from MODIS (effective radius and optical depth) are approximately 5 km [Segrin et al., 2007], or roughly 3 times larger. To construct representative averages of rainfall within and

outside a ship track region, a sufficient number of independent samples was needed to minimize the noise inherent in the retrieval of precipitation. The precipitation product provides an estimate of the uncertainty for each retrieval of rain rate. On average, the errors (that stem from the calculation of σ_o and σ_{clr}) for each retrieval were between 30 and 50% of the mean retrieved rain rate. To minimize the noise, rain rates were averaged over several profiles containing low-level clouds separately for the ship track and for the surrounding unpolluted clouds. On the average, segments contained roughly 13 CloudSat profiles. A segment was used in the analysis if a minimum of four estimates of precipitation were acquired from either raining or non-raining cloudy profiles. Justification for using this approach is provided in the following paragraphs.

The CPR measures reflectivity profiles along the CloudSat orbital track with no across track sampling. As a consequence, the characteristics of the precipitation could not be assessed down the lengths of individual ship tracks. The number of rain rate retrievals used in a segment was limited by the width and angle the ship track made with the CloudSat orbit. On average, the width and intercept angles were 11 km (estimated from MODIS 1-km imagery) and 64° (the majority of intercepts were closer to a perpendicular angle than one that was parallel) respectively, leaving roughly half of the ensemble of segments with fewer than ten independent samples of precipitation.

To test whether segments with fewer samples represented the mean characteristics of the rainfall, a composite analysis of the precipitation responses was assessed for those segments having fewer than ten and greater than ten samples. Even though rainfall and cloud depth was higher for those ship tracks having more across track samples (i.e. the width of the track scales with cloud depth), precipitation responses between the polluted

68

and unpolluted clouds were in the same direction for each composite. As a result, the number of independent samples did not affect the sign of the overall results. Since a large fraction of the ship track segments have fewer then ten samples, an effective sample size of four was chosen to construct reasonably representative averages of rainfall without removing a significant fraction of the segments used in the analysis. A minimum of four samples also ensures that the standard error would not exceed half the standard deviation of the sample (i.e. $\sigma/\sqrt{N} = \sigma/2$).

In total, 1451 ship tracks were hand-logged from MODIS imagery. In some instances, particularly when ship traffic was dense, the unpolluted clouds from the domain of a ship track would fall onto the polluted clouds of a nearby ship track. Such cases were removed, leaving 1369 cases. If the only criterion established were the use of the passive remote sensing data (MODIS), 1083 segments would be suitable to study the optical properties of ship tracks. By including the observations of CALIOP (requirements used in Part II), the number of cases slightly diminished to 1032. Segments were screened to include a minimum of four CloudSat profiles (995 segments) containing warm phase precipitation (ten of those segments were affected by snow), leaving 258 raining (detected in either the polluted or unpolluted clouds) and 727 non-raining cases to study the breadth of the microphysical and macrophysical responses to aerosol.

CHAPTER 6

RESULTS

6.1. Rainfall departures

How often is rainfall suppressed in ship tracks? Out of 985 cases, 185 ship tracks
were observed to have reductions and 73 were found to have increases in column
averaged rain rate compared to the ambient clouds. The remaining 727 cases were
composed exclusively of non-raining clouds. This assessment is consistent with the
results reported in other field campaigns involving ship tracks (i.e. [Ferek et al., 2000]
and [Lu et al., 2009]). These results demonstrate that aerosol plumes from oceangoing
vessels most frequently decrease mean precipitation rates in polluted clouds. Although
reductions of precipitation were common amongst the clouds with detectable rainfall
(72%), a substantial fraction of ship tracks (28%) exhibited the opposite response. These
findings contrast with results from simple heuristic models and other precipitation
susceptibility constructs which always predict a decrease in precipitation with increasing
droplet concentrations ([Wood et al., 2009]; [Sorooshian et al., 2009]).

To shed light on what drives the sign and magnitude of the precipitation response,
two case studies with opposing precipitation responses were examined (Figure 4.1),
followed by an analysis outlining the response of different mesoscale cloud regimes.
Further investigation was conducted to understand which clouds were most susceptible to
a change in precipitation and whether the response was primarily controlled by
microphysical or macrophysical changes.

6.2. Case study I: ship track observed in closed cellular stratus

The clouds examined in Figure 4.1 (left column) exhibited profound changes in the microphysical and macrophysical properties in the region polluted by the ship plume. The track was identified in the Northeast Pacific during boreal winter (February, 2008). The width of the ship track at the location of the CloudSat overpass was approximately 35 km. The length of the ship track from the location nearest the ship (head) to the overpass was 220 km. This was calculated by summing the distance along the hand-logged locations outlining the shape of the ship track as observed in the MODIS image. The wind velocity ten meters above the surface (ECMWF reanalysis product) was northwesterly at approximately 7 m s^{-1}. Given the wind velocity, and by assuming a typical steaming speed of 12 m s^{-1} for a container ship [McNicholas, 2008] with an eastward bearing (based on the orientation of the ship track), the clouds were estimated to had been polluted by the ship for approximately five hours at the time of the satellite overpass. Effective radii significantly decreased, liquid water paths increased, optical depths significantly increased, and cloud top heights significantly increased (although, the relative increase was only 2%) between the polluted and surrounding clouds. A strong response in radar reflectivity was also evident. Reflectivity decreased by approximately 5 dBZ in the ship track region. Consequently, significant decreases in the precipitation intensity (rain rates were halved in the ship track region) were retrieved in the 2C-Precip Column product. Because the differences in rain cover fraction were small between the ship (0.74) and controls (0.83), reductions in rainfall resulted primarily from the differences in the rain rate intensity.

6.3. Case study II: ship track observed in open cellular stratocumulus

Compared to the previous case study, ship tracks observed in Figure 4 (right panel), exhibited the opposite precipitation response. Geographically and temporally, the ship tracks observed here share similar characteristics to the previous example; tracks were identified in the Northeast Pacific region during the boreal winter (January, 2009). The boundary layer was slightly deeper (by 0.5 km) and unstable (LTS was smaller by 2.5 K) in comparison to the previous example. Here, the distance from the head of the ship track to the overpass was considerably longer than in the previous example. The width of the ship track was approximately 30 km and the head of the ship track was approximately 570 km away from the CloudSat overpass. Amazingly, the ship track continued for another 400 km beyond the cross section as shown in the figure. Clearly, the plumes from the ships increased the fractional cloud coverage. Changes in effective radius were negligible. However, significant increases in optical depth (Ship = 25.4, Cons [average of con 1 and con 2] = 11.3), and liquid water path (Ship = 335 g m^{-2}, Cons = 146 g m^{-2}) were observed in the polluted clouds estimated by MODIS. It is noteworthy that the optical properties in the controls may be biased due to low cloud coverage (an explanation of this bias is provided in chapter 8.2). Mean cloud top altitude across the ship track region was significantly higher than the surrounding clouds by approximately 260 m (estimated using CALIOP). Radar reflectivity increased on average in the ship track (by 10 dBZ).

Throughout the domain, several regions of high target reflectivities were concentrated to narrow spatial areas. Features such as these may indicate the locations of enhanced vertical ascent associated with the mesoscale structure and location of the

cellular walls. Evidently, cloud top heights and precipitation rates increased substantially across these convective cores. Convective cores, such as the one described in this case, appear to be a common feature among the irregular configuration of the cellular walls in the open cell regime. While scanning through several images, it was noted that, when ship tracks were present, the convective cores tended to be concentrated in the region polluted by the ship. This particular case exhibits several convective cores in the controls, but with diminished intensity. Convective cores concentrated to the ship track region, occurring in all of the ship tracks to the north of the one selected here, may have arisen due to the influence of a local circulation as discussed in Wang and Feingold [2009]. Based on the increases in cloud cover fraction, relatively long spatial extents of the ship tracks, enhanced precipitation in the polluted regions, and higher cloud tops associated with the pollution, the atmospheric conditions for this particular case led to highly susceptible clouds to an aerosol perturbation.

CHAPTER 7

CLOSED AND OPEN CELL CLOUD STATISTICS

7.1. Rainfall

The previous case studies demonstrated key differences in the precipitation response between stratocumulus regimes. To examine this in further detail, ensemble averages of the cloud properties are presented for the population of ship tracks inhabiting closed (367 cases), open (109), and unclassified (354) stratocumulus cloud regimes. The remaining cases were ship tracks belonging to the rolled (86 cases), wavy (47), uniform (20), and cloud street (2) stratocumulus regimes. To simplify the presentation of this section, these cases are not shown. Ship plume effects on rainfall in the remaining regimes resembled similar responses of the ship tracks identified in the closed and unclassified cellular clouds.

To serve as a sample in these ensembles, segments needed to span a minimum of four CloudSat profiles over the polluted and unpolluted cloud domains. These results are summarized in Table 7.1. The closed and open cellular clouds exhibited the same optical and geometrical cloud responses identified in Part II. Figure 7.1 shows the rain rates of the polluted and unpolluted clouds observed in the closed (left), open (middle), and unclassified (right) cloud regimes. Because the unclassified regime closely resembled the precipitation responses observed in the closed cell regime, further analysis of this regime was ignored unless otherwise stated. In agreement with Comstock et al. [2007], clouds composing the closed cell regime tended to have lower area-averaged rain rates compared

74

to those in the open cell regime. In addition, as shown in Figure 7.2, rainfall was found to occur more frequently in open cells. Because the majority of the CPR profiles over the polluted clouds were composed of non-raining clouds (see ν_{max} in Figure 7.2), in most cases the precipitation response was strongly influenced by changes in the rain cover fraction. For example, a large difference in mean rain rate occurred if the ship track region contained a larger fraction of non-raining clouds than the nearby unpolluted cloud region (or visa versa), which is represented by equation (2).

To exemplify the changes between the polluted and unpolluted clouds, Figure 7.3 shows the differences in mean rain rate (left) and rain cover fraction (right) between the ship and controls for the closed (solid line) and open (dashed line) cell regimes. In both cloud regimes, the ship plume had a significant impact on the rain rate and rain cover fraction, but responses differed between the two cloud regimes. In the closed cell regime, significant reductions in rain rate were observed in the polluted clouds compared to the clouds surrounding the ship track (-0.19 ± 0.05 mm/day; a $68 \pm 17\%$ decrease). These differences were similar to the relative decreases in rain cover fraction ($-61 \pm 13\%$). The contributions to changes in rain cover fraction and intensity were examined using equation (2). In the closed cell regime, differences in rain cover fraction between the polluted and unpolluted clouds accounted for approximately 90% of the precipitation response. Therefore, ship plumes ingested into closed cellular clouds decreased domain averaged rain rates primarily through reducing the spatial coverage of the rainfall. In contrast, the opposite response occurred in the open cell regime, wherein rain rate (1.14 ± 0.49 mm/day; a $89 \pm 38\%$ increase) and rain cover fraction increased (by $31 \pm 38\%$) as a result of oceangoing vessels. Approximately 35% of the response was due to the

increases in the rain cover fraction; the other larger portion was due to the increased

intensity of the rainfall. The difference in the size of the rain rate response between

closed and open cells is a simple consequence of average rain rates being greater in the

open cells.

Table 7.1. Comparisons between closed and open cell cloud properties[a]

	Closed Cell Clouds (367 cases)			Open Cell Clouds (109 cases)		
	Ship	*Controls*	*Ship-Controls*	*Ship*	*Controls*	*Ship-Controls*
Reflectivity (dBZ)	−23.1 (2.8)	−21.0 (3.6)	−2.1 (0.32)	−16.3 (5.4)	−14.8 (3.1)	−1.4 (0.69)
Rain Rate (mm/day)	0.09 (0.53)	0.27 (1.02)	−0.19 (0.05)	2.43 (5.60)	1.29 (2.25)	1.14 (0.49)
Cloud Cover Fraction (%)	99.1 (5.8)	97.6 (8.5)	1.5 (0.41)	96.5 (10.7)	75.1 (19.2)	21.4 (1.71)
Rain Cover Fraction (%)	2.4 (10.1)	6.1 (17.0)	−3.7 (0.77)	24.8 (32.2)	18.9 (24.7)	5.9 (2.39)
Cloud Top Height (m)	817 (298)	815 (301)	1 (1)	910 (309)	832 (303)	77 (8)
Effective Radius (μm)	10.3 (2.0)	12.4 (2.8)	−2.1 (0.1)	14.6 (2.9)	19.0 (3.1)	−4.5 (0.3)
Optical Depth	13.7 (6.3)	12.7 (5.9)	1.0 (0.2)	13.3 (4.9)	8.3 (2.9)	5.0 (0.5)
Liquid Water Path (g m^{-2})	96 (54)	108 (60)	−11 (1)	132 (60)	107 (41)	24 (5)

[a]Listed are the means and standard deviations of *Ship* and *Controls* and the means and standard errors of the means for *Ship* − *Controls* for cloud average rainfall, cloud cover fraction (# of clouds per # of domain profiles), fraction of clouds that are raining (rain cover fraction), cloud top height, droplet effective radius and liquid water path derived from the 3.7-μm radiances, and visible cloud optical depth. Also listed is the ensemble average radar reflectivity, consisting of 107 closed and 66 open cell cases which were deep enough to be observed by the CPR. Standard deviations and standard errors of the mean are given in parentheses.
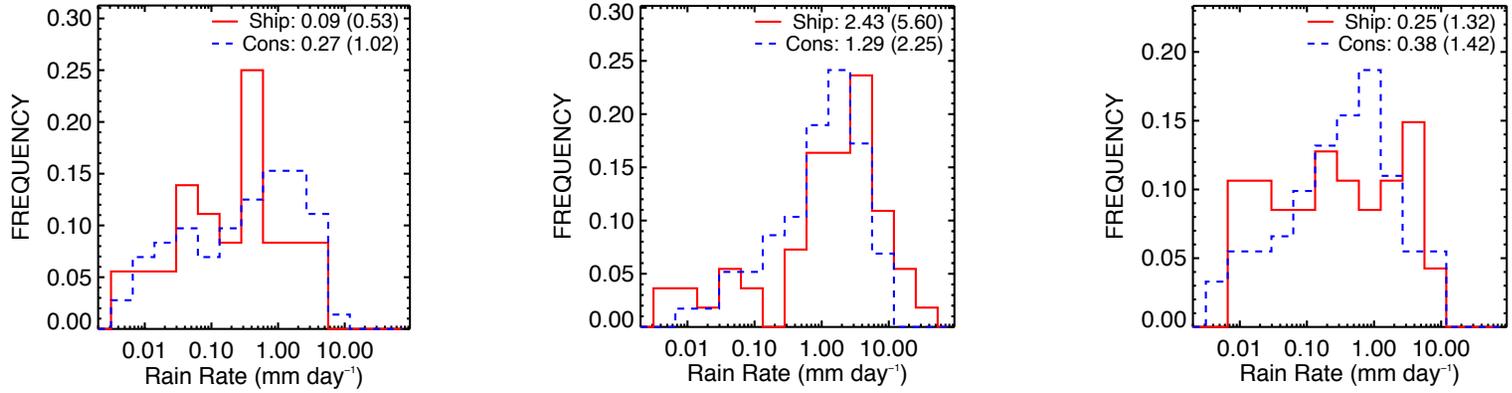
Figure 7.1. Rain rates averaged for ship track segments containing polluted (Ship; solid) and unpolluted (Cons; dashed) clouds identified in the closed (left), open (middle), and unclassified (right) regimes. Means and standard deviations are provided; standard deviations are shown inside the parenthesis.
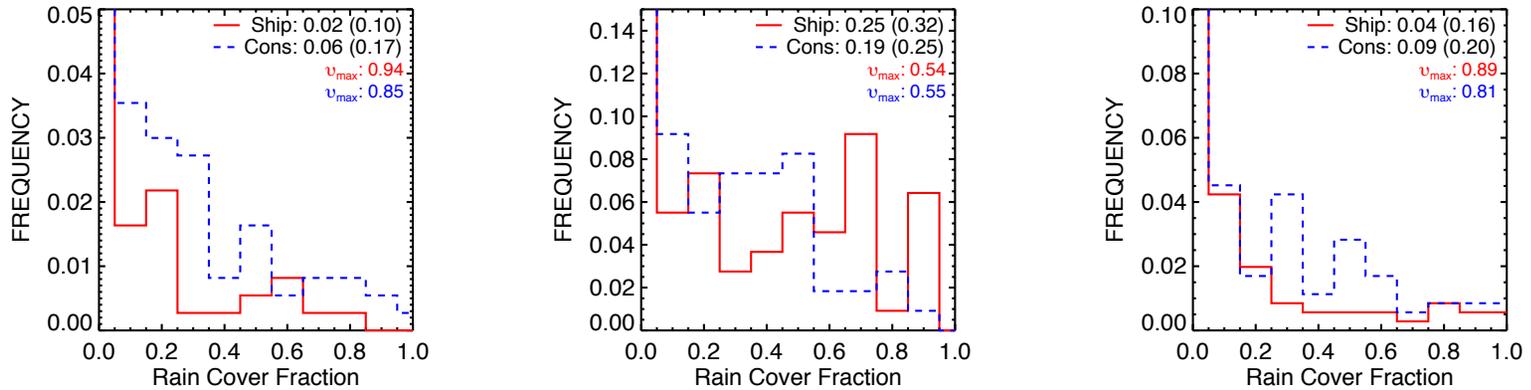
Figure 7.2. Same as in Fig 5., except mean rain cover fraction; maximum frequency values (ν_{max}) occur for non-raining clouds (i.e. rain cover fraction equals zero) and are given for the ship (solid) and cons (dashed) segments.
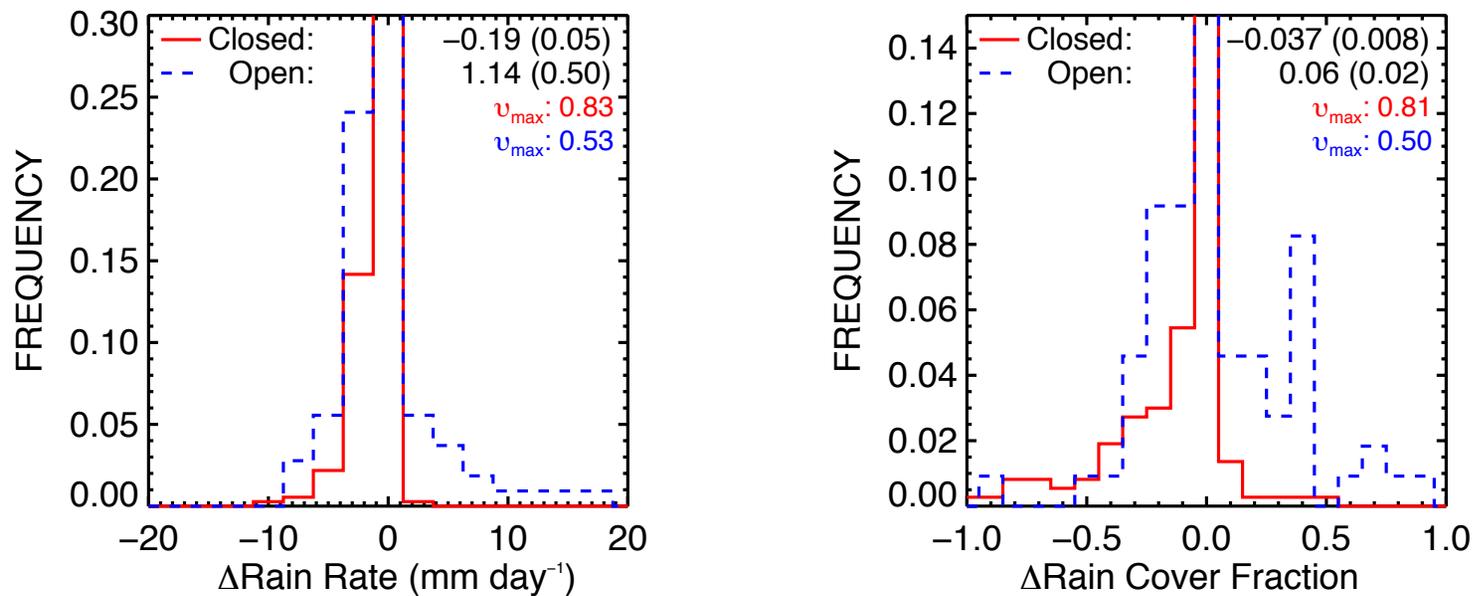
Figure 7.3. Mean differences in rain rate (left) and rain cover fraction (right) between the polluted and nearby- unpolluted clouds observed in closed (solid line) and open (dashed line) cell regimes. Maximum frequencies are provided for the non-raining clouds. The standard error of the difference of the mean is given in parenthesis.

7.2. Rain rate variability and statistical tests

Statistical tests were performed to determine whether the ship plume was responsible for the observed changes in rainfall. Precipitation responses were analyzed between the unpolluted clouds (con 1 and con 2) on either side of the ship track and compared with the response associated with the ship track. Table 7.2 lists the mean differences and standard errors of the mean differences between the unpolluted clouds (*Con1 – Con2*) and between the polluted and the combined unpolluted clouds from both sides of the ship track (*Ship – Cons*). The table also lists the average standard deviation in precipitation from the ensemble of ship track segments. Clearly, the variability in rainfall was different between the closed and open cell regimes and was largest in the open cell regime where the amplitude and spatial distribution of precipitation was highly irregular. Differences that were statistically significant at the 95% confidence level are shown as boldface font in Table 7.2. In the closed and unclassified regimes, precipitation was suppressed in the ship track clouds for the majority of cases (also displayed in Figure 7.3). However, in the open cell regime where there were roughly an equal number of cases with both enhanced and diminished rainfall, the ensemble average difference between the polluted and unpolluted clouds was not statistically significant. In all of the regimes, the absolute value of the differences in rainfall between the polluted and unpolluted clouds were statistically insignificant and considerably smaller than the effects of the pollution on the clouds.

Further tests were conducted to determine how often significant differences in precipitation could be claimed for individual ship tracks. Table 7.3 lists the number of cases, categorized by the confidence level, in which the differences in precipitation were

statistically significant using a two-tailed t-test. The average difference, standard deviation, and number of CloudSat footprints per segment for the ensembles are provided for each category. As expected, due to inherent noise caused by the relatively short autocorrelation length scale of precipitation throughout the segments (the size of the CloudSat footprint), the number of cases decreased as the difference became statistically significant at higher confidence levels. At higher confidence levels, the average standard deviation of the segment rainfall increased and, as a consequence, a larger sample size and difference was needed between the polluted and unpolluted clouds to significantly stand out above the background noise. These results suggest that the precipitation rates were highly skewed (i.e. larger rain rates generally led to significant differences). As a consequence, a substantial number of ship tracks were obtained having significant rain rate differences between the polluted and unpolluted clouds.

Table 7.2. Rain rate statistics[a]

	Stratocumulus Regime		
	Closed Cell	Open Cell	Unclassified
Con 1 – Con 2 (mm/day)	0.05 (0.06)	−0.32 (0.39)	-0.02 (0.09)
Ship – Cons (mm/day)	**−0.16 (0.04)**	0.62 (0.45)	**−0.12 (0.05)**
σ_{ship} (mm/day)	0.11	2.7	0.23
σ_{cons} (mm/day)	0.35	2.6	0.52

[a]Listed are the means and standard errors of the means for the differences in rain rate between each control (*Con 1 – Con 2*) and between the ship and combined controls (*Ship – Cons*). Also listed is the ensemble average standard deviation for the polluted (σ_{ship}) and unpolluted clouds (σ_{cons}). The ensemble is slightly smaller due to requiring a control from both sides of the ship track. Numbers cast in boldface represent statistically significant differences from the mean at the 95th % confidence level. Standard errors of the mean are listed in parenthesis.

Table 7.3. Statistical significance on the differences in rainfall[a]

		Confidence Level		
	No Threshold	90th %	95th %	99th %
	Decrease in Precipitation			
Number of Ship Tracks	185	60	35	20
# pixels/seg	17.1	20.5	22.4	23.5
ΔR (mm/day)	−2.1	−2.4	−2.8	−3.6
σ (mm/day)	1.6	2.2	2.2	2.5
	Increase in Precipitation			
Number of Ship Tracks	73	36	33	20
# pixels/seg	17.7	17.4	17.8	19.0
ΔR (mm/day)	3.1	5.4	5.4	6.7
σ (mm/day)	3.6	4.6	4.5	5.0

[a]Statistical significance was assessed using a two-tailed t-test for the ensembles of cases having decreases and increases in rainfall between the ship track and surrounding clouds. The average number of samples per segment (#pixels/seg), difference in rainfall between the ship and controls (ΔR), and ensemble standard deviation (σ) are given for each confidence level.

7.3. Reflectivity profiles

Radar reflectivity, expressed in dBZ = 10log(Z), can be used to infer the changes

in the size (diameter, D) and/or number concentration of drizzle-sized drops (through

an assumed droplet size distribution; N[D]) simply using the Rayleigh approximation in

the radar equation, where the reflectivity is given by $Z = \int_0^\infty N(D)D^6 dD$. To analyze

which portions of the clouds exhibited changes in droplet concentration and/or size due to

the ship plume, reflectivity was normalized according to the top of the cloud layer for

each profile. All profiles were then averaged over the polluted and unpolluted cloud

domains of each ship track. Because the CPR missed many cloud layers below 1 km,

radar reflectivity profiles could only be assessed for about half of the ship tracks. The

deeper clouds in this composite were thus, biased toward heavily drizzling cases. Due to

the coarse vertical resolution, a running mean filter was applied to the vertical coordinate

system to smooth the reflectivity with height. This was accomplished by averaging the

reflectivity in normalized height intervals of 0.2. Because the ground clutter regions hid

most of the vertical extent of the cloud layers, the number of samples were largest near

cloud top (i.e. z/ztop = 1).

Figure 7.4 shows the vertical distribution of the mean reflectivity averaged from the

population of ship track observations. Common to all of the cloud regimes, reflectivity

generally increased from cloud top to cloud base. Higher reflectivities were likely

observed near cloud base due to a larger fraction of the scattering volume caused by

drizzle-sized drops. Because reflectivities were larger in the open cell regime (mean

cloud base reflectivity was approximately −6 dBZ) compared to the closed cell regime

(−14 dBZ), rain rate estimates were significantly larger.

Aerosol plumes from the ships had a profound impact on the reflectivity in both the closed and unclassified regimes. In these regimes, the reflectivity was smaller than the surrounding clouds by approximately half of one standard deviation of the mean at each level. Statistically significant differences at the 95th percentile were identified throughout most of the cloud layer, particularly in the middle to upper portion where the number of samples were large. Because the reflectivity was reduced by approximately 3 dBZ, this resulted in a decrease of nearly 50% of the backscattered power. This reduction would have manifested as either smaller diameters and/or numbers of drizzle-sized drops in the polluted clouds.

In the open cell regime, where rain rates were enhanced in the polluted clouds, the reflectivity changes were small except near the cloud base. However, the response was not as clear due to larger variance and smaller separation between the ship and controls associated with the reflectivity. As a consequence, differences in reflectivity were not statistically significant. Higher reflectivities near the base of the clouds may in part explain the increased rain rates from the polluted clouds in the open cell regime.
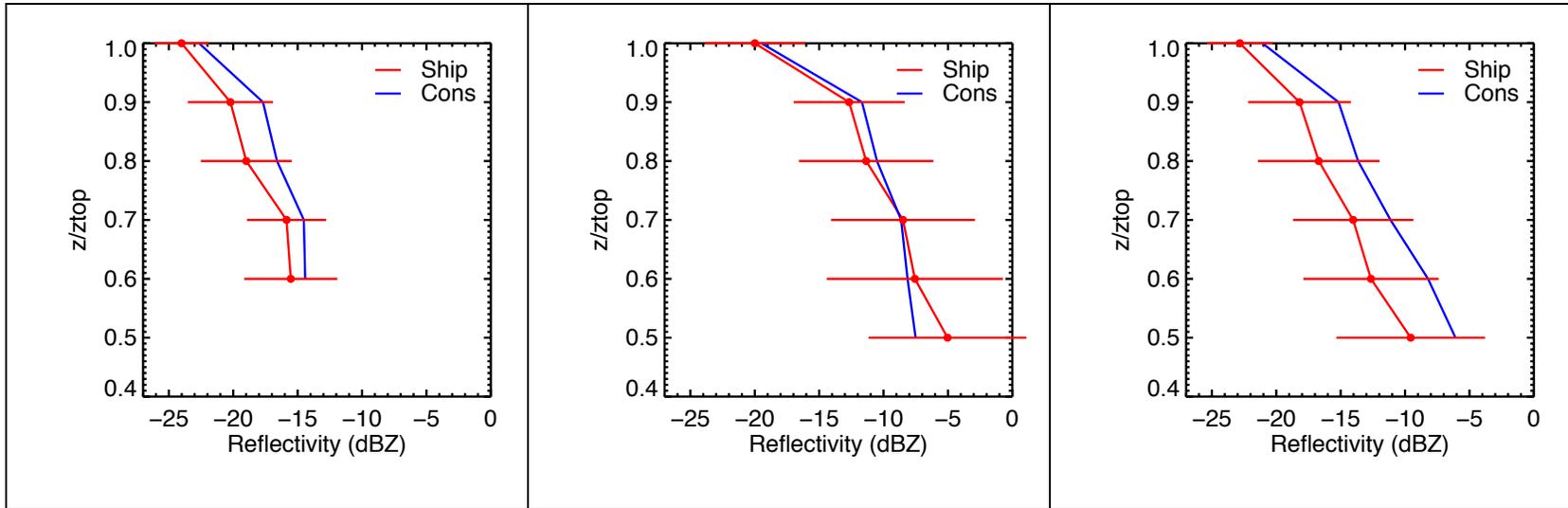
Figure 7.4. Average radar reflectivity plotted in vertical coordinates normalized to the top of the cloud for the ensembles of closed (left), open (middle), and unclassified (right) cellular cloud regimes. Observations of the polluted (unpolluted) clouds are shown by the solid (dashed) line, respectively. Horizontal lines are plus and minus one standard deviation about the mean as observed in the polluted clouds.

CHAPTER 8

RELATIONSHIPS TO CLOUD OPTICAL PROPERTIES

8.1. *Precipitation susceptibility*

Which clouds were most susceptible to changes in precipitation? Figure 8.1 shows the change in precipitation rate (top) and the fractional change in cloud optical depth (bottom) as a function of the optical depths and droplet radii derived from MODIS observations. The susceptibility of a cloud to changes in albedo by increasing the concentration of cloud droplets (through aerosol) has been shown to strongly depend on the initial size of the cloud droplets and optical thickness of the cloud (e.g., see Part IV and Platnick et al., [1994]). Figure 8.1 was constructed by binning the results according to the optical depths and droplet radii from the unpolluted clouds in each ship track domain. The changes were binned in increments of three in optical depth, from $0 \leq \tau \leq 24$, and three micrometers in droplet radius, from $6 \leq R_e \leq 24$. To be included in the figure, each bin required a minimum of five samples. For the clouds with small optical depths and droplet sizes, liquid water paths, drizzle rates, and cloud top heights were lower than average (plot not shown). As a result, absolute differences in precipitation rates were also small or zero if the clouds were non-raining. As optical depths increased, drizzle rates increased and the effects of pollution had a larger absolute change on precipitation rate. The suppression of precipitation was observed in nearly all of the ship tracks except for those clouds with the largest droplet radii and smallest optical depths, the majority of which were classified as open cellular clouds. This result suggests that the

86

precipitation response depends on the properties of the clouds (droplet size and cloud optical depth) and the mesoscale organization of the cloud field. As shown in Figure 8.1 (right), optically thin clouds with the largest droplets were the most susceptible to fractional changes in cloud optical depth, a result also found in [Segrin et al., 2007] and discussed in detail by [Platnick and Twomey, 1994]. In cases that the pollution plume suppressed drizzle fractional changes in optical depth were noticeably smaller. Therefore, the magnitude of the cloud albedo effect (or fractional change in optical depth) is correlated to some degree by the changes in precipitation associated with the pollution plume from the ship.

8.2. *Microphysical and macrophysical responses*

Is the precipitation response forced by microphysical or macrophysical changes? Precipitation rate has been shown to depend on the microphysical (effective radius) and macrophysical (liquid water path) properties of clouds (e.g., see comprehensive review in Rogers and Yau [1996], pp. 124 − 129, and also, from a more recent study see Kubar et al., [2009]), both of which change, sometimes significantly, in response to aerosol plumes from ships (Part II). Figure 8.2 shows the change in rain rate as a function of the change in liquid water path (left), droplet effective radius (middle), and cloud optical depth (right). Each quadrant in Figure 8.2 (left) represents different liquid water path and precipitation responses to the increased aerosol burden from the ship. The fraction of cases belonging to each quadrant depended strongly on the mesoscale stratocumulus regime. Liquid water paths and precipitation rates were reduced in the majority of ship

tracks identified in the closed cell regime. In the open cell regime, there was a substantial spread in the data throughout all quadrants — this suggests that the precipitation response can be either positive or negative in this regime.

In general, the precipitation and liquid water path response is governed by the competition between the rate of moistening (vertical or horizontal transport of moisture from near the ocean surface) and drying (cloud top evaporation and rainfall). When the atmosphere above the marine stratus deck is sufficiently dry, polluted clouds lose liquid water because of the enhancement in entrainment brought about by their small droplets (Ackerman et al. 2004). This process appears to be occurring for the majority of ship tracks observed in closed cell stratocumulus clouds, where approximately 80% had diminished liquid water paths. Reduced liquid water paths may have been due, in part, to a more statically stable (the LTS was larger by 2.5 K) and dry (average dew point depression was 5 K larger between cloud top to 700 hpa) atmosphere compared to the open cell regime. If the moistening exceeds the loss through entrainment drying and precipitation, liquid water paths increase; this occurred in 75% of the polluted clouds in the open cell regime. This phenomenon has been observed in simulations of ship tracks [Wang and Feingold, 2009], wherein the initial suppression of precipitation allows for the convergence of moisture from below the base of the polluted clouds. Such a local circulation becomes established from the convergence of stationary cold pools that are initiated from the relatively heavy precipitation occurring in the open cells surrounding the ship track. This process may be occurring for cases in the open cell regime, in which the deeper polluted clouds have enhanced rainfall and liquid water paths.

To understand the liquid water path results, changes in droplet effective radius

(middle) and optical depth (right) were also examined (shown in Figure 8.2). In nearly all of the ship tracks, significant decreases in droplet effective radii were observed compared to the surrounding clouds, even for those cases in which rainfall was significantly increased compared to the surrounding clouds. It's noteworthy that the polluted pixels comprising a ship track are determined from the contrast in the 3.7-μm radiances between the ship track and surrounding clouds (Part II). Radiances at this wavelength are sensitive and frequently used to retrieve the size of cloud droplets [Coakley et al., 1987]. Evidently, the magnitude of the difference had no discernible impact upon the changes in precipitation. This was also true of the droplet radii measurements derived from the 2.1-μm radiances.

For the changes in optical depth, it's fairly obvious that these more closely resemble the changes in liquid water path. However, the extent of this change is questionable. As pointed out in Part II, as the fractional cloud coverage decreased, the optical properties of the MODIS retrievals become prone to biases stemming from the partly cloudy pixels. While the degree of these biases remain uncertain, recent studies show that averaging over partly cloudy pixel retrievals (as would be the case for the unpolluted clouds in the open cell regime) leads to an underestimate in cloud optical depth and overestimate in droplet effective radius (e.g.; [Coakley et al., 2005]; [Hayes et al., 2010]). The biases in optical depth and droplet radius compensate somewhat in the estimate of liquid water, but not completely, and often, an underestimate of cloud liquid water occurs in the retrieval of partly cloudy pixels. As a consequence, an apparent increase in cloud liquid water path, cloud optical depth, and cloud albedo is observed in ship tracks residing in open cell cloud regimes. Thus, actual changes in cloud optical

depth are likely smaller than the results suggest. Nonetheless, the differences in liquid water path followed the direction of the precipitation response even when precipitation was suppressed. As a result, drizzle rates can be enhanced or diminished in ship tracks relative to the surrounding clouds, and the change in precipitation is evidently correlated with changes in liquid water path.

To estimate the potential impact of entrainment on the clouds, atmospheric stability and moisture above the boundary layer was analyzed from the ECMWF re-analysis data. Lower troposphere stability and moisture above the boundary layer was calculated using the same method described in Part II. While in general there is good agreement in the estimation of LTS between the Atmospheric Infrared Sounder (AIRS) and ECMWF re-analysis [Yue et al., 2011], LTS represents the bulk state of the atmosphere between the surface and roughly 3 km. Due to the course vertical resolution (250 m) of the ECMWF re-analysis product, the height and strength of a temperature inversion generally found above stratocumulus is poorly resolved. Despite the poor vertical resolution, LTS and cloud top height are reasonably correlated to each other (e.g. see Part II). For example, the LTS calculated from the composite of the shallower non-raining clouds was approximately 2 K higher than the deeper raining clouds. Differences in LTS and moisture above the boundary layer were also noted between closed and open cells (discussed above).

In agreement with Wang and Feingold [2009], reductions in precipitation rates (for those cases with confidence levels greater than the 95th percentile) were observed closer to the head of the ship tracks (211 km), while increases in rainfall were found farther from the head (248 km) on average. Differences here were not statistically significant.

Reduced rainfall rates closer to the heads of ship tracks may suggest that the relative age and lifecycle of polluted clouds are an important variable to consider when assessing aerosol-precipitation interactions. The lifecycle of the cloud microphysics, precipitation, and cold pool development have also been shown to susceptible through increasing the concentration of aerosols in deep convective clouds (e.g., [van den Heever et al., 2006]; [van den Heever and Cotton, 2007]).
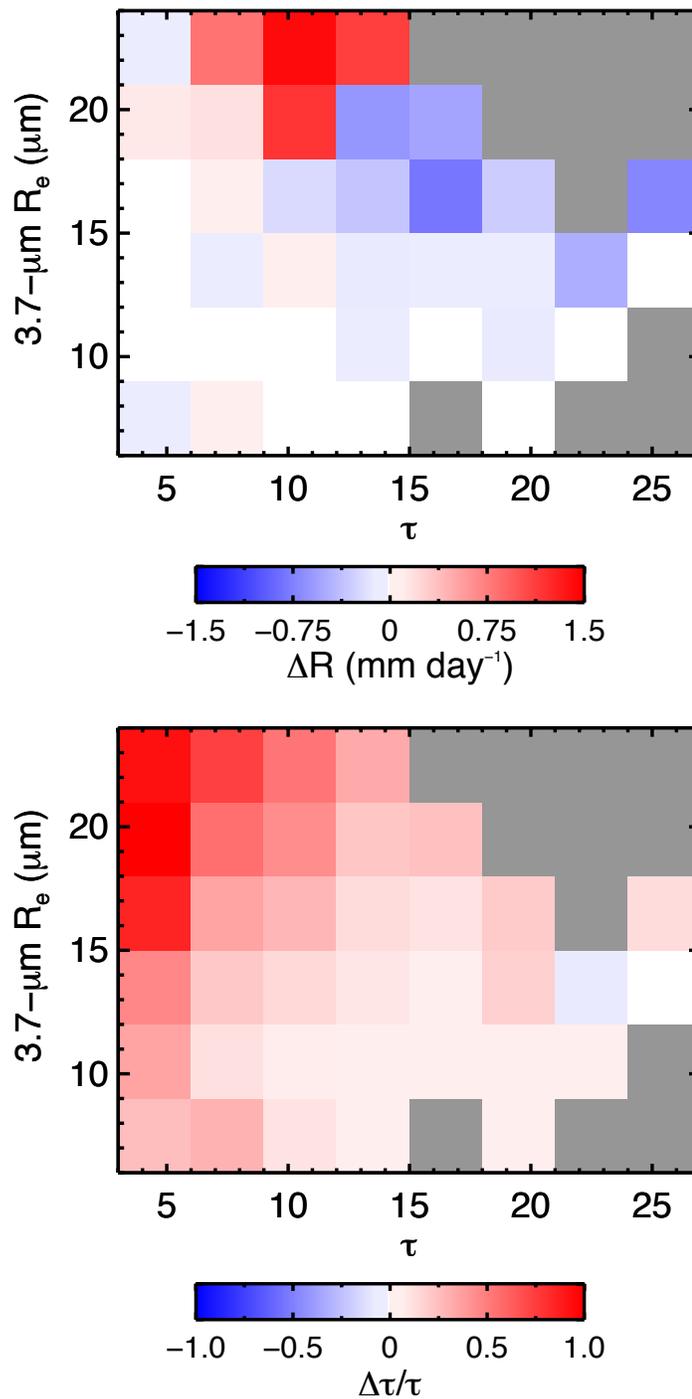
Figure 8.1. (top) Difference in precipitation rate and (bottom) fractional change in optical depth between the polluted and unpolluted clouds as a function of the optical depths and droplet radii in the nearby-unpolluted clouds. A minimum of 5 ship tracks were required for each bin. Zones in gray denote missing data.
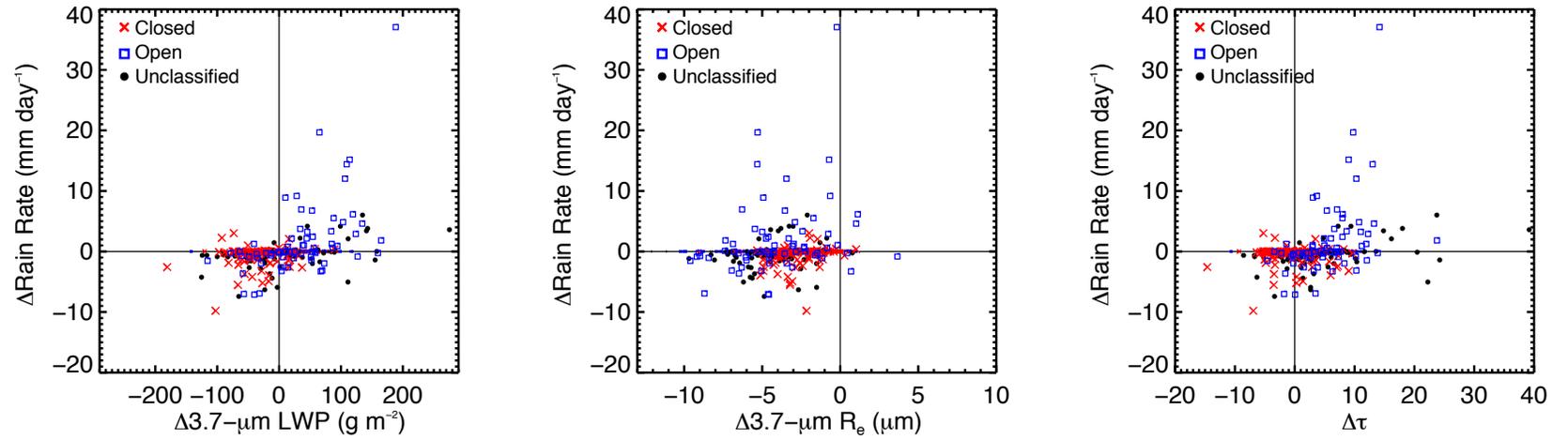
Figure 8.2. Differences in rain rate between the polluted and unpolluted clouds (*SHIP – CONS)* are displayed as a function of the difference in liquid water amount (left), effective radius (middle), and optical depth (right) for the ensembles of closed (red ×), open (blue square), and unclassified (filled black circle) cloud regimes.

CHAPTER 9

CONCLUSIONS

By combination of multiple active and passive remote sensors in the A-Train, several hundred ship tracks were studied to analyze the microphysical and macrophysical changes to marine stratocumulus due to the increased aerosol burden from oceangoing vessels. Accurate measurements of rain rates and cloud top heights were derived using the observations of the CloudSat radar and Calipso lidar, respectively. To increase the confidence of the analysis, multiple regions were used as hunting grounds for ship tracks. By searching for ship tracks across the globe, several were spotted in unexpected cloud types, such as cloud streets and in clouds behind the polar front. Ice was detected in both the MODIS and CALIOP observations; however, the numbers observed were too small to conduct an analysis of the impact of particle pollution on cold clouds. A significantly larger database would be needed for this purpose. The research described here analyzes the largest database of ship tracks observed synergistically by radar and lidar. The main findings from this study include the following:

1. Consistent with past field campaigns (e.g., [Ferek et al., 2000]; [Lu et al., 2009]), the results from this study provide additional evidence that aerosol has the ability to significantly modify rainfall in marine stratocumulus. The response manifested as changes to the spatial extent and intensity of the rainfall, which were closely tied to the mesoscale stratocumulus regime in which the aerosol plumes were ingested. Evidently, the results from the two case studies presented here demonstrate that the precipitation response can either be suppressed or enhanced by the effluents from oceangoing vessels.

2. How often is rainfall suppressed in ship tracks? While the vast majority of the clouds in this study were non-raining, most of ship tracks having detectable rainfall exhibited decreased precipitation compared to the surrounding clouds (an average relative decrease of 72%) especially as the observations became closer in proximity to the emission source from the oceangoing vessel. In addition, significant increases and decreases in rain rate were claimed from numerous individual ship tracks.

3. *Which clouds were most susceptible to a precipitation response?* Clouds with the largest droplets and smallest optical depths, primarily resembling open cellular cloud forms, exhibited a large positive precipitation response. Whereas, for the clouds with large optical depths and small droplets radii (predominately closed cell clouds), precipitation and liquid water paths were greatly reduced. Thus, the direction and magnitude of the precipitation response was strongly influenced by the cloud properties and mesoscale stratocumulus cloud regime.

4. Significant reductions in rainfall were identified in the ship tracks inhabiting closed and unclassified cellular clouds (majority of the clouds identified). The reductions in rainfall were primarily due to a decrease in rain cover fraction and, to a lesser extent, rain intensity. Decreases in radar reflectivity were also observed, suggesting that the number and/or size of drizzle-sizes drops significantly decreased throughout most of the vertical extent of the cloud layer. Aerosol ingested into lightly drizzling closed cellular clouds presumably modified the cloud layer by decreasing precipitation and increasing cloud top entrainment, resulting in drier clouds with virtually no changes in cloud top height and small increases in cloud optical depth. These conclusions were drawn based on the results from large eddy and cloud-system-resolving model simulations performed

by Wang and Feingold, [2009] and Wang et al., [2011], respectively.

5. On the other hand, suppressed precipitation occurred as frequently as enhanced drizzle rates in the clouds polluted by oceangoing vessels in open cellular clouds. Despite the equal frequencies, rain rates were significantly heavier in the ship-contaminated clouds compared to the surrounding open cellular clouds in the ensemble average. Open cellular clouds had the largest cloud droplets and cloud averaged precipitation rates compared to the other stratocumulus regimes. Aerosol plumes ingested into this regime resulted in significantly deeper and brighter clouds with higher liquid water amounts and rain rates. As a result, the aerosol indirect forcing was magnified, but likely exaggerated due to the biases inherent in the MODIS retrievals for clouds at low cloud cover fractions (Part II).

6. *Is the precipitation response forced by microphysical or macrophysical changes?* Microphysical changes almost always led to significantly smaller droplet radii in ship tracks, even when precipitation was increased where the magnitude of the difference had virtually no affect on the precipitation response (no correlation between the differences in droplet size and the differences precipitation between the polluted and unpolluted clouds). In comparison, differences in precipitation were better correlated with the liquid water path response. In agreement with the results from Kubar et al. [2009], macrophysical changes (liquid water path and cloud depth) play a significant role in the direction and magnitude of the precipitation response of low-level warm water clouds.

Marine stratocumuli have been shown to be, in general, highly susceptible to microphysical and macrophysical alterations due to changes in aerosol concentration (e.g. [Platnick and Twomey, 1994]; [Segrin et al., 2007]; [Kubar et al., 2009]). The results

96

presented in this study demonstrate key differences in the precipitation response between stratocumulus regimes and are in qualitative agreement with the results from large eddy simulations performed in Wang and Feingold [2009]. Because the dynamic cloud response to aerosol differs between regimes, cloud type identification is essential for accurately assessing aerosol indirect effects on clouds. Quantifying current distributions of the various marine stratocumulus cloud types and how these might change in the future is thus necessary for gaining confidence in the simulations of aerosol indirect effects in global climate models.

REFERENCES

Ackerman, A. S., O. B. Toon, and P. V. Hobbs (1993), Dissipation of marine stratiform clouds and collapse of the marine boundary layer due to the depletion of cloud condensation nuclei by clouds, Science, 262, 226–229.

Ackerman, A. S., O. B. Toon, J. P. Taylor, D. W. Johnson, P. V. Hobbs, and R. J. Ferek (2000), Effects of aerosols on cloud albedo: Evaluation of twomey's parameterization of cloud susceptibility using measurements of ship tracks, J. Atmos. Sci., 57, 2684–2695.

Ackerman, A. S., M. P. Kirkpatrick, D. E. Stevens, and O. B. Toon (2004), The impact of humidity above stratiform clouds on indirect aerosol climate forcing, Nature, 432, 1014–1017, doi:10.1038/nature03174.

Albrecht, B. A. (1989), Aerosols, cloud microphysics, and fractional cloudiness, Science, 245, 1227–1230.

Atkinson, B. W., and J. W. Zhang (1996), Mesoscale shallow convection in the atmosphere, Rev. Geophys, 34, 403–431.

Baker, M. B., and R. J. Charlson (1990), Bistability of ccn concentrations and thermodynamics in the cloud-topped boundary layer, Nature, 345, 142–145, doi:10.1038/345142a0.

Bretherton, C. S., R. Wood, R. C. George, D. Leon, G. Allen, and X. Zheng (2010), Southeast pacific stratocumulus clouds, precipitation and boundary layer structure sampled along 20° S during vocals-rex, J. Atmos. Chem. Phys., 10, 10,639–10,654, doi:10.5194/acp-10-10639-2010.

Campmany, E., R. G. Grainger, S. M. Dean, and A. M. Sayer (2009), Automatic detection of ship tracks in atsr-2 satellite imagery, J. Atmos. Chem. Phys., 9, 1899–1905, doi:10.5194/acp-9-1899-2009.

Christensen, M. W., and G. L. Stephens (2011), Microphysical and macrophysical responses of marine stratocumulus polluted by underlying ships: Evidence of cloud deepening, J. Geophys. Res., 116, D03201, doi:10.1029/2010JD014638.

Coakley J. A. Jr., R. L. Bernstein, and P. A. Durkee (1987), Effect of ship-stack effluents on cloud reflectivity, Science, 237, 1020–1022, doi:10.1126/science.237.4818.1020.

Coakley J. A. Jr., et al. (2000), The appearance and disappearance of ship tracks on large spatial scales, J. Atmos. Sci., 57, 2765–2778.

Coakley J. A. Jr., M. A. Friedman, and W. R. Tahnk (2005), Retrieval of cloud properties for partly cloudy imager pixels, J. Atmos. Oceanic. Technol., 22, 3–7, doi:10.1175/JTECH-1681.1.

Conover J. H. (1966), Anomalous cloud lines, J. Atmos. Sci, 23, 778 – 785.

Comstock, K. K., C. S. Bretherton, and S. E. Yuter (2005), Mesoscale variability and drizzle in southeast pacific stratocumulus, J. Atmos. Sci., 62, 3792–3807, doi:10.1175/JAS3567.1.

Comstock, K. K., S. E. Yuter, R. Wood, and C. S. Bretherton (2007), The three-dimensional structure and kinematics of drizzling stratocumulus, Mon. Weather Rev, 135, 3767–3784, doi:10.1175/2007MWR1944.1.

Ferek, R. J., et al. (2000), Drizzle suppression in ship tracks., J. Atmos. Sci., 57, 2707–2728.

Hawkness-Smith, L. D. (2010), A novel retrieval of liquid water path and an evaluation of the representation of drizzle in numerical models, Ph.D. thesis, UNIVERSITY OF READING.

Hayes, C. R., J. A. Coakley Jr., and W. R. Tahnk (2010), Relationships among properties of marine stratocumulus derived from collocated calipso and modis observations, J. Geophys. Res., 115, D00H17, doi:10.1029/2009JD012046.

Haynes, J. M., T. S. L'Ecuyer, G. L. Stephens, S. D. Miller, C. Mitrescu, N. B. Wood, and S. Tanelli (2009), Rainfall retrieval over the ocean with spaceborne W-band radar, J. Geophys. Res., 114, D00A22, doi:10.1029/2008JD009973.

IPCC (2007), Climate Change 2007: The Physical Science Basis. Contribution of Working Group I to the Fourth Assessment Report of the Intergovernmental Panel on Climate Change. [Solomon, S., D. Qin, M. Manning, Z. Chen, M. Marquis, K.B. Averyt, M.Tignor and H.L. Miller (eds.)], Cambridge University Press, Cambridge, United Kingdom and New York, NY, USA.

Kraus, E. B., and P. Squires (1947), Experiments on the stimulation of clouds to produce rain, Nature, 159, 489–491, doi:10.1038/159489a0.

Kubar, T. L., D. L. Hartmann, and R. Wood (2009), Understanding the importance of microphysics and macrophysics for warm rain in marine low clouds. part i: Satellite observations, J. Atmos. Sci., 66, 2953–2972, doi: 10.1175/2009JAS3071.1.

Lebsock, M. D., G. L. Stephens, and C. Kummerow (2008), Multisensor satellite observations of aerosol effects on warm clouds, J. Geophys. Res., 113, D15205, doi:10.1029/2008JD009876.

Lebsock, M. D., T. S. L'Ecuyer, and G. L. Stephens (2011), Detecting the ratio of rain and cloud water in low-latitude shallow marine clouds, J. Appl. Meteor. Climatol, 50, 419–432, doi: 10.1175/2010JAMC2494.1.

Liu, Q., Y. L. Kogan, and D. K. Lilly (2000), Modeling of ship effluent transport and its sensitivity to boundary layer structure, J. Atmos. Sci., 57, 2779–2791.

Lu, M.-L., A. Sorooshian, H. H. Jonsson, G. Feingold, R. C. Flagan, and J. H. Seinfeld (2009), Marine stratocumulus aerosol-cloud relationships in the mase-ii experiment: Precipitation susceptibility in eastern pacific marine stratocumulus, J. Geophys. Res., 114(D24203), D10209, doi:10.1029/2006JD007985.

Marchand, R., G. G. Mace, T. Ackerman, and G. Stephens (2008), Hydrometeor detection using cloudsat — an earth-orbiting 94-ghz cloud radar, J. Atmos. Oceanic Technol, 25,519–533, doi:10.1175/2007JTECHA1006.1.

McNicholas, M. (2008), Maritime Security: An Introduction, Butterworth-Heinemann (Elsevier), Burlington, MA. Paluch, I. R., and D. H. Lenschow (1991), Stratiform cloud formation in the marine boundary layer, J. Atmos. Sci., 48, 2141–2158. Platnick, S., and

Paluch, I. R., and D. H. Lenschow (1991), Stratiform cloud formation in the marine boundary layer, J. Atmos. Sci., 48, 2141–2158.

Platnick, S., and S. Twomey (1994), Determining the susceptibility of cloud albedo to changes in droplet concentration with the advanced very high resolution radiometer, J. Appl. Meteor, 33, 334–347

Quaas, J., O. Boucher, N. Bellouin, and S. Kinne (2008), Satellite-based estimate of the direct and indirect aerosol climate forcing, J. Geophys. Res., 113, D05204, doi:10.1029/2007JD008962.

Rogers, R. R., and M. K. Yau, (1996), A short course in cloud physics, 3rd ed., Butterworth-Heinmannn, Woburn, Mass.

Savic-Jovcic, V., and B. Stevens (2008), The structure and mesoscale organization of precipitating stratocumulus, J. Atmos. Sci., 65, 1587–1605, doi:10.1175/2007JAS2456.1.

Schreier, M., H. Mannstein, V. Eyring, and H. Bovensmann (2007), Global ship track distribution and radiative forcing from 1 year of aatsr data, Geophys. Res. Lett, 34, L17814, doi:10.1029/2007GL030664.

Segrin, M. S., J. A. Coakley Jr., and W. R. Tahnk (2007), Modis observations of ship tracks in summertime stratus off the west coast of the united states, J. Atmos. Sci., 64,

4330–4345, doi:10.1175/2007JAS2308.1.

Sorooshian, A., G. Feingold, M. D. Lebsock, H. Jiang, and G. L. Stephens (2009), On the precipitation susceptibility of clouds to aerosol perturbations, Geophys. Res. Lett., 36, L13803, doi:10.1029/2009GL038993.

Stephens, G. L. (1978), Radiation profiles in extended water clouds. ii: Parameterization schemes, J. Atmos. Sci., 35, 2123–2132.

Stephens, G. L. (2005), Cloud feedbacks in the climate system: A critical review, J. Clim.18, 237–273, doi:10.1175/JCLI-3243.1.

Stephens, G. L., and T. Slingo (1992), An air-conditioned greenhouse, Nature, 358, 369–370, doi:10.1038/358369a0.

Stephens, G. L., et al. (2008), The CloudSat mission: performance and early science after the first year of operation, J. Geophys. Res., 113, D00A18, doi:10.1029/2008JD009982.

Stevens, B., and G. Feingold (2009), Untangling aerosol effects on clouds and precipitation in a buffered system, Nature, 461, 607–613, doi:10.1038/nature08281.

Taylor, J. P., and A. S. Ackerman (1999), A case-study of pronounced perturbations to cloud properties and boundary-layer dynamics due to aerosol emissions, Q. J. Royal. Meteorol. Soc., 125, 2643–2661, doi: 10.1002/qj.49712555915.

Twomey, S. (1974), Pollution and the planetary albedo, Atmos. Environ., 8, 1251–1256.

van den Heever, S. C., G. G. Carrio, W. R. Cotton, J. P. DeMott, and A. J. Prenni (2006) Impacts of nucleating aerosol on florida storms. Part I: Mesoscale simulations. J. Atmos. Sci., 63, 1752 – 1775.

van den Heever and W. R. Cotton (2007) Urban aerosol impacts on downwind convective storms, J. Atmos. Sci., 46, 828 – 850.

Wang, H., and G. Feingold (2009), Modeling mesoscale cellular structures and drizzle in marine stratocumulus. part ii: The microphysics and dynamics of the boundary region between open and closed cells, J. Atmos. Sci., 66, 3257–3275, doi:10.1175/2009JAS3120.1.

Wang, H., G. Feingold, R. Wood, and J. Kazil (2010), Modelling microphysical and meteorological controls on precipitation and cloud cellular structures in southeast pacific stratocumulus, J. Atmos. Chem. Phys., 10, 6347–6362, doi:10.5194/acp-10-6347-2010.

Wang, H., P. J. Rasch, and G. Feingold (2011), Manipulating marine stratocumulus cloud

amount and albedo: a process-modelling study of aerosol-cloud-precipitation interactions in response to injection of cloud condensation nuclei, Atmos. Chem. Phys., 11, 4237—4249, doi:10.5194/acp-11-4237-2011.

Warren, S. G., C. J. Hahn, H. J. London, R. M. Chervin, and R. L. Jenne (1988), Global distribution of total cloud cover and cloud type amounts over the ocean, NCAR tech. Note, NCAR/TN-317+STR, 41pp.+170 maps.

Wood, R. (2005), Drizzle in stratiform boundary layer clouds. part i: Vertical and horizontal structure, J. Atmos. Sci., 62, 3011–3033, doi:10.1175/JAS3529.1.

Wood, R., and C. S. Bretherton (2004), Boundary layer depth, entrainment and decoupling in the cloud-capped subtropical and tropical marine boundary layer, J. Climate, 17, 3576–3588.

Wood, R., and D. L. Hartmann (2006), Spatial variability of liquid water path in marine low cloud: the importance of mesoscale cellular convection, J. Climate, 19, 1748–1764, doi: 10.1175/JCLI3702.1.

Wood, R., T. L. Kubar, and D. L. Hartmann (2009), Understanding the importance of microphysics and macrophysics for warm rain in marine low clouds. part ii: Heuristic models of rain formation, J. Atmos. Sci., 66, 2973–2990, doi:10.1175/2009JAS3072.1.

Wood, R., et al. (2011), The vamos ocean-cloud-atmosphere-land study regional experiment (vocals-rex): goals, platforms, and field operations, J. Atmos. Chem. Phys., 11, 627–654, doi:10.5194/acp-11-627-2011.

Yue, Q., B. H. Kahn, E. J. Fetzer, and J. Teixeira (2011), Relationship between marine boundary layer clouds and lower troposphere stability observed by airs, cloudsat, and caliop, J. Geophys. Res., 116, D18212, doi:10.1029/2011JD016136.

PART IV: CANCELLATION OF AEROSOL INDIRECT EFFECTS AS OBSERVED IN SHIP TRACKS

CHAPTER 1

INTRODUCTION

Over the past few decades, numerous discoveries have begun to shed light on the cloudy view of aerosol indirect effects in the climate system (Twomey, [1974], Albrecht, [1989], Ackerman et al., [2004], Wood et al., [2007]). Although many studies disagree on the magnitude and even the sign of the cloud albedo response to increases in aerosol concentration, this ambiguity has led to a number of insights on the response which points to an aggregated indirect effect. The aggregated indirect effect is the result of a number of different cloud feedbacks (such as changes in drizzle rates, cloud top entrainment, and boundary layer coupling) that alter the microphysical and macrophysical properties of clouds in response to changes in aerosol concentration – feedbacks that are poorly represented climate models causing great disparity amongst projections of future climate change (e.g., [Stephens 2005]; [IPCC, 2007]).

Processes at the heart of the aggregated indirect effect can be divided into a quasi-instantaneous radiative forcing (formally known as the Twomey effect) and an adjustment to the forcing by way of the clouds interaction with the environment. The forcing is considered quasi-instantaneous because the timescale over which the cloud microphysics adjusts to changes in aerosol concentration is rapid (on the order of minutes [Durkee et al., 2000]) compared to the macrophysical adjustment timescale (on the order of hours [Bretherton et al., 2010]). In the quasi-instantaneous process, clouds are macrophysically identical (i.e. same liquid water path, cloud depth, cloud coverage, and precipitation rate) and increases in cloud condensation nuclei (CCN) enhance the

104

reflectivity of the cloud [Twomey, 1974]. On the other hand, macrophysical adjustments can either enhance or diminish the cloud brightening response to increases in aerosol particles. One of the challenges in understanding the cloud macrophysical responses lies in untangling the aerosol effects from other processes, such as the meteorological influence on the clouds.

By utilizing accurate measurements from a suite of sensors in the A-Train and, data from a recent ship track campaign, we attempt to determine the regulating processes that determine the sign and magnitude of the aerosol indirect forcing in ship tracks. In this part of the dissertation a radiative transfer model lookup table was used in conjunction with the retrieved cloud properties from the Moderate Resolution Imaging Spectroradiometer (MODIS) to calculate the albedo of clouds (described in chapter 2) and, to determine the atmospheric conditions that enhance/cancel the aerosol indirect radiative forcing as deduced from ship tracks (described in chapter 3). In addition, in situ observations of ship tracks recently measured in the Eastern Pacific Emitted Aerosol Cloud Experiment (E-PEACE) campaign were incorporated as a means of comparing the satellite observations and theory to aerosol-cloud brightening. Finally, a conceptual model of plume affects in the four most commonly observed stratocumulus cloud types (having ship tracks) are discussed.

CHAPTER 2

METHODOLOGY

The same database of ship tracks described in Part III and Christensen and Stephens, [2012], was used in this study to determine the atmospheric conditions that promote negative and positive cloud albedo responses in marine stratocumulus. Cloud albedo was calculated using a lookup table that was generated using the BUGSrad [Stephens, 2001], a two-stream radiative transfer model. Visible cloud optical depth, 3.7-μm droplet effective radius, and the solar zenith angle were used as inputs for the lookup table. These variables were derived using MODIS cloud product. All of the other parameters used to calculate the cloud top height, thermodynamic profiles of temperature and humidity, free-tropospheric moisture content, precipitation, and the type of mesoscale cloud coverage were the same as those described in Part III and Christensen and Stephens, [2012].

Understanding how cloud albedo responds to increases in droplet concentration was a goal that was similarly shared by those conducting the E-PEACE campaign. E-PEACE was carried out in July and August 2011 over the eastern Pacific adjacent to the coast of Monterey, California. This campaign was the first to deliberately seed cloud through the controlled release of aerosol in three different size ranges of particles by flight and on a dedicated ship. A full payload of state-of-the-art aerosol and cloud instrumentation measurements were made below, in, and above clouds using the Center for Interdisciplinary Remotely-Piloted Aircraft Studies (CIRPAS) Twin Otter aircraft.

Results from four ship tracks were used to demonstrate the effect of the thermodynamic conditions that affect aerosol-cloud microphysics and macrophysics.

We introduce cloud susceptibility [Platnick and Twomey, 1994], defined as the sensitivity of cloud albedo to changes in droplet concentration, to understand the magnitude of the aerosol indirect effect. In the Monterey Area Ship Track (MAST) experiment, ship tracks were observed in a variety of clean and moderately polluted environments. Two key insights were observed: first, fewer ship tracks were identified as the background became more polluted despite the abundant ship vessel traffic, and second, increases in cloud albedo caused by the ship plume were often muted in polluted environments. Muted indirect radiative effects have similarly been identified in deep convective clouds downwind of urban areas when the background aerosol concentration was relatively high [van den Heever and Cotton, 2007]. One conclusion to be reached was that the extent of the cloud brightening, to a large degree, depended on the susceptibility of the cloud to the addition of cloud droplets. In addition, ship tracks were commonly observed when the engines were burning diesel fuel. Engines that burn diesel fuel produce an order of magnitude more cloud condensation nuclei than those running on steam or gas turbine fuels.

Cloud susceptibility can be expressed in terms of the cloud optical depth using the chain rule

$$\frac{dA}{dN} = \frac{dA}{d\tau}\frac{d\tau}{dN}, \tag{1}$$

where τ is the cloud optical depth, A is the cloud albedo, and N is the number droplet concentration. Equation (1) holds under the assumption that the clouds are nonabsorbing at visible wavelengths ($0.3 - 0.7$ μm) and the asymmetry parameter (g) remains constant.

Cloud optical depth can be expressed as $\tau = 2\pi r^2 Nh$, where r is the average radius, and h is the cloud depth under the assumption that the cloud droplets are spherical and scatter radiation in the geometric limit. Similarly, the liquid water content can also be estimated as $L=(4/3)\pi\rho Nr^3$ and the average radius can be related to the effective radius through $r^3 = kr_e^3$ [Martin et al., 1994], where k is a measure of the drop size distribution (i.e., a value of 1 would indicate a monodisperse droplet size distribution) and the measured values during E-PEACE were approximately 0.75. Upon combining L and r, cloud optical depth can be written as

$$\tau = 2\pi\left(\frac{3L}{4\pi\rho}\right)^{2/3}(kN)^{1/3}h, \tag{2}$$

where taking the derivative with respect to N, gives

$$\frac{d\tau}{dN} = \frac{\tau}{3N}\left(1 + 2\frac{d(\ln L)}{d(\ln N)} + \frac{d(\ln k)}{d(\ln N)} + 3\frac{d(\ln h)}{d(\ln N)}\right), \tag{3}$$

where the right hand side forms one of the differentials in equation (1). Here it can be seen that changes in the liquid water content, droplet size distribution, or cloud depth can decrease, or possibly even reverse the sign of the cloud optical depth response to increasing the droplet concentration. To derive $dA/d\tau$, an expression for the albedo of a cloud can be obtained using the Eddington approximation of the two-stream radiative transfer equation, i.e., $A \cong (1-g)\tau/[2+(1-g)\tau]$. Taking the derivative of τ with respect to

N yields $\dfrac{dA}{d\tau} = \dfrac{A(1-A)}{\tau}$, and when multiplied by equation (3), the cloud susceptibility follows as

$$\frac{dA}{dN} \cong A(1-A)\frac{1}{3N}\left(1 + 2\frac{d(\ln L)}{d(\ln N)} + \frac{d(\ln k)}{d(\ln N)} + 3\frac{d(\ln h)}{d(\ln N)}\right), \tag{4}$$

where $d(\ln L)/d(\ln N)$ and $d(\ln h)/d(\ln N)$ remain constant under quasi-instantaneous

changes. Under this assumption (Twomey effect), the cloud albedo response is simply a

function of the changes in number concentration as

$$\frac{\Delta A}{A(1-A)} = \frac{1}{3}\Delta(\ln N), \tag{5}$$

or expressed in terms of the cloud optical and geometric properties as

$$\frac{dA}{dN} = \frac{2\pi}{9}A(1-A)\frac{r^2 h}{\tau}, \tag{6}$$

where the droplet size (r), cloud thickness (h), and cloud optical depth (τ) largely control

the cloud susceptibility. Thus, changes in cloud albedo scale with the changes in cloud

droplet concentration. Figure 8.2 of Part III demonstrates this effect wherein the plumes

affect on cloud albedo (or fractional change in cloud optical depth) has the largest

sensitivity on the optically thinnest clouds with the largest droplets.

Because the study focuses on the changes in cloud albedo, and not the changes in

cloud top height or precipitation as was the focus in Part III, a slightly stricter screening

procedure of the MODIS cloud optical properties was invoked to remove potential biases

stemming from partly cloudy pixels. First, the controls on both sides of the ship track

domain were required for the analysis and, each segment needed to have a minimum of

thirty 1-km pixels. Second, the cloud cover fraction needed to be larger than 95% when

averaged over the ship track and control pixels to reduce biases stemming from 3D

effects and photon leakage out of the sides of clouds. After screening, 589 ship tracks

remained allowing for a thorough assessment of the effect of particle pollution on the

albedo of stratocumulus.

CHAPTER 3

RESULTS

3.1. *Pathways of the cloud albedo response*

Out of 589 cases, roughly 75% of the ship tracks had a higher cloud albedo than the ambient clouds. Figure 3.1 shows the distribution of the mean cloud albedo responses, i.e. $\Delta A/[A(1-A)]$ left hand side of equation (5), for the entire ensemble of ship tracks. While the majority of cases were susceptible to cloud brightening, 25% of the ensemble had polluted clouds that were dimmer than their unpolluted counterparts. We thus, attempt to answer the following question: *Why does cloud dimming occur in ship tracks?*

To a large extent, changes in droplet number concentration and cloud liquid water path influence the magnitude and sign of the cloud albedo response. To first order, differences in cloud liquid water path were responsible for the magnitude and sign of the cloud albedo response as depicted in Figure 3.2a. In situ observations from the E-PEACE campaign tended to reside within the distribution of the ship tracks examined from this study with the exception of one outlier in which heavy drizzle was measured was in an open cellular regime. When the polluted and unpolluted clouds were macrophysically similar (i.e., red dots in Figures 3.2(left) and Fig. 3.2.(right) determined by the absolute value of the fractional change in liquid water amounts and cloud top heights being less than 5%) the fit between the cloud albedo responses and the log difference of N was strongly correlated to that predicted by the Twomey equation (5). N was simply estimated using the optical depth equation (i.e., $\tau = 2\pi r^2 Nh$) where h was assumed to be the cloud top height and the effective radius was substituted for the average radius. This

relationship is shown in Figure 3.2 (right) with a slope having the value of 1/3. Roughly 30% of the ship tracks resided in this quasi-instantaneous regime. Because macrophysical changes were negligible under this assumption, differences in cloud albedo between the polluted and unpolluted clouds (red dots) resulted primarily from the increased concentration of smaller cloud drops. When the macrophysical differences between perturbed and unperturbed clouds were larger (black dots in Figure 3.2 [left], in which clouds interact with the environment, leading to changes in liquid water path), the differences in liquid water path govern the sign and strength of the cloud albedo response. In some ship tracks, the albedo enhancement was diminished to the point where complete cancellation occurred due to dramatic decreases in liquid water path. Many ship tracks stood out significantly above and below the slope of the line in Figure 3.2b indicating that substantial adjustments were made to the cloud albedo response in a number of ship track cases.

Because equation (5) does not predict a negative cloud albedo response, ship tracks were separated into two categories: those with enhanced albedo (cloud brightening) and those with diminished albedo (cloud dimming) compared to the surrounding clouds. Figure 3.3 shows the distributions of the mean free-tropospheric moisture content, cloud top height, cloud effective radius, and cloud optical depth for each composite. Polluted clouds were brighter than the surrounding unpolluted clouds when they were embedded in shallower cloud decks with relatively moist air above the cloud tops. Observations from E-PEACE measurements of ship tracks confirm that cloud brightening occurred when the humidity was relatively high in the free-troposphere. In addition, clouds that became brighter in response to the plume were optically thinner and

contained larger droplets than those in which a dimming effect occurred. These clouds were also commonly identified in collapsed marine boundary layers and open cellular clouds. In the closed and unclassifiable cellular regimes, cloud brightening occurred less frequently (70%) and the air above the cloud tops was dry in comparison.

To understand why the cloud albedo response was highly correlated to the depth of the marine boundary layer, Figure 3.4a shows the trend of the response as a function of the cloud top height averaged over the unpolluted clouds. Data was binned into height increments of 200 m and averages were removed from the plot if the bin contained less than twenty ship tracks. Microphysical (fractional change in effective radius) and macrophysical (fractional change in liquid water path and cloud top height) responses were included on the figure to demonstrate causality. As the marine boundary layer deepened, fractional changes in liquid water path between the polluted and unpolluted clouds became progressively more negative. Clouds in deeper boundary layers were thus, prone to losing liquid water when polluted by the ship plume. Similar reductions in the cloud top height response were also observed (yellow line), however these changes were modest by comparison.

Differences in effective radius remained relatively constant as the boundary layer depth increased. This surprising result contrasts with the expectation that the affect on cloud microphysics should decrease since the ship plume becomes more diluted in a deeper boundary layer (e.g., [Durkee et al., 2000]; [Wood, 2007]). First, a deeper boundary layer causes greater dispersion and dillution of the ship plume before reaching cloud base. In fact, the dilution of the plume is approximately linearly proportional to the distance from the cloud layer to the exhaust stack of the ship (e.g., see Fig.6. in Durkee et

al., [2000]). In addition, deeper boundary layers are more susceptible to decoupling in which an internally stratified stable layers can prevent the plume from reaching cloud base [Liu et al., 2000]. The frequency in which ship tracks can form under varying degrees of boundary layer coupling has yet to be explored from an observational perspective.

Because the albedo response closely followed the liquid water path response, the affect of aerosol on cloud brightening decreased as the boundary layer deepened. In fact, beyond about 1.2 km, the exhaust plume exhibited virtually no impact upon the cloud albedo and, above this altitude, cloud dimming began to take over on average. Similarly, Figure 3.4b shows that as the moisture content in the free-troposphere decreased, larger negative adjustments to the cloud albedo occurred due to the greater loses in liquid water path. The dependence of cloud top height and free-tropospheric moisture content on the cloud albedo response, in general, agrees with the results of the E-PEACE campaign and, those found by Wood, [2007].
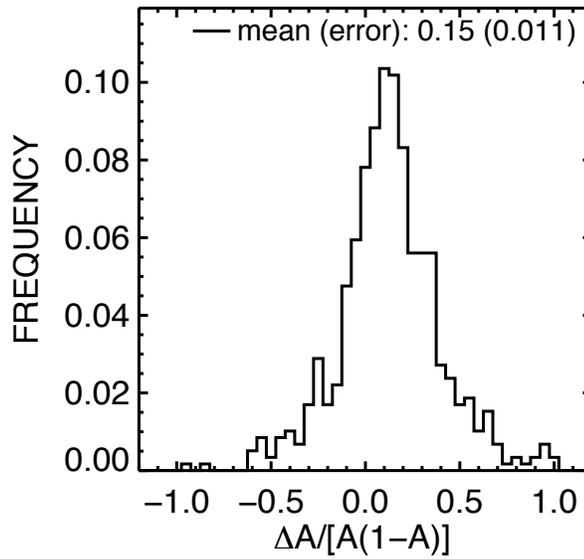
Figure 3.1. Average cloud albedo response (ΔA/[A(1-A)]) from the ensemble of ship tracks used in Christensen and Stephens, [2012].
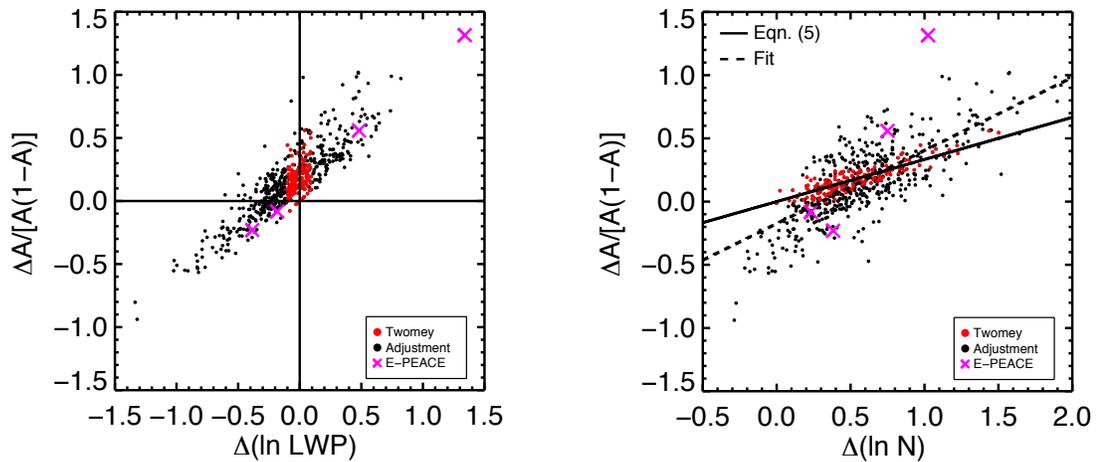
Figure 3.2. Scatter plot of the cloud albedo response plotted against the (left) changes in liquid water path (LWP) and (right) cloud droplet concentration (N). Cloud droplet concentration was calculated by solving for N using the cloud optical depth equation. In the E-PEACE campagin, cloud albedo was calculated from the measurement of cloud optical depth (i.e., $A = \tau/[7.7+\tau]$).
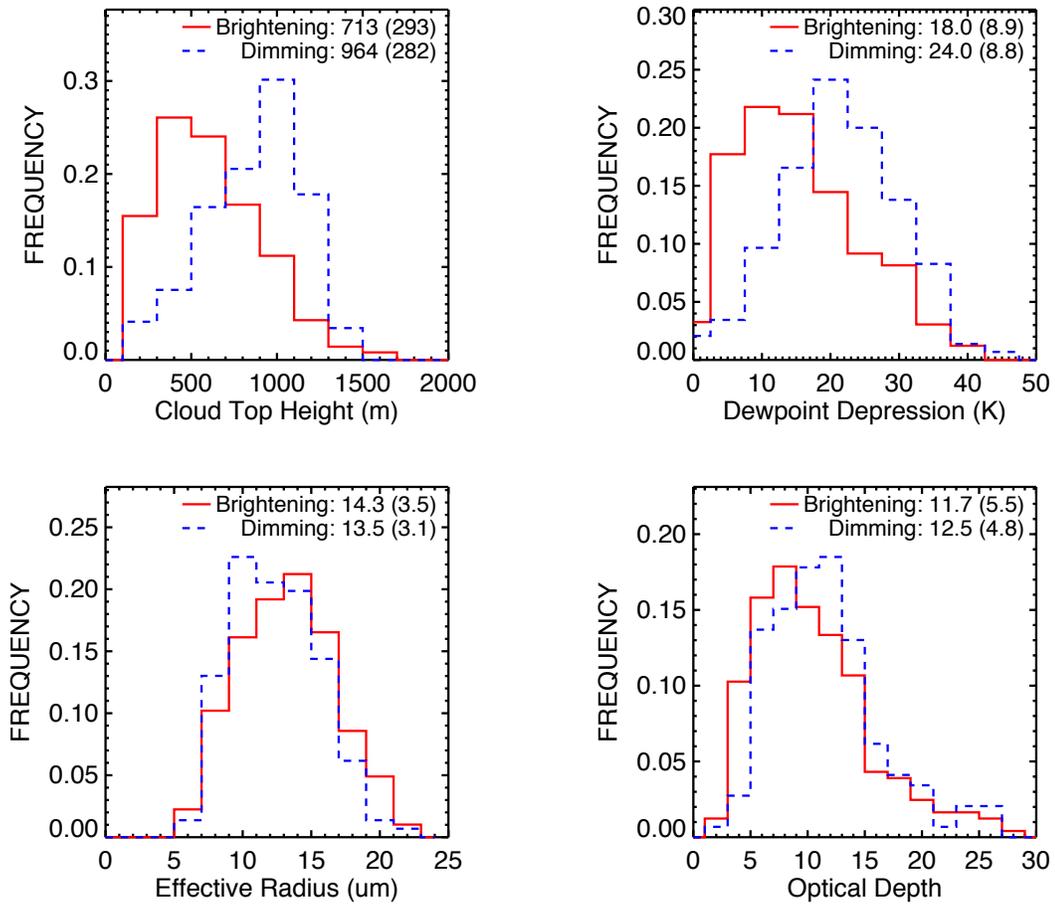
Figure 3.3. Frequency distribution of mean (a) cloud top height, (b) dew point depression, (c) effective radius, and (d) optical depth for 589 individual ship tracks from June 2006 – December 2009 A-Train observations. Cloud brightening and cloud dimming cases are shown by red and blue lines, respectively. Means and (standard deviations) are given at the top of each panel.
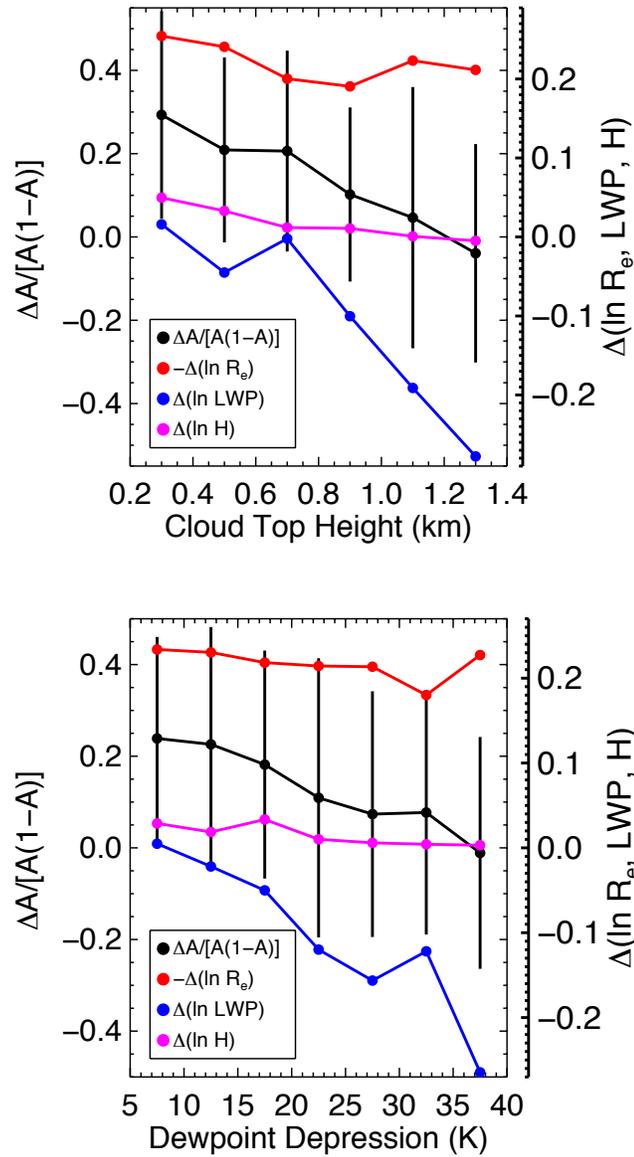
Figure 3.4. Binned change in albedo, effective radius (R_e), LWP, and cloud thickness (H) as a function of cloud top height (left panel), and dew point depression (right panel) based on 589 ship tracks observed over June 2006 – December 2009. Cases were binned by 200 m in cloud top height and 5 K in dewpoint depression. A minimum of 20 ship tracks were required for each bin.

3.2. Role of mesoscale convection on the cloud albedo response

Classifying clouds according to their appearance has long been a useful indicator for predicting weather and inferring the movement of air in the atmosphere. It is remarkable that, through simply observing the type and relative size of the cellular structures in stratocumulus clouds we may gain some semblance of the thermodynamic conditions, depth of the marine boundary layer, and precipitation – processes which play a key role in regulating the cloud albedo response to changes in aerosol concentration. In this section, we attempt to establish causal links of the direction and magnitude of the aerosol indirect radiative forcing in ship tracks inhabiting commonly observed stratocumulus cloud regimes.

Shallow clouds in collapsed marine boundary layer are perhaps the most susceptible clouds on Earth to an enhancement in cloud albedo caused by the pollution plumes from oceangoing vessels. A spectacular depiction of this interaction is shown in Figure 3.5a and b. Ship tracks were observed in collapsed boundary layers in approximately 15% of cases. Because this system has only been examined in one case study [Taylor and Ackerman, 1999], little is actually known about its formation and evolution. Numerical model simulations reveal that when cloud condensation nuclei reach extremely low values through droplet collisions and drizzle, clouds can become so optically thin that radiative cooling cannot drive a mixed layer and, the cloud layer collapses to a shallow fog [Ackerman, 1993]. Under these conditions, the effluents from the ships can replenish the concentration of CCN and rejuvenate cloud top radiative cooling and entrainment throughout the depth of the boundary layer. As a consequence, clouds in this pristine environment undergo significant reductions in droplet size and

117

significant increases in cloud liquid water path, both of which contribute to a significant

enhancement in cloud albedo. Table 3.1 lists the mean atmospheric conditions and cloud

properties for each cloud regime.

Figure 3.5 shows a true color satellite image of a collapsed boundary layer using

MODIS and, a conceptual diagram is provided illustrating the transformation of the cloud

layer in response to the ship plume. Many of the cloud regimes in previous parts were not

explicitly labeled as collapsed marine boundary layers and, were grouped into the

unclassifiable regime. For a boundary layer to be collapsed, two things had to be true: 1st,

the ship track needed to be observable using only the visible (0.64 μm) wavelengths on

MODIS and, the ship track needed to be significantly wider than the cells in the

surrounding clouds. Collapsed boundary layers tend to exhibit the appearance of an open

cellular cloud system, however the sizes of the cells are typically on the order of 1 – 2

km. The dispersion rates (widening of the ship track as a function from the distance to the

head) were very rapid in the cloud system – an indication that the entrainment rates were

likely greatly invigorated in the ship track compared to the ambient clouds. Because the

average amount of moisture above the collapsed boundary layer was higher than the other

cloud regimes, the invigorated entrainment in the ship track likely enabled it to deepen

and accumulate liquid water compared to the surrounding clouds. In addition, ship tracks

had the greatest average lengths in this regime, suggesting that polluted clouds may last

longer in collapsed boundary layers.

While scanning through several images, it was often noted that cirrus was found

overlying a collapsed boundary layer and, most of these systems occurred across the

Northern Pacific Ocean, while relatively few were found in the Southern Oceans. In

addition, collapsed boundary layer clouds had the highest average levels of free tropospheric moisture compared to the other analyzed cloud regimes. Abundant free-tropospheric moisture and/or cirrus reduces the boundary layers ability to cool (e.g.; [Chen and Cotton, 1987]; [Christensen et al., *in prep*]), and hence, may aid in its collapse.

Closed cellular clouds exhibited positive and negative cloud albedo responses to increased aerosol and the response primarily depended on the optical and geometrical properties of the clouds, as well as the amount of moisture above the boundary layer. Because ship tracks were frequently observed in closed cells (up to 45%), it is thus essential to understand the causes of this mixed albedo response. Figure 3.7a and b shows a visible and near infrared satellite image of a ship track in a closed cellular system. Evidently, the ship track is difficult to detect when using only visible bands in the electromagnetic spectrum. The difficulty arises for two reasons: first, the background clouds were highly reflective providing weak contrast between the ship track and surrounding clouds. Second, the enhancement in cloud albedo was small (less than 2%) due to the large losses in liquid water path that occurred in this case, and many like it in closed cellular clouds (Parts II and III). The ship track stands out in the near infrared because water vapor begins to absorb radiation at these wavelengths thereby providing a higher degree of contrast between the smaller droplets that absorb less of this radiation in the ship track compared to the ambient clouds [Coakely et al., 1987].

When ship tracks were detected in a shallow boundary layer (Figure 3.7 c) (approximately less than 500 m) composed of closed cells, both the polluted and unpolluted clouds were commonly non-raining. Unlike the optically thin clouds in a collapsed marine boundary layer ($\tau = 7.8$), optically thicker clouds in the closed cell

119

regime ($\tau = 14.7$) generate more buoyant turbulence production (through stronger cloud top radiative and evaporative cooling) that drives turbulence through the depth of the shallow boundary layer. The cloud layer is thus, connected to the rich supply of moisture near the ocean surface through this mixing. Under this condition, the losses in liquid water path are small in the ship track compared to the surrounding clouds and the enhancement in cloud albedo follows the increase predicted by the Twomey effect. Figure 3.7c illustrates the processes occurring in a shallow closed cell boundary layer.

A possible cause for the negative adjustment in deeper closed cellular cloud systems (deeper than 1 km) may have arisen from the invigorated cloud top entrainment rates in the polluted clouds when the air above the boundary layer was sufficiently dry – a similar result found in the large eddy simulations performed by Ackerman et al., [2004] – and by subcloud layer decoupling. The relative humidity above the deeper closed cell boundary layer clouds was significantly lower (dewpoint depression = 21.5 K) than those found in a shallow boundary layer (dewpoint depression = 12.7 K). A deeper boundary layer is also prone to decoupling produced by the subcloud evaporative cooling from drizzle (shown in Figure 3.7b) [Wood and Bretherton, 2004]. Evaporative cooling from drizzle produces a stable layer that can, under certain conditions when the drizzle reaches the surface, inhibit turbulent mixing throughout the depth the boundary layer [Lewellen and Lewellen, 2002]. Under these conditions, closed cell clouds that are deeper and decoupled from the ample supply of near surface moisture may have been more susceptible to reductions in cloud liquid water content by the aerosol plume [Wood, 2007]. In addition, the exhaust plume had to travel farther to reach the cloud base,

thereby becoming diluted in the processes and limiting its effect on cloud microphysics [Durkee et al., 2000].

In the open cellular cloud regime, drizzle plays a central role in depleting cloud condensation nuclei from the boundary layer [Wood, 2006] promoting larger drizzle rates and cloud droplets compared to other cloud regimes (Part III). Due to subcloud evaporation of the drizzle, the boundary layer of an open cellular system exhibits a high degree of decoupling from surface moisture, except in the cloud walls where the convergence of neighboring cold pools cause locally enhanced updrafts [Wang and Feingold, 2009a]. When a ship passes through a pocket of open cells rainfall is initially suppressed from the plume of aerosols and, cold pools driven by precipitation in the unaffected open cells converge below the ship track, forming a local circulation. With stronger updrafts, precipitation later recovers and becomes even heavier after approximately 5 hours [Wang and Feingold, 2009b]. As a consequence, liquid water path, cloud depth, and cloud albedo increase significantly in the polluted clouds.

Table 3.1. Cloud albedo responses[a]

	Cloud Regime			
	Collapsed	**Open**	**Low-Closed**	**High-Closed**
	105 cases	90 cases	78 cases	81 cases
Frequency of occurrence	15%	11%	All Closed cells: 45%	
$\Delta A/[A(1-A)]$	0.58 (0.42)	0.45 (0.55)	0.13 (0.17)	−0.03 (0.27)
Dewpoint Depression (K)	11.6 (4.6)	13.4 (6.5)	12.7 (6.0)	21.5 (6.2)
Rain Rate (mm/day)	0.29 (1.2)	1.49 (2.4)	0.00 (0.00)	0.60 (1.5)
$\Delta R/R$	0.23	0.68	0	−0.81
Cloud Height (m)	452 (152)	887 (298)	506 (113)	1188 (138)
$\Delta H/H$	0.13	0.08	0	-0.003
Width of ship track (km)	13	14	8	10
Length of ship track (km)	439 (225)	376 (172)	343 (149)	270 (152)
Effective Radius (μm)	17.9 (2.6)	19.4 (3.1)	11.8 (2.6)	14.0 (2.5)
$\Delta Re/Re$	−0.27	−0.23	−0.17	−0.19
Optical Depth	7.8 (2.8)	8.5 (2.9)	14.7 (5.5)	12.7 (5.4)
$\Delta\tau/\tau$	0.72	0.53	0.12	−0.03
Liquid Water Path	92 (33)	111 (42)	118 (54)	121 (58)
$\Delta LWP/LWP$	0.29	0.19	−0.06	−0.23

[a]Listed are the means and standard deviations (given in parenthesis) of the cloud albedo response, i.e. $\Delta A/[A(1-A)]$, dewpoint depression (ECMWF re-analysis data), rain rate and fractional change in rain rate (CloudSat), length and width of the ship track, effective radius and fractional change in effective radius ($\Delta Re/Re$), optical depth and its fractional change ($\Delta\tau/\tau$), and liquid water path ($\Delta LWP/LWP$) from the unpolluted segments from the population of ship tracks. Fractional changes are between the polluted and unpolluted clouds (i.e. [ship – cons]/cons). The number of cases used in the averages is provided for each cloud regime. Relative frequencies of ship tracks occurring in each cloud regime are also provided. The low- and high-cloud composites are separated by the median value of the average cloud top height distribution of closed cells.
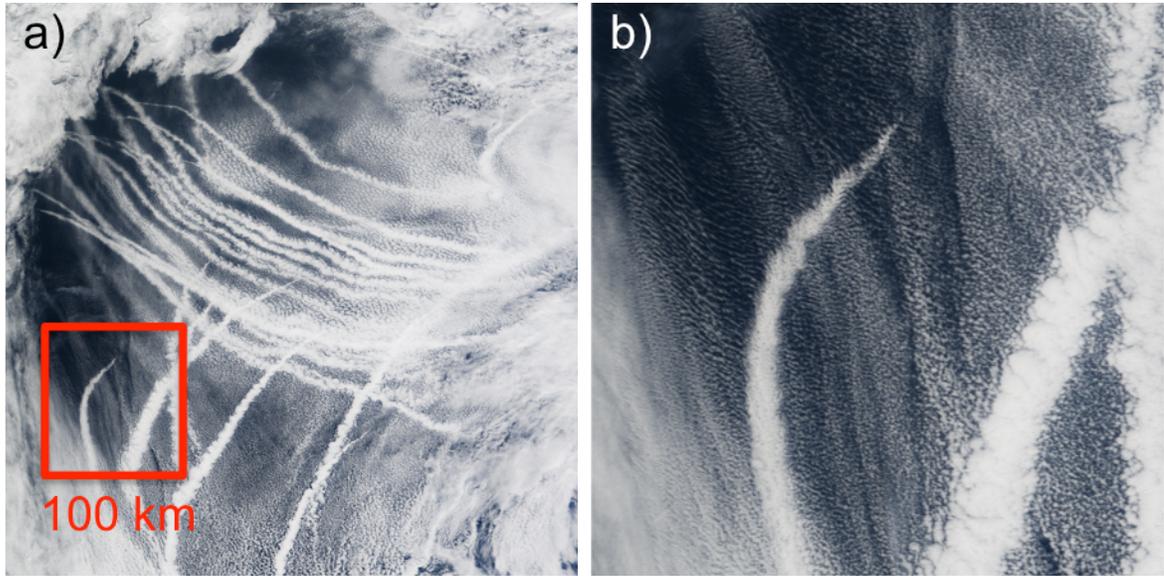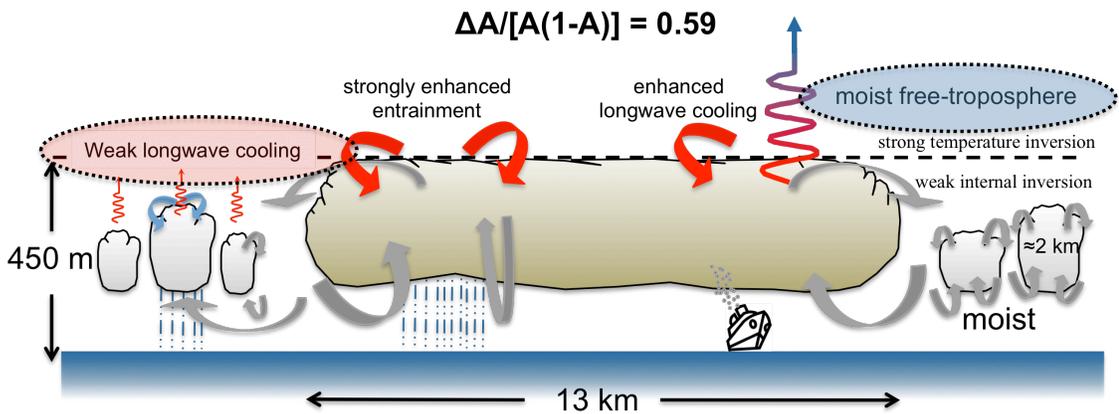
Figure 3.5. (a) True color satellite image of a collapsed marine boundary layer identified south of Alaska on March 4th, 2009 at 2125 UTC. (b) A 100 km^2 portion of the image is displayed over a ship track in the Southwestern part of the image. True color images were constructed by Robert Simmon and Jesse Allen and downloaded from http://earthobservatory.nasa.gov. (c) Conceptual diagram showing changes to the structure of the collapsed boundary layer by the effluents from ships. Gray arrows indicate the primary movement of the large scale turbulenece, red arrows indicate small scale mixing by entrainment. Wavy and dashed dotted lines represent cloud top radiative cooling and drizzle, respectively. The average value of the cloud albedo response, $\Delta A/[A(1-A)]$, for the ensemble of ship tracks detected in collapsed marine boundary layers is also provided.

a) Visible

b) Near IR
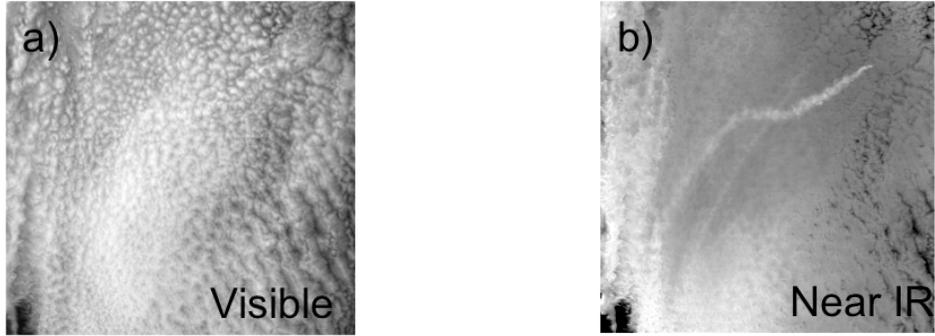
c)

Shallow Closed Cellular Clouds

ΔA/[A(1-A)] = 0.13

entrainment

dry

temperature inversion

500 m

well-mixed moist layer

8 km

d)

Deep Closed Cellular Clouds

ΔA/[A(1-A)] = -0.03

entrainment

extremely dry

temperature inversion

mixed cloud layer

1200 m

subcloud transitional layer

evaporative cooling

mixed surface layer

10 km
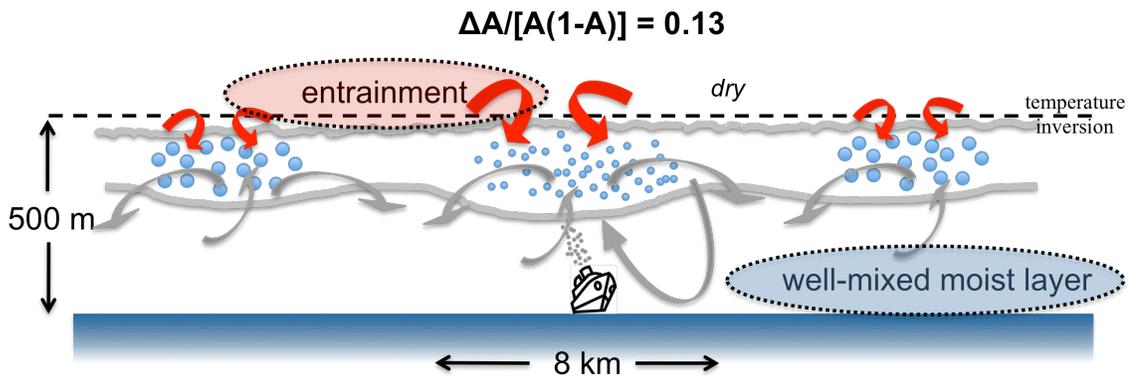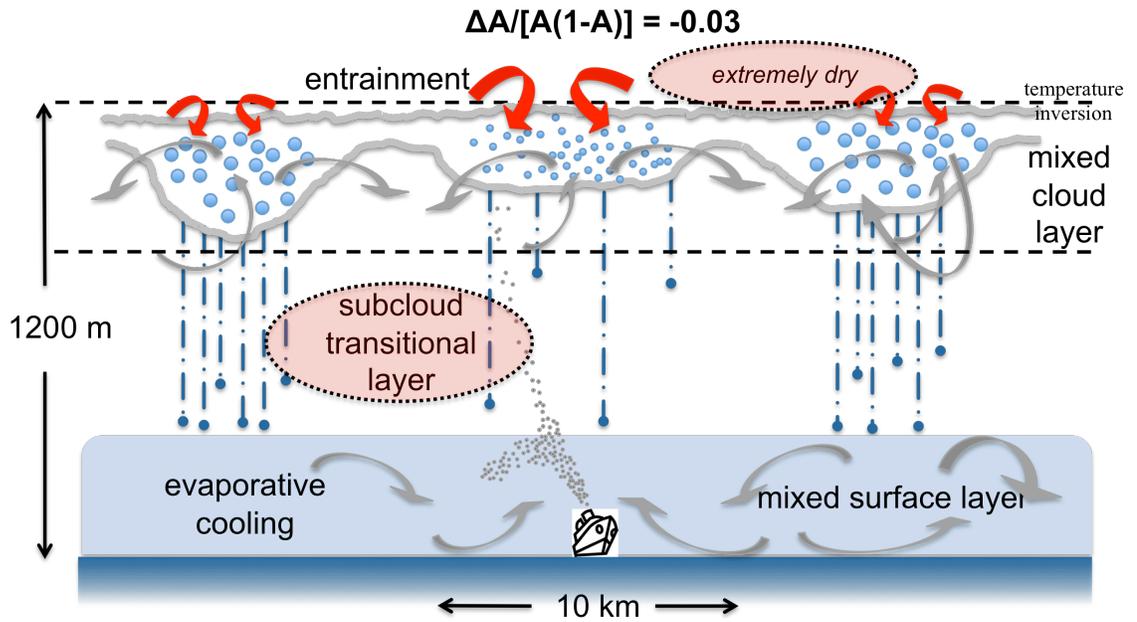
Figure 3.6. Same as Figure 3.5 except of a closed cellular cloud system off the coast of South America on November 18, 2008 at 1855 UTC.
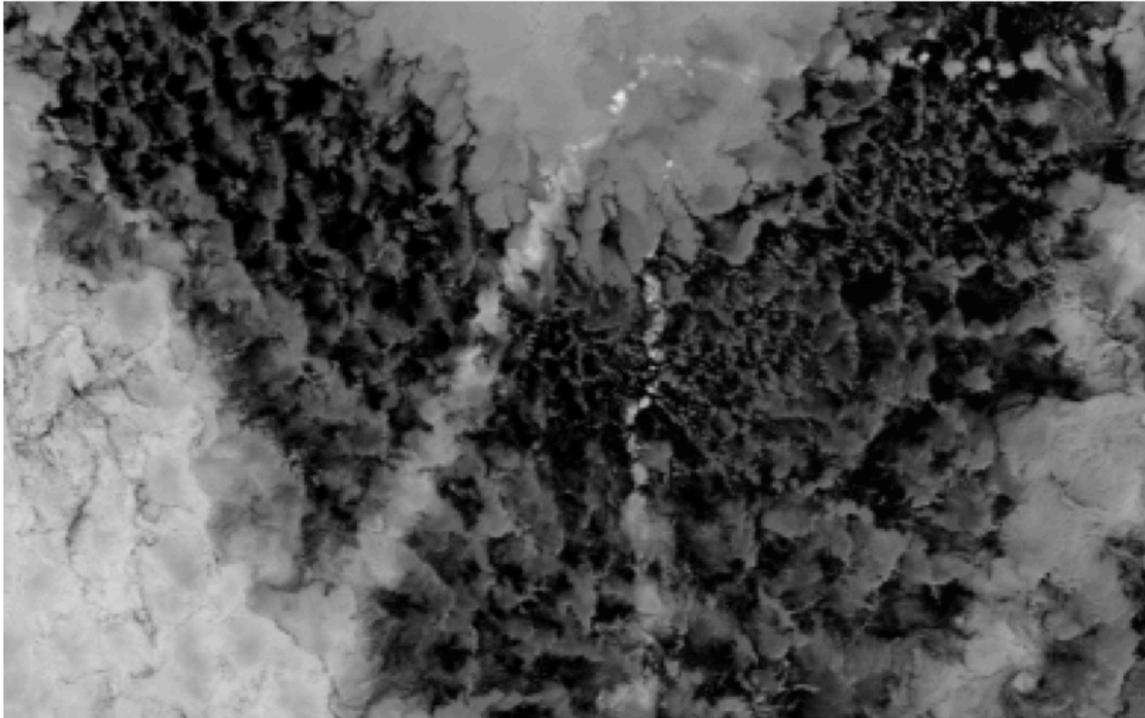
Open Cellular Clouds

ΔA/[A(1-A)] = 0.45
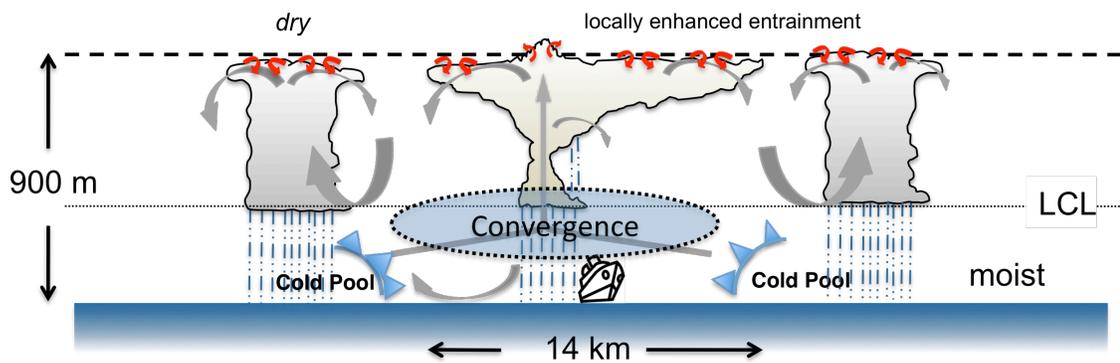
Figure 3.7. Same as Figure 3.5 except for an open cell regime showing a (a) near infrared image of ship tracks in a pocket of open cells on September 11th, 2007 at 2245 UTC.

3.3. Regional responses

The location and sign of the cloud albedo response for each ship track is plotted in Figure 3.8 (top). Cloud brightening by aerosol plumes was a common occurrence across the northernmost extent of the Pacific Ocean and along the West Coast of the United States. Throughout these regions, more than 85% of the polluted clouds were on average, more reflective then the surrounding unpolluted clouds. For regions in the Southern Hemisphere, a dimming influence on the clouds occurred nearly as often as a brightening one. In the annual average, free tropospheric humidity, assessed at 700 hpa, was significantly lower across the selected regions in the Southern Hemisphere compared to that across the Northern Pacific and off the West Coast of America. Regional influences on the cloud albedo response corroborate with the previous results, which demonstrate that as the free-tropospheric moisture decreases, negative adjustments to the aerosol indirect forcing become larger and are more likely to occur. Thus, regions of efficient low-cloud brightening may be constrained to regions in the midlatitudes where free-tropospheric moisture is frequently prevalent.
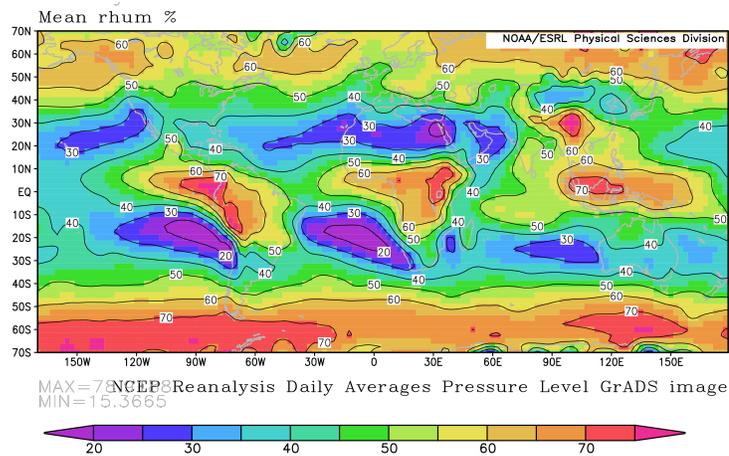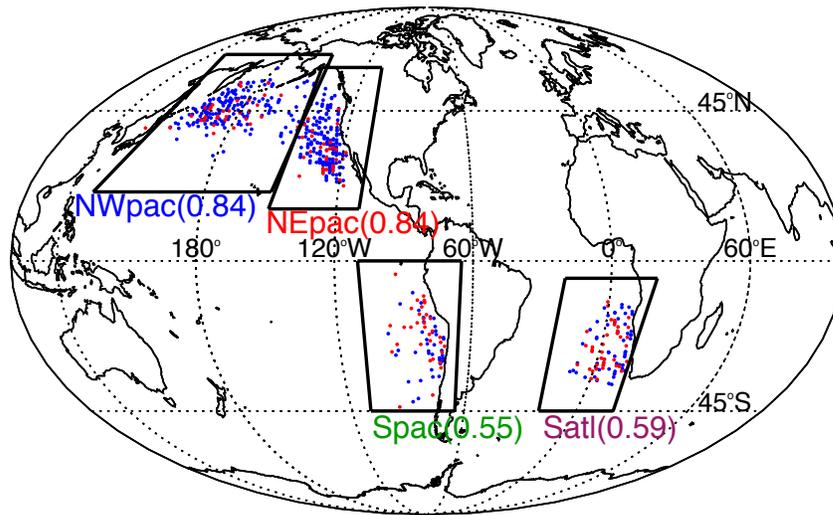
Figure 3.8. (top) Locations of ship tracks where plume-cloud brightening (blue) and, dimming (red) occurred. Names of the regions are abreviated and the fraction of ship tracks occuring in the region that are brighter than the surrounding clouds are shown in parenthesis. (bottom) Mean relative humidity at the 700 hpa level obtained from NCEP re-analysis data product, plot was obtained from the plotting routine that is available on the NCEP/NCAR website (www.esrl.noaa.gov); the data is described in Kalnay et al., [1996].

CHAPTER 4

DISCUSSION AND CONCLUSION

The effect of particle pollution on the direction of the cloud albedo response was

examined using over 500 ship tracks. Cloud brightening occurred in roughly 75% of ship

tracks where the extent of the change was mostly related to the height of the cloud layer,

free-tropospheric humidity, and the optical properties of the clouds. The results suggest

that changes in cloud top entrainment and boundary layer coupling influence the sign and

strength of the aerosol indirect effect. Unfortunately, measurements of entrainment and

degree of cloud coupling are not attainable using satellite technology (unless long-term

averaging methods are used) and can only be examined using in situ measurements or

through the use of models. E-PEACE provided a unique opportunity to investigate the

role of entrainment on the radiative properties of ship track clouds. Here, it was

confirmed that a sufficiently dry free-troposphere generally led to cloud dimming. The

intensity of the entrainment/detrainment rates in stratocumulus was commonly related to

the mesoscale structure of the clouds, thus making this kind of classification useful for

studying aerosol-cloud interactions. Concentration of CCN, precipitation rate, and large-

scale dynamical forcing (sea surface temperature and stability) play a large part in the

formation of the various mesoscale circulation patterns observed in stratocumulus.

Visually categorizing the cloud pattern in which ship tracks are embedded serves as a

useful indicator for interpreting the state of the atmosphere, providing another tool to

assess and analyze the aerosol-cloud interactions in marine stratocumulus. When the

clouds resembled open cells, or those in a collapsed boundary layer, the aerosol plume

128

significantly enhanced the albedo of the cloud layer. These cloud regimes constituted less than a third of the cases. Ship tracks were much more prevalent in a closed cellular regime where the cloud albedo response was often mixed. The results presented here demonstrate that increasing the concentration of aerosol does not always lead to cloud brightening and, the response is likely muted to some degree in closed cells. It is thus, essential to characterize the aerosol-cloud albedo response in marine stratocumulus clouds in order to pin down the cooling potential of aerosol effects in the climate system. This work is extended to the global scale in Part V of this dissertation to examine ship plume affects on the Earth's radiation budget.

REFERENCES

Ackerman, A. S., O. B. Toon, and P. V. Hobbs (1993), Dissipation of marine stratiform clouds and collapse of the marine boundary layer due to the depletion of cloud condensation nuclei by clouds, Science, 262, 226–229.

Ackerman, A. S., M. P. Kirkpatrick, D. E. Stevens, and O. B. Toon (2004), The impact of humidity above stratiform clouds on indirect aerosol climate forcing, Nature, 432, 1014–1017, doi:10.1038/nature03174.

Albrecht, B. A. (1989), Aerosols, cloud microphysics, and fractional cloudiness, Science, 245, 1227–1230.

Bretherton C. S., J. Uchida, and P. N. Blossey (2010) Slow manifolds and multiple equilibria in stratocumulus capped boundary layers, J. Adv. Model. Earth Syst., Vol. 2, Art. #14, 20 pp.

Chen, C., and W. R. Cotton (1987), The physics of the marine stratocumulus-capped mixed layer, J. Atmos. Sci., 44(20), 2951–2977.

Christensen, M. W. and G. L. Stephens (2011), Microphysical and macrophysical responses of marine stratocumulus polluted by underlying ships: Evidence of cloud deepening, J. Geophys Res., 116, D03201, doi:10.1029/2010JD014638.

Christensen, M. W. and G. L. Stephens (2012), Microphysical and macrophysical responses of marine stratocumulus polluted by underlying ships. Part II: Impacts of haze on precipitating clouds, J. Geophys Res., (in press)

Christensen, M. W., G. L. Stephens, G. Carrió, and W. R. Cotton, Radiative Impacts of Free-Tropospheric Clouds on the Properties of Marine Stratocumulus (in preparation for submission to JGR)

Coakley, J. A., Jr., R. L. Bernstein, and P. A. Durkee (1987), Effect of ship-stack effluents on cloud reflectivity, Science, 237, 1020–1022.

Durkee, P. A., and coauthors (2000), The impact of ship-produced aerosols on the microstructure and albedo of warm marine stratocumulus clouds: A test of MAST hypotheses 1i and 1ii, J. Atmos. Sci., 57, 2554 – 2569.

IPCC (2007), Climate Change 2007: The Physical Science Basis. Contribution of Working Group I to the Fourth Assessment Report of the Intergovernmental Panel on Climate Change. [Solomon, S., D. Qin, M. Manning, Z. Chen, M. Marquis, K.B. Averyt, M.Tignor and H.L. Miller (eds.)], Cambridge University Press, Cambridge, United Kingdom and New York, NY, USA.

Kalnay E. and coauthors (1996), The NCEP/NCAR 40-year reanalysis project, Bull. Amer. Meteor. Soc., 77, 437—470.

Liu, Q., Y. L. Kogan, and D. K. Lilly (2000), Modeling of ship effluent transport and its sensitivity to boundary layer structure, J. Atmos. Sci., 57, 2779–2791.

Lebsock, M. D., G. L. Stephens, and C. Kummerow (2008), Multisensor satellite observations of aerosol effects on warm clouds, J. Geophys. Res., 113, D15205, doi:10.1029/2008JD009876.

Lewellen, D. and W. Lewellen, 2002: Entrainment and decoupling relations for cloudy boundary layers. J. Atmos. Sci., 59, 2966–2986.

Martin, G. M., D. W. Johnson, and A. Spice (1994), The measurement and parameterization of effective radius of droplets in warm stratocumulus clouds, J. Atmos. Sci., 51, 1823–1842.

Paluch, I. R., and D. H. Lenschow (1991), Stratiform cloud formation in the marine boundary layer, J. Atmos. Sci., 48, 2141–2158.

Platnick, S., and S. Twomey (1994), Determining the susceptibility of cloud albedo to changes in droplet concentration with the advanced very high resolution radiometer, J. Appl. Meteor, 33, 334–347

Stephens, G. L. (2005), Cloud feedbacks in the climate system: A critical review, J. Clim.18, 237–273, doi:10.1175/JCLI-3243.1.

Stephens, G. L., P. M. Gabriel, and P. T. Partain, 2001: Parameterization of atmospheric radiative transfer. Part I: Validity of simple models. J.Atmos. Sci., 58, 3391–3409.

Taylor, J. P., and A. S. Ackerman (1999), A case-study of pronounced perturbations to cloud properties and boundary-layer dynamics due to aerosol emissions, Q. J. Royal. Meteorol. Soc., 125, 2643–2661, doi: 10.1002/qj.49712555915.

Twomey, S. (1974), Pollution and the planetary albedo, Atmos. Environ., 8, 1251–1256.

Wang, H., G. Feingold, R. Wood, and J. Kazil (2009a), Modelling microphysical and meteorological controls on precipitation and cloud cellular structures in southeast pacific stratocumulus, J. Atmos. Chem. Phys., 10, 6347–6362, doi:10.5194/acp-10-6347-2010.

Wang, H., and G. Feingold (2009b), Modeling mesoscale cellular structures and drizzle in marine stratocumulus. part ii: The microphysics and dynamics of the boundary region between open and closed cells, J. Atmos. Sci., 66, 3257–3275, doi:10.1175/2009JAS3120.1.

Wood, R., 2006: The rate of loss of cloud droplets by coalescence in warm clouds. J. Geophys. Res., 111, D21 205.

Wood, R. (2007), Cancellation of aerosol indirect effects in marine stratocumulus through cloud thinning, J. Atmos. Sci., 64, 2657–2669.

Wood, R., and C. S. Bretherton (2004), Boundary layer depth, entrainment and decoupling in the cloud-capped subtropical and tropical marine boundary layer, J. Climate, 17, 3576–3588.

PART V: IMPACT OF SHIP EMISSIONS ON CLIMATE

CHAPTER 1

INTRODUCTION

The world fleet of merchant ships consists of about 85,000 oceangoing vessels [Llyod, 2002]. In many oceanic regions, emissions from ships containing sulfur and particulate matter outweigh those from natural biogenic sources. These emissions serve as a potential test laboratory for analyzing aerosol indirect effects on low-clouds. A small fraction (less than 1%) of these emissions go into changing cloud microphysics and forming ship tracks; the other, larger portion, modifies the radiative properties of the stratocumulus through latent processes that cannot be directly observed using satellite technology. Satellite assessments involving the emissions from ships that only account for ship tracks grossly underestimate the magnitude of the radiative forcing. Therefore, and not surprisingly, the global impact of ship tracks inferred from satellite observations [Schreier et al, 2007] is negligible (-0.5 mW m^{-2}) compared to that due to the buildup of greenhouse gases (2.63 W m^{-2}; [IPCC, 2007, Working Group 1, *Cambridge Univ. Press*]). The other, and presumably larger, component is difficult to detect because exhaust plumes from vessels can affect clouds for up to 2 days after they are emitted from the ships. The plume can thus become dispersed over a wide area (several hundred kilometers), thereby making it difficult to attribute cloud brightening from an individual ship plume. By comparing the optical properties of clouds near densely populated shipping routes in satellite imagery, Peters et al., [2011] concluded that the net effect (ship tracks + dispersed plume effects) from shipping was not large enough to be distinguishable from the natural dynamics controlling cloud presence and formation.

In stark contrast to satellite observational studies, previous modeling attempts to analyze the impact from shipping on the radiation budget have discovered that an alarming portion of the total anthropogenic aerosol indirect forcing (as large as 40%) stems from shipping (e.g., Capaldo et al., [1999]; Lauer et al., [2007]). This result is surprising for two reasons: first, because global shipping accounts for a small portion of sulfate production (about 10% in the global average) and, second, because the predicted cloud radiative forcing far exceeds that estimated from the satellite observational studies mentioned earlier. It is thus, imperative to understand this disparity between the observations and GCM's in order to pin down the magnitude of the aerosol indirect forcing due to shipping.

In this part of the dissertation, an attempt is made to provide an estimate of the aerosol indirect radiative forcing due to ship tracks and shipping emissions as a whole. The impact of ship emissions on climate was inferred by examining the radiative changes in cloud properties by the very large decreases in ship traffic that took place prior and after the world economic recession in 2008. In the second study, a new approach was developed to predict the area of clouds contaminated by shipping lanes. An estimate of the global aerosol indirect radiative forcing is calculated for ship tracks in closed and open cellular cloud regimes.

CHAPTER 2

EXAMINATION OF POSSIBLE EFFECTS OF THE RECENT GLOBAL ECONOMIC RECESSION ON CLIMATE

2.1. Introduction

On September 11th, 2001, the Federal Aviation Administration grounded all flying aircraft over the continental United States. For a period of three days, the skies above were clear of airplanes and contrails. Travis et al., [2002] argued that the lack of contrails enhanced the diurnal temperature range by approximately 1°C over this period. During the day contrails exert a cooling effect through dimming the sunlight reaching the surface. At night, they act like "blankets" that provide warming by absorbing and re-emitting long wave radiation back to the surface. Aviation accounts for a mere 5% of the total anthropogenic fossil fuel consumption and, as demonstrated by Travis et al., [2002], has the ability to affect climate. Other forms of transportation, such as shipping, also impact the climate by cooling the surface through brightening and/or increasing the amount of low-clouds through the increase of sulfate particles in the boundary layer. Shipping accounts for roughly 60% of the total SO_2 production over most of the Northern Hemisphere oceans [Capaldo et al., 1999]. While the complete shutdown of shipping has never occurred, decreases resulting from the recent global recession may provide a way to investigate the extent to which emissions from ships influence the properties of low-clouds, and thus, climate.

On December 1st, 2008, the National Bureau of Economic Research declared that the United States was in the worst recession since the great depression. Many factors

136

contributed to the country's economic downturn, the consequences of which include crises in the housing, banking, and trading spheres. During 2008, the United States, among many other nations, experienced rampant inflation, rising gas prices (reaching $150 per barrel), record breaking unemployment rates, diminished home values, and record breaking foreclosures and personal bankruptcies. The gross domestic product (GDP) fell by 5%, and the U.S. trade deficit increased by 30 billion dollars (a 50% increase).

Figure 2.1 shows the trade balance during the last two decades. Evidently, the recession that took place between 2008 and mid-2009 coincided with significant reductions in both imports and exports to and from the United States. As examined in the next section, this led to fewer ships making trips to and from the United States of America. The world fleet of merchant ships transport up to 80% of the trade between nations. Because their emissions have the ability to alter the microphysical properties of the clouds they come into contact with, a large reduction was assumed to have an effect on the radiative properties of marine boundary layer clouds between the years of 2007 and 2009. Since a majority of the ship tracks analyzed in Part IV showed that about 75% of the cases were brighter than the surrounding clouds, the net effect of the emissions was therefore hypothesized to cool the globe through the increased reflected solar radiation to space. On the local cloud scale, ship tracks demonstrate that the radiative effect can be quite large compared to the global anthropogenic aerosol indirect forcing, where radiative forcing is typically on the order of several tens of watts per square meter. Because a small fraction of these emissions actually go into forming ship tracks (less than 1%), the analysis used here focuses on the differences in the average cloud properties of all

boundary layer clouds between 2007 (prior to the recession) and 2009 (after the recession) in order to infer the net radiative effect due to shipping. Changes in aerosol concentrations from non-shipping sources were not accounted for between these years and, it is recognized that this may serve as a potentially large source of error on the radiative properties of the clouds.
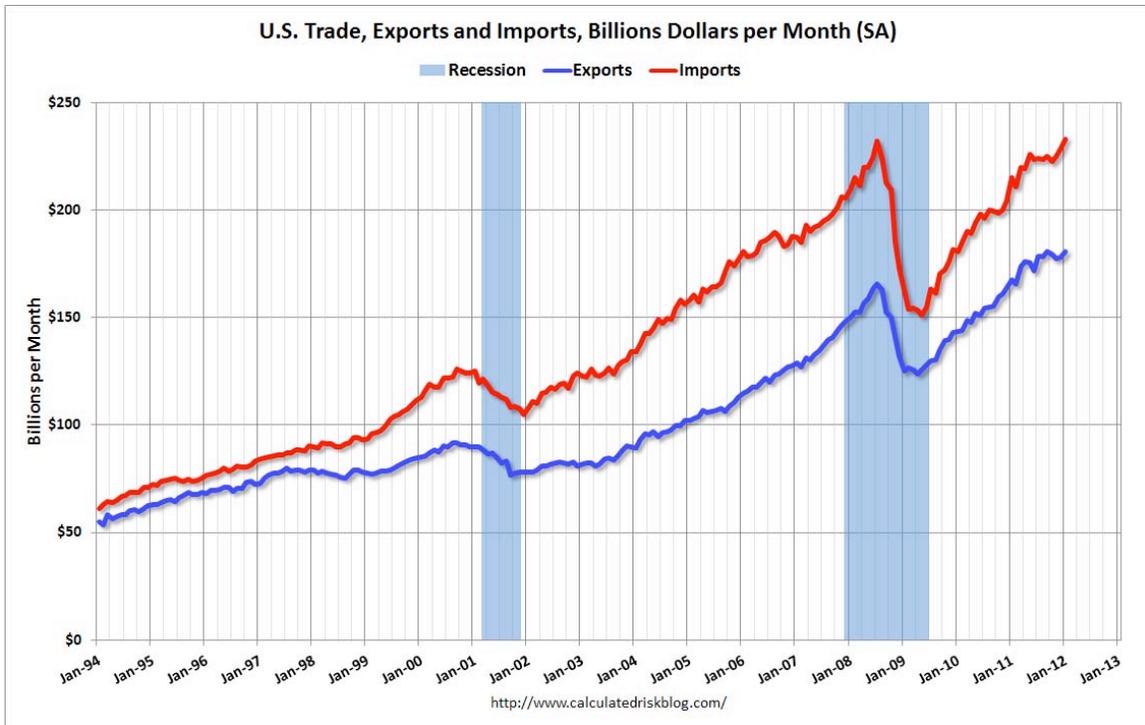
Figure 2.1. Monthly U.S. exports and imports in dollars from January 1994 to January 2012. Figure was obtained from the Calculated RISK Finance and Economics blog website (http://www.calculatedriskblog.com/2012/03/trade-deficit-increased-in-january-to.html).

2.2. Method

The locations of merchant ships were obtained from the Automated Mutual-Assistance Vessel Rescue System (AMVER). Cloud optical properties, such as droplet effective radius and cloud optical depth was obtained from the CloudSat collocated data products. Differences in several variables were examined between the years of 2009 at the peak of the recession and 2007 when trade between nations was healthy. Sponsored by the United States Coast Guard, AMVER is a voluntary global ship reporting system that was established in 1958. Its primary purpose is used for aiding in search and distress calls out over the ocean; it accounts for roughly 1/3 of the world fleet of merchant ships.

139

Because ship emissions remain confined to the planetary boundary layer, clouds were screened to include only those that were detected below 3 km using the CloudSat 2B-Geoprof-Lidar product. A value of 3 km was chosen because the depth of the boundary layer rarely exceeds this level over the global oceans. Cloud optical properties, such as droplet size and optical depth, were obtained from the MODIS cloud product that is collocated to the CloudSat observations (MODIS-AUX). Because MODIS estimates column-averages of the cloud properties, profiles were screened to include only single layer low-level clouds. Cloud albedo was estimated using the Eddington approximation for a non-absorbing media ($\alpha = (1 - g)\tau / (2 + (1 - g)\tau)$), where the asymmetry parameter, g, was taken to be 0.85 as typically observed in warm water clouds. Outgoing shortwave radiative fluxes at the top of the atmosphere were characterized using the Clouds and Earth's Radiant Energy System (CERES) instrument and obtained from the CERES-MODIS-CALIPSO-CloudSat (CCCM) dataset.

2.3. Results

Figure 2.2 shows the distribution of the world fleet of ships for 2007 (top) and the difference between 2009 and 2007 (bottom). Despite the global recession, the number of ships increased by 13% throughout this time period. Increases primarily occurred along the African and Asian coasts. Clearly, large reductions occurred across the northern Pacific and Atlantic oceanic basins where shipping decreased by more than 10%. The cause of which was linked to the global recession [Los Angeles Times, 30 December 2010]. In fact, AMVER registered 6,500 fewer ships making several-day voyages across the Northern Hemisphere oceans in 2009, which resulted in a reduction of approximately

200 KT of sulfur emissions. This was estimated by assuming that on average, ships burning low-grade marine fuel oil use 1 kg of fuel per second and roughly 12% of the emissions go into producing particles and sulfur gas that can serve as cloud condensation nuclei [Hobbs et al., 2000]. Because AMVER only accounts for about 1/3 of the world fleet of ships, the decrease was probably closer to 20,000 ships across the Northern Hemisphere oceanic basins. In contrast, the south Atlantic exhibited a significant increase in shipping (70%) during this time period. The increase may have occurred artificially, that is, more people may have registered their ships with AMVER from 2007 to 2009. Another possibility is that, despite the global economic recession, many countries in East Asia retained a rapidly growing economy [The Guardian, 23 March 2012]. The increase in shipping across the south Atlantic thus, may have occurred because Cape Town (in South Africa) is a central hub for transportation to East Asia. As a result, an additional increase in about 4 KT of particulate matter (that could potentially serve as CCN) was injected into this region between 2007 and 2009 by the increased shipping.

Figure 2.3 shows the distribution of mean cloud effective radius for 2007 (top) and the difference between 2009 and 2007 (bottom). Evidently, cloud droplets were particularly small near the continental land-masses where cloud condensation nuclei (CCN) is commonly abundant in the air mass containing continental aerosols and those generated by megacities along the coasts. Farther from the coast, CCN concentrations decreased presumably due to wet and dry deposition processes where consequently clouds exhibited larger and less numerous cloud droplets. By examining the differences in the droplet radii of low-level clouds between 2007 and 2009, it was not clear that the reductions in shipping had much of an affect on the mean state of the clouds. This is

demonstrated by the apparent lack of a coherent spatial signal in the difference. However, through close examination, effective radius was smaller across the north Atlantic ocean in the region coinciding with high volumes of shipping for three years of CloudSat observations (2007, 2008, and 2009; plot not shown) but, differences in the size of the droplets between 2007 and 2009 were minimal in this region despite the large reduction in shipping.

Averages of many of the microphysical and macrophysical variables are provided in Table 2.1. As expected, in regions where shipping decreased (across the Northern Hemisphere), cloud effective radius increased on average. However, the differences were noisy and, were often larger than the standard error of the difference of means. With an exception, the low-level clouds off the coast of Africa exhibited decreases in effective radius, increased cloud optical thickness, increased cloudiness, and increased ship traffic between 2007 and 2009. Due to the optically thicker clouds and higher cloud fractions in 2009, the regional albedo increased on average, and increased the outgoing shortwave radiation at the top of the atmosphere by approximately -1.8 W m^{-2} compared to 2007. Because the sea surface temperature and atmospheric stability remained relatively constant between both years, the additional ships may have had a significant impact on the cloud properties throughout this region. Here, the differences were statistically significant at the 95th percentile using a two-tailed T-test.

In the remaining regions, fewer ships were correlated with larger cloud droplets and lower cloud optical thicknesses, however the changes were not statistically significant. Average cloud amounts were also higher in 2009. The increased cloudiness resulted in a higher amount of outgoing shortwave radiation. This contradiction negates

the assumption that less ship traffic would have a warming influence. The effect may have been masked by the increased cloudiness caused by interannual and seasonal variability in meteorology during this time period. This result is in qualitative agreement with Peters et al., [2011] in which the radiative properties of low-level clouds were unaffected by dense shipping lanes.
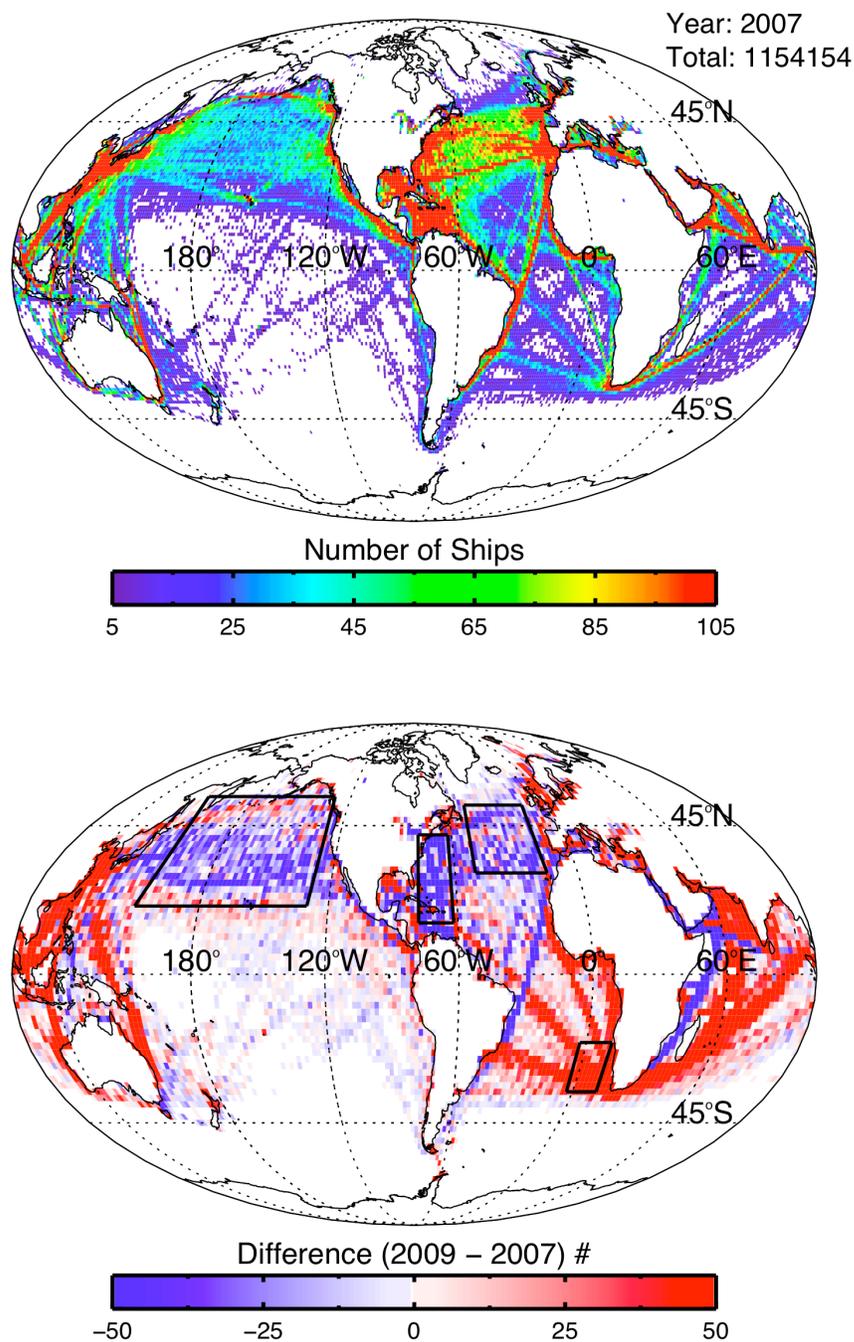
Figure 2.2. Annual average distribution of the number of ships obtained from AMVER for (top) the year 2007 and difference (bottom) between 2007 and 2009 annual averages. Data was binned into $1° \times 1°$ degree regions in the top panel and into $2.5° \times 2.5°$ degree regions in the bottom panel.
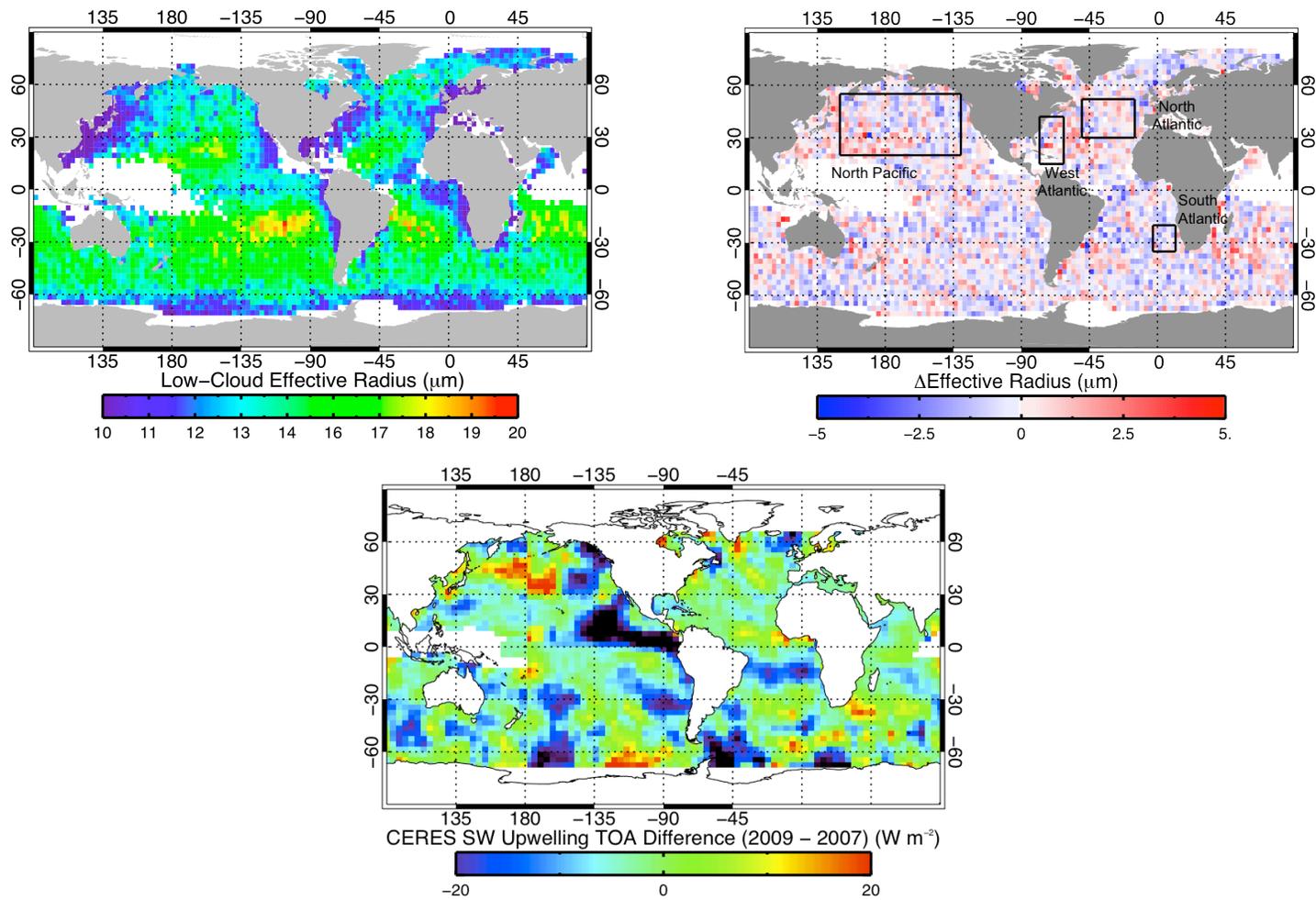
Figure 2.3. Annually averaged global distribution of (top left) 3.7-μm derived cloud effective radius for cloud layers with cloud top altitudes less than 3 km as determined from the 2B-Geoprof-lidar product. Top right panel shows the differences in average effective radius between years, 2007 and 2009. Bottom panel shows the difference in the top of atmosphere shortwave radiative flux between years, 2007 and 2009 obtained from the CERES instrument. Global plots were constructed by binning daytime observations into 1° × 3° (latitude × longitude).

145

Table 2.1. Regional analysis of low-cloud properties between 2007 and 2009[a]

Δ(2009-2007)	South Atlantic	Northeast Atlantic	West Atlantic	North Pacific
ΔShips (%)	70	−13	−20	−10
ΔR_e (μm)	−0.6 (0.24)	0.2 (0.13)	0.6 (0.37)	0.01 (0.07)
ΔOptical Depth	1.4 (0.8)	−0.5 (0.6)	−2.6 (1.8)	−0.1 (0.1)
ΔLow-Cloud Amount (%)	0.45 (1.7)	3.3 (0.8)	1.0 (0.7)	1.25 (0.4)
Forcing (W m^{-2})	−1.8 (6.0)	−2.2 (7.5)	−1.7 (7.9)	−2.6 (8.0)
ΔSST	0.13 (0.06)	−0.37 (0.07)	0.07 (0.07)	0.13 (0.04)

[a]Regionally average differences between years, 2007 and 2009, of the fractional change in the number of ships (AMVER database), droplet effective radius (MODIS), cloud optical depth (MODIS), cloud amount (2B-Geoprof-Lidar), cloud radiative forcing (CERES), and sea surface temperature (ECMWF-AUX re-analysis).

2.4. *Impact from the sea surface temperature response*

To understand why the aerosol indirect forcing may have been masked in most regions, Figure 2.4 reveals that the year 2007, coincided with a modest La Niña, as indicated by the warm anomaly in sea surface temperatures across the equatorial Pacific. Klein and Hartman, [1993] demonstrated that the amount of marine stratocumulus, is highly correlated to the monthly averaged sea surface temperature, with a correlation coefficient equal to -0.76. As sea surface temperatures cool, the boundary layer typically shallows, becomes more statically stable, and entrains less dry air thereby trapping moisture near the surface and increasing the likelihood of forming clouds. Figure 2.5 shows the abundance of single layer low-level clouds (with tops less than 3 km) as identified from the joint CloudSat and CALIPSO product (2B-Geoprof-lidar). The anomaly in the center of the North Atlantic was two degrees colder in 2009 compared to 2007. A cold anomaly may have been responsible for the increased amount of low-level cloudiness. Warm anomalies (in 2009 compared to 2007) in the Eastern Pacific coincided with reduced cloudiness on average. Because the clouds were highly reflective, the albedo throughout these regions was mostly determined by the cloud amount and, changes forced by meteorology and SST probably outweighed those due to shipping. For example, a decrease of 1°C (SST) increases cloudiness and regional cloud albedo by approximately 5% per K as found in Klein and Hartman, [1993] over for subtropical stratocumulus regions. Therefore, a 1 K change in SST would entirely mask the changes estimated due to shipping (i.e., the relative increase in the forcing would be equal to about -17 W m^{-2}). Because the meteorology remained relatively constant between 2007 and 2009 in the South Atlantic, it was thus possible that the increased regional albedo

was due to increased ship vessel traffic. Although, further investigation using a regional climate model is likely needed to determine if shipping was the sole cause of the increased cloudiness and albedo off the shore of South Africa during 2009.

2.5. Discussion

In order to isolate the effect of shipping on the radiative properties of low-level clouds, further investigation is clearly needed. Because changes in SST and other large-scale meteorological variables can partially explain the cloud albedo response, a closer examination of the cloud properties is needed to attribute cause and effect. Several methodologies, though labor intensive, could be used to accomplish this end. One way could be to implement a global circulation model capable of resolving the dispersion of ship plumes and their interaction with the clouds explicitly. Or, by choosing specific shipping lanes to monitor the evolution of the clouds using a geostationary satellite as they propagate across dense lanes of ship traffic. Such a research project will be possible with the upcoming launch of the Geostationary Operational Environmental Satellite – R Series (GOES-R) in 2015.

An analysis of the indirect radiative effect from shipping could be assessed using a state-of-the-art 3D transport model capable of resolving the dispersion of ship plumes and its interaction with the clouds explicitly. Such a model would provide a quantitative estimate of the aerosol indirect effect from shipping (ship tracks and dispersed plume effects) under a variety of mesoscale cloud regimes in which the clouds react to aerosol along different pathways (Part IV). By incorporating a model that can simulate the

148

mesoscale structure of the clouds (e.g., Bretherton et al., [2004]), it is hypothesized, that cloud brightening on the global scale will not follow the simple Twomey relationship established in Part IV and, a small or even possible cancellation of the aerosol indirect effect will likely arise due to changes in meteorology or competing mesoscale cloud regimes that have opposing influences on cloud albedo. If the hypothesis is true, the indirect forcing estimated from shipping would more closely resemble the muted responses derived from observations of ship tracks in frequently occurring closed cellular clouds.
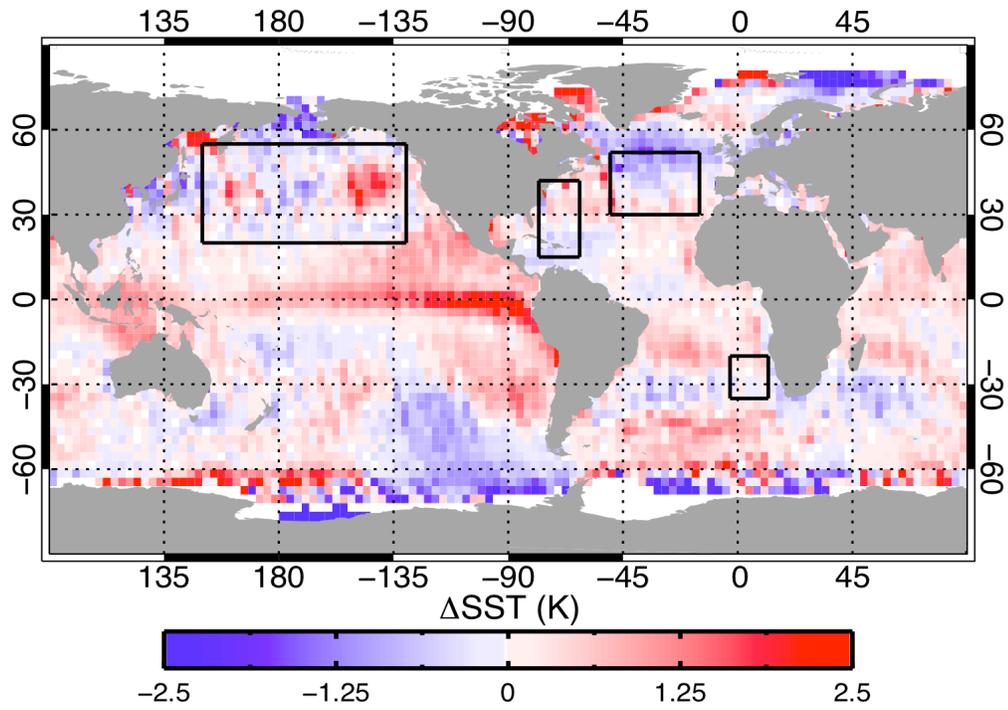
Figure. 2.4. Difference in mean sea surface temperature (SST) between years, 2009 and 2007 (Δ = 2009 − 2007) binned into 1° × 3° regions.
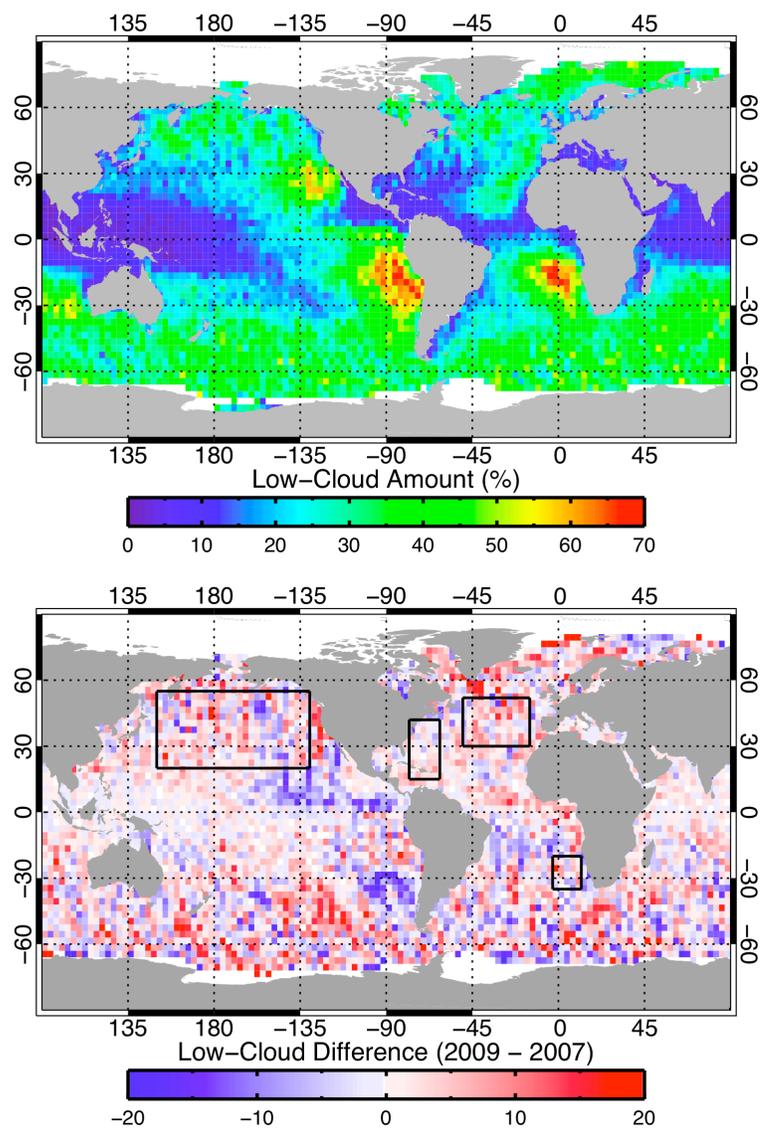
Figure 2.5. Single layer low-level cloud amount (less than 3 km) obtained from the joint CloudSat and CALIPSO data product (2B-Geoprof-lidar) annually averaged (top) over the year 2007 and (bottome) the difference (Δ = 2009 – 2007) between years, 2007 and 2009.

2.6. Conclusion

The recent global economic recession of 2008 resulted in the reduction of approximately 10% of the shipping across the Northern Hemisphere oceanic basins. This resulted in an approximate reduction of 200 KT of sulfur emissions across the region. On the average, regional cloud albedo was diminished, however the changes were not significant. Such a dramatic difference in shipping was expected to have a noticeable impact on the radiative properties of the clouds due to that predicted by the Twomey effect, however, the signal was probably partially masked due to the changes in sea surface temperature caused by the modest La Niña recorded in 2007. The response may have also been masked if higher frequencies of closed cells, deeper clouds, or drier free-tropospheric air occurred in 2009, thereby reversing the sign of the aerosol indirect forcing (Part IV results).

In the South Atlantic region, where shipping increased significantly and changes in SST were small, low-clouds were significantly brighter probably in response to more ships passing through the region in 2009. Here, the regional cloud radiative forcing was approximately -1.8 W m^{-2}, although further investigation is needed to rule out changes in aerosol concentration (other non-related shipping sources) that may have occurred throughout the time period. The results reported here demonstrate that shipping may have an impact the regional albedo of clouds, however further studies that utilize GCM simulations are likely needed to quantify this effect.

CHAPTER 3

GLOBAL PROJECTION OF SHIP TRACKS ONTO GLOBAL CLOUD

RADIATIVE FORCING

3.1. Algorithm implementation and analysis procedure

In order to evaluate the global cloud radiative forcing from ship tracks, a global database of their areal coverage is required. Building such a database by hand would be a relentless task and would likely take an individual their entire lifetime to complete. The use of automated ship track identification algorithms have achieved some success (e.g., see Schreier et al., [2007], and Campmany et al., [2009] for details on the algorithm), however, these schemes are typically fraught with detection errors that often produce a substantial percentage of falsely identified ship tracks. With detection errors commonly as large as 50%, the use of automated schemes casts considerable doubt on their reliability to accurately assess the aerosol indirect forcing from ship tracks.

The current study describes an alternative method to estimate the aerosol indirect forcing from shipping on a global scale that does not require either the painstaking task of logging ship tracks by hand or running time consuming automated schemes that are fraught with detection errors. Here, the fraction of a region covered by ship tracks is based on two key parameters: ship vessel density and the joint frequency of clouds in which their geometrical and optical properties reside within those of the ship tracks analyzed in Parts II – IV. By utilizing this approach, the global radiative forcing from ship tracks can be estimated and possibly illuminate aspects – such as the locations,

153

seasons, and cloud regimes – that may be climatically important in aerosol indirect effect studies.

Ship tracks most frequently occur when ocean going vessels burn low-grade diesel fuel producing particles in the accumulation size mode and, the plume remains intact upon impinging the base of the cloud layer. Dispersion and dilution rates of the plume remain small as long as the cloud base and lifting condensation level are low and coupled to a cool moist surface layer. In addition, ship tracks tend to go undetected if the pollution is high in the ambient air or the cloud droplets are small with large optical depths [Platnick et al., 2000]. Using satellite observations of cloud top height, sea surface temperature, lower troposphere stability, cloud effective radius, and cloud optical depth a ship track formation efficiency parameter (E) was developed to determine the likelihood of detecting a ship track if a ship is in the vicinity. The parameter predicts on an area over which ship plumes contaminate the properties of low-clouds, thereby enabling a rough estimate of the aerosol indirect radiative forcing from ship emissions.

The change in the top of atmosphere radiative forcing can be calculated from

$$\Delta F = \Delta F_{local}\left(A_{ship}/A_{region}\right), \qquad (1)$$

where ΔF is the change in the net shortwave flux at the top of the atmosphere caused by a local change in the radiative flux (ΔF_{local}) from polluted clouds that cover the region (A_{ship}/A_{region}). Equation (1) simply predicts the change in the top of atmospheric radiative flux by altering a fraction of the regional albedo (whether it is changes in the surface or cloud properties). Local changes in the radiative flux were calculated using

$$\Delta F_{local} = -\Delta\alpha F_{SW}^{\downarrow}, \qquad (2)$$

154

where $\Delta\alpha$ is the local change in cloud albedo caused by the ship plumes interaction with the radiative properties of the low-clouds and $F_{SW}^{\downarrow}$ is the top of atmosphere downwelling shortwave radiation. Because the A-Train crosses the equator at approximately 1:30 pm local time, $F_{SW}^{\downarrow}$ is approximately 70% smaller than the local noon value. In regions of closed and open cells, $\Delta\alpha$ takes on mean values of 0.02 and 0.19, respectively [Christensen and Stephens, 2011]. Realistically, $\Delta\alpha$ ranges from -0.3 to 0.3 in satellite observations of ship tracks where the value is highly correlated to the type of mesoscale convection (i.e. closed or open cellular), depth of the marine boundary layer, optical thickness and effective cloud droplet radius, and free-tropospheric humidity (Part IV). Because a positive $\Delta\alpha$ value was used here, cloud brightening always occurred and, this assumption negates negative feedbacks that can diminish the brightening influence from the plume. However, because 75% of the ship tracks studied in Part IV were brighter than the surrounding clouds, this assumption represents the typical response of aerosol-cloud brightening in ship tracks for these cloud regimes when averaged over many cases.

The fraction of clouds in the region polluted by underlying ships (A_{ship}) was calculated by dividing it by the area of the region (i.e., $A_{region} = r_{earth}^2 \int_{\Delta\phi} d\phi \int_{\Delta\theta} \sin\theta d\theta$, where r_{earth}^2 is the radius of the earth and equal to 6,378 km, ϕ is the longitude, and θ is the latitude). Polluted clouds were assumed to resemble the same spatial characteristics of ship tracks – that is having average widths and lengths of 7 and 296 km, respectively [Durkee et al., 2000]. Therefore, the effluents from ships typically contaminate a 2000 km^2 region (A_o) of clouds on average. However, not every ship produces a ship track. In fact, during many of the stratocumulus cloud campaigns, ship tracks were seldom found to occur downwind from ship plumes due to the persistent inadequate meteorological

155

conditions. Global assessments of ship tracks demonstrate that their occurrence is rare [Schreier et al., 2007], and on average, cover approximately 0.004% of the earth [Campmany et al., 2009]. To account for the scarcity, an efficiency parameter was introduced as a way to determine how effective the plume was in contaminating the clouds and producing ship tracks. The contaminated area was parameterized as

$$A_{ship} = N_s A_o E(H, R_e, \tau_c, LTS)\tau_s, \tag{3}$$

where N_s is the average number of ships identified in the region per day using the AMVER database, τ_s is the average lifetime of the ship tracks (7.3 hours estimated by Durkee et al.,[2000]), and E is the ship track formation efficiency parameter that is a function of cloud top height (H), effective radius (R_e), cloud optical depth (τ_c), and lower troposphere stability (defined in Part II) – variables in E that strongly modulate the appearance of ship tracks in satellite imagery [Coakley et al., 2000].

The probability of finding a ship track in a region containing an oceangoing vessel was determined from the joint probability of the observed ship track frequencies with the distributions of clouds in the region. The integrated area under the curve represented a measure of similarity (or correlation) between the two distributions. Figure 3.1 shows an example outlining the approach for estimating the ship track forming efficiency in a region off the West Coast of Chile during austral winter. First, frequency distributions from the ship track database and regional observations were normalized. Next, the area of the joint probability distribution was determined by integrating over the region where the two distributions overlap. If the distributions were identical then the area or probability of the frequency of the clouds having the same properties as those

identified in the ship track database would be equal to one. Roughly 50% of the probability distribution functions overlapped for each variable shown in Figure 1.

Since several variables control ship track formation, the probability distributions were assumed to be independent so that the ship track formation efficiency could be parameterized as

$$E = P(H) \times P(R_e) \times P(\tau) \times P(LTS),$$ (4)

where $P(H)$, $P(R_e)$, $P(\tau)$, and $P(LTS)$ are the probabilities of the above mentioned variables that reside within the distributions of the ship track database. Because ship tracks were never observed when sea surface temperatures were greater than 21°C, cases in which the clouds were overlying warmer sea surface temperatures were assigned a probability of zero. This approach serves as a simple way to determine the annual and seasonal radiative forcing of ship tracks on the global scale. To determine global radiative forcing of ship tracks by cloud regime, ship density was projected onto the distributions of closed and open cellular clouds. The following section describes a method to detect stratocumulus clouds as being closed and open cellular.
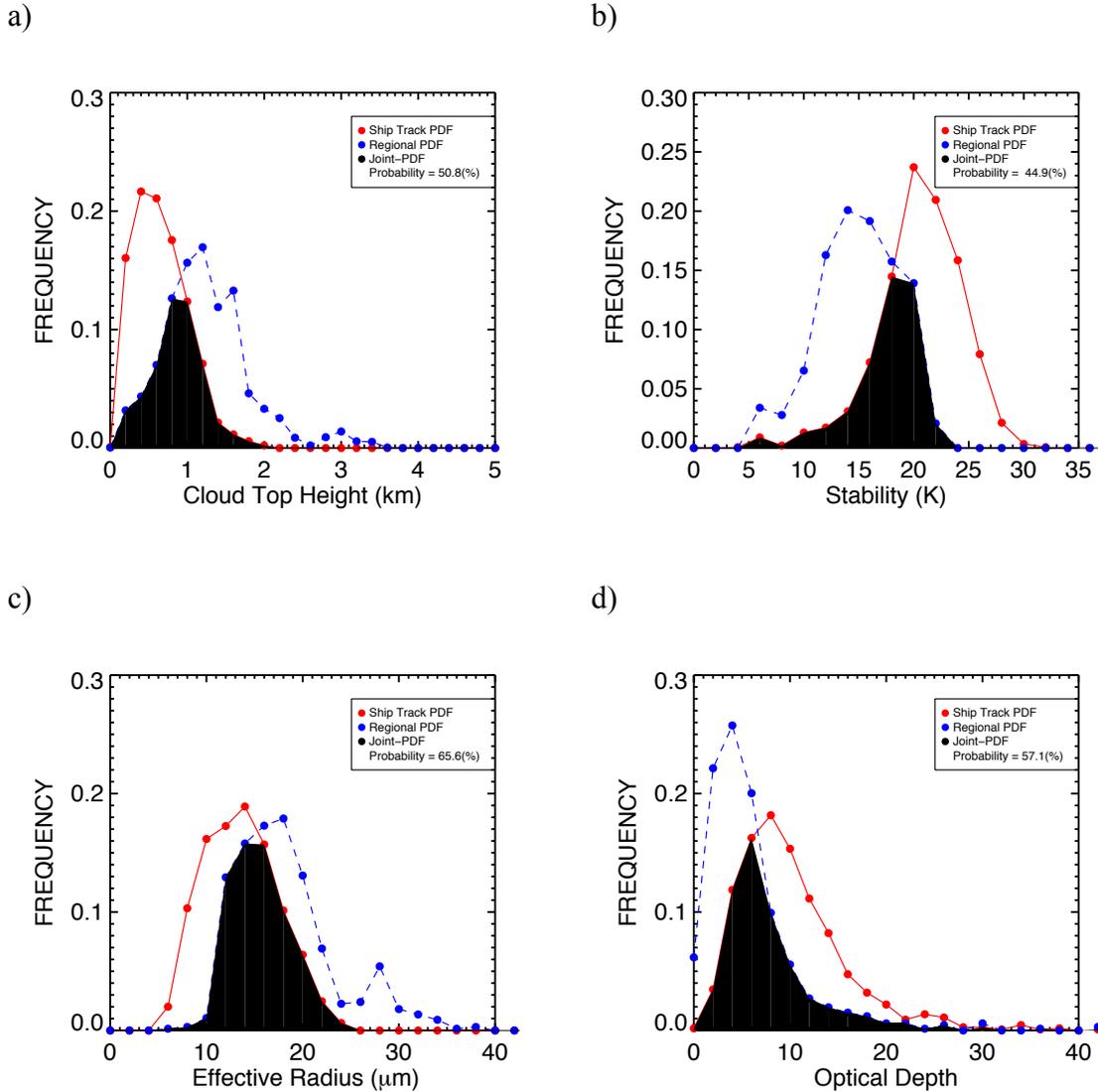
Figure. 3.1. Frequency distribution of the segment averages from the observed ship track database (solid red line) and those observed over a 1° × 3° region just off the coast of Chile during JJA (blue dashed line) as a function of (a) cloud top height, (b) lower troposphere stability, (c) cloud effective radius, and (d) cloud optical depth. Area calculated between curves represents the probability of observing similar cloud properties over the region with the ship track database. The combined probability from all four PDFs was approximately 10%.

3.2. Automated cloud classification algorithm

The procedure used to detect the type of mesoscale cloud convection (closed or open cellular clouds) was obtained from the global analysis of MODIS data using the methodology outlined in Wood and Hartman, [2006]. Robert Wood offered to share this algorithm and the global distributions of closed and open cells clouds for the research conducted here. The algorithm uses a power spectral analysis and neural network approach to characterize the size and type of mesoscale cellular clouds. Power spectrums were calculated using liquid water path in 1-km MODIS pixels for regions having an area of 256 km^2. The 2D power spectrums of the liquid water paths were used to estimate the width of cloud cells. To obtain the cellular cloud type, a neural network was trained by visually inspecting several hundred cases. This was performed in the stratocumulus-dominated regions off the west coasts of North and South America. Once trained, the algorithm selected the cellular cloud regime having the highest correlation to the skewness and kurtosis of the power spectrum distribution as constructed from the training. Four classification categories were used: closed, open, homogenous, and inhomogeneous cellular stratocumulus over the global oceans.

Figure 3.2 shows the annually averaged oceanic distributions of (a) closed, and (b) and open cellular clouds during 2008. Ship traffic is plotted over the top of the mesoscale cloud distributions in regions where the density is high (i.e., a minimum of 15 ships per day in a 0.5° × 0.5° region). In the global average, closed cell clouds were observed 2.5 times more frequently than open cells. Interestingly, their spatial distribution was quite similar – that is, closed cells occurred in roughly the same places as open cells but having higher abundances. There were some exceptions; the frequency of

159

open cells generally became higher farther from continents probably because open cells are associated with larger cloud droplets [Wood et al., 2008]. Closed cells were observed in high abundance in the midlatitudes and along the coastlines of continents.

Also shown in Figure 3.2 are the distributions of the annually averaged (c) ship track formation efficiency and (d) abundance of ship tracks in the closed cellular regime for the year 2008. Evidently, the ship track formation efficiency was high in regions where the cloud tops were relatively low with cold sea surface temperatures (see Figure 3.2 in Part III). Such regions typically occurred in the midlatitudes and in stratocumulus dominated regions. While the efficiencies were relatively high across the circumpolar Southern Hemisphere Oceans, ship traffic was very sparse so that the radiative forcing from ship tracks was negligible there. Conditions were also commonly ideal in the Southern Hemisphere stratocumulus regions, off the coasts of South America and South Africa, however few ship tracks were projected to occur because ship vessel traffic was relatively small in those locations. The fraction of the clouds polluted by the ships was calculated by using equation (3). Here, we estimate that ship tracks cover approximately 0.0025% of the Earth when observed in the closed cell regime and approximately 0.0007% when observed in open cells (the inhomogeneous regime exhibited similar values as the closed cell regime). Ship tracks were more commonly observed in closed cellular clouds, a result also found in Part III, but probably because the abundance of them was simply larger.

Because the calculation of E played a large role in the likelihood and abundance of ship tracks, E was artificially increased and decreased by 10% to estimate the uncertainty in the radiative forcing. Increasing/decreasing E by 10% altered the

160

abundance of ship tracks by factors of 3 and 4 in closed and open cell regimes, respectively. Knowledge of the uncertainty of E is unknown, but if it had an uncertainty of 10%, the radiative forcing would have a relative uncertainty of 300 to 400%. It is noteworthy that the ship track database of Part III may not be representative of ship tracks everywhere on the globe and, other variables such as low-level divergence, wind shear, sensible and latent heat fluxes, and atmospheric moisture probably influence ship track formation. The resultant ship track distributions produced here, have a remarkably similar spatial distribution as those detected in Part III and in other global assessments of ship tracks (e.g.; [Schreier et al., 2007];[Campmany et al., 2009]).
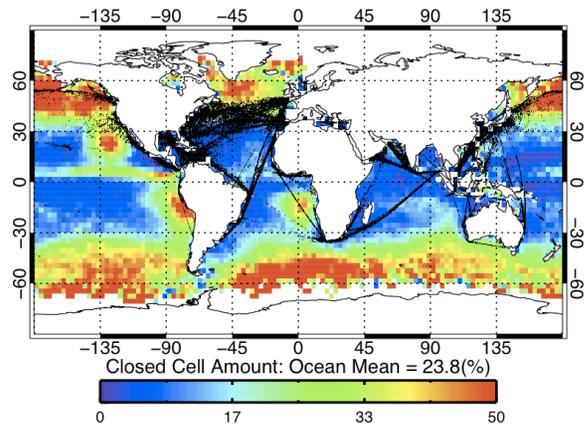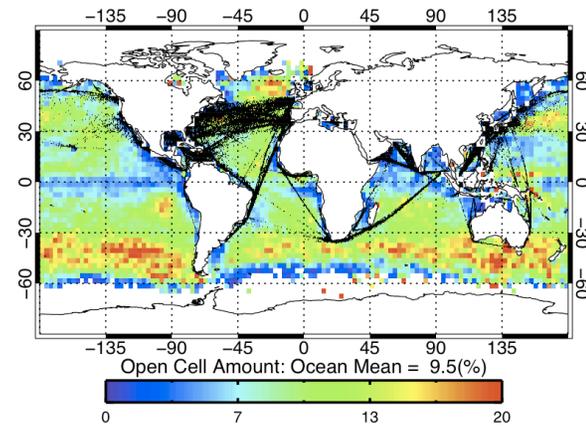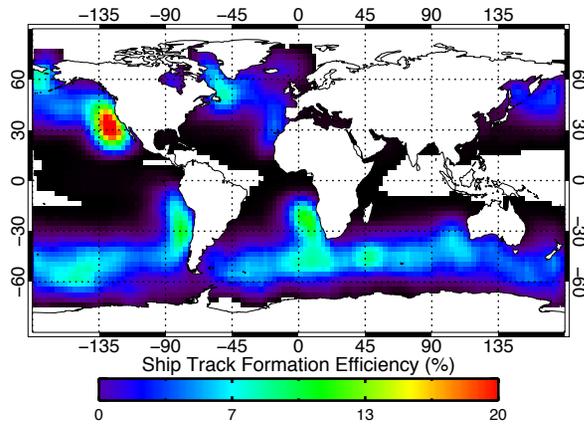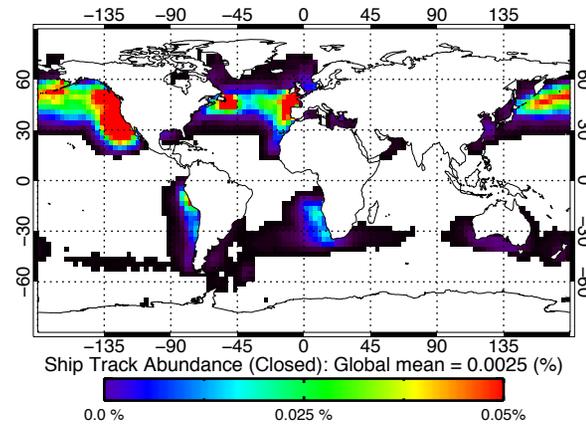
Figure 3.2. (a) Global distributions of closed cellular clouds, (b) open cellular clouds (filled in with black for 0.5° × 0.5° regions having more than 15 ships per day for a and b), (c) ship track formation efficiency parameter, and (d) ship track abundance in closed cellular clouds.

162

3.3. Cloud radiative forcing

In the automated ship track assessment of Campmany et al., [2009], the global abundance of ship tracks was estimated to cover roughly 0.004% of the Earth. Based on the methodology outlined here, the results are consistent, given the error associated with the approach, between the current and former studies. Using this value, a simple estimate of the radiative forcing can thus be calculated by combining equations (1) and (2), and using mean values of $\Delta\alpha$ (0.03) and $F_{SW}^{\downarrow}$ (340 W m^{-2}). The global ship track radiative forcing was approximately -0.4 mW m^{-2}, which was very small compared to the forcing due to the buildup of CO_2 in the atmosphere (2.63 W m^{-2}) and aerosol indirect effects in general (-0.7 ± 1.1 W m^{-2}). Thus, these results imply that ship tracks have a very small influence on the global top of atmosphere radiation budget. However, using the distributions of cloud types, we can assess to what extent the cloud regime influences the response.

By convolving the cloud type distributions the ship traffic database and the cloud albedo susceptibility to aerosol, the ship track radiative forcing was estimated using equations (1) and (2) and displayed for closed (Figure 3.3 top) and open cells (bottom). In the annual mean, the radiative forcing from ship tracks in closed cells was -0.46 mW m^{-2}, a value very similar to the simple "back of the envelope" calculation discussed in the previous paragraph. Despite having a significantly smaller quantity of open cells, the radiative forcing was roughly 3 times larger than the closed cell composite. Because the structure of the spatial distributions was roughly the same, the radiative forcing linearly scaled with the abundance of low-cloud. This probably occurred because the ship track formation efficiencies could not be estimated separately for each regime due to a limited

number of samples. The properties of closed and open cells were thus assumed to follow the mean characteristics of the low-clouds in the region. Nonetheless, this result demonstrates that open cells, which are relatively rare, are an important cloud regime to consider in aerosol-cloud radiative forcing on the global scale.

Table 3.1 lists the annual and seasonal averages of ship track amount and their associated radiative forcing. During boreal summer, the abundance of ship tracks reaches a maximum value, nearly a one-hundredth of a percent, while in winter they become less prevalent (0.0025). Because ship vessel traffic remained roughly constant throughout the year, the area of clouds polluted by ships was largely controlled by the thermodynamics of the atmosphere. During JJA, lower troposphere stability and the fraction of cloud top heights less than 2 km reaches a maximum across the Northern Pacific and Atlantic Oceans, regions having high volumes of shipping. This resulted in the bulk of the ship tracks being observed in the Northern Hemisphere. As a consequence, radiative forcing averages were particularly large during JJA due to the high abundance of ship tracks in regions where the solar insolation peaked during this period.
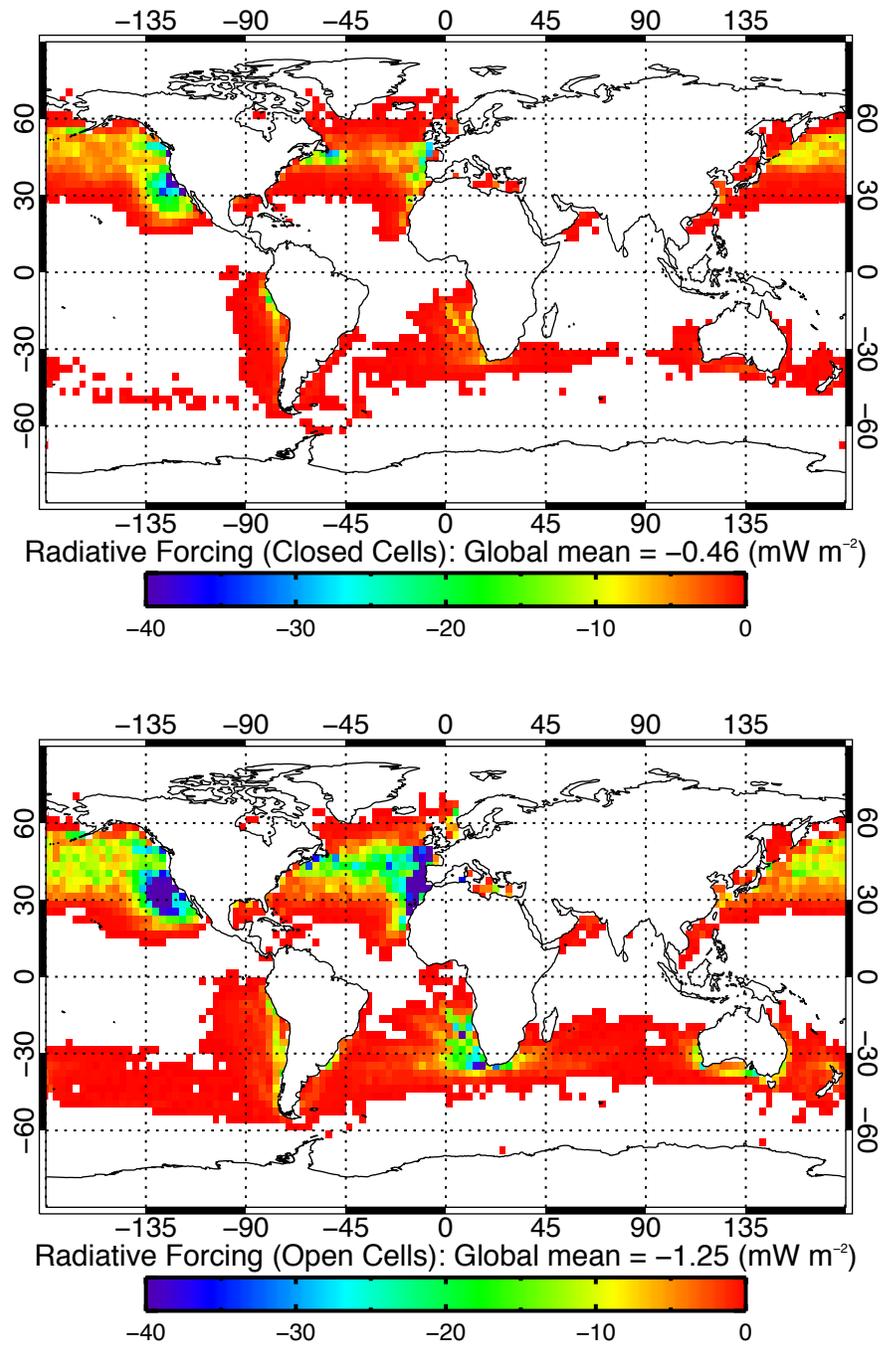
Figure 3.3 (a) Annually averaged ship track cloud radiative forcing in regions containing closed cellular clouds and (b) open cellular clouds.

Table 3.1. Annual global average ship track cloud radiative forcing[a]

Cloud Regime	Ship Track Coverage (%)	Radiative Forcing (mW m^{-2})
	Annual	
Closed Cells	0.0025	−0.46
Open Cells	0.0007	−1.29
	June, July, and August	
Closed Cells	0.0045	−0.99
Open Cells	0.0004	−0.77
	December, January, February	
Closed Cells	0.0011	−0.18
Open Cells	0.0004	−0.65

[a]Listed is the fraction of the globe covered by ship tracks estimated by taking the cosine-weighted sum of areal ship track coverage divided by the sum of the weights. Radiative forcings were calculated for closed cells using a local cloud albedo enhancement of 0.03. Open cells used a value of 0.1.

CHAPTER 4

DISCUSSION AND CONCLUSIONS

To determine the effect of shipping aerosols on climate, two independent studies were conducted. The first study examined the effect of the changing global economy and subsequent changes in shipping on the radiative properties of low clouds. The impact of this change did not manifest as a clear response in the climate system and was probably masked either due to competing aerosol cloud feedbacks or by the large interannual variability in meteorology. The results found here were in general agreement with those of Peters et al., [2011]. Presumably, a substantially larger reduction than 10% in ship traffic across the oceanic basins would be needed to observe a change beyond that due to natural variability.

In the second study, a method was developed to assess the radiative forcing from ship tracks in a variety of cloud types to ascertain their importance in the climate system. Several regions were identified as being highly susceptible, but were often devoid of ships. Such regions may be suitable places to seed boundary layer clouds, as a ship track analog, to produce deliberate cloud brightening and hence, global cooling as proposed in Lathem, [1990]. However, the extent of this cooling remains questionable as either large negative or positive cloud albedo responses can occur, depending on the mesoscale nature of the clouds. Because the number of ships was found to scale with the global radiative forcing, the sensitivity of the response reported here demonstrates that the number of ships would need to increase by 4 orders of magnitude to produce enough ship tracks to have a sizeable effect on the warming due to the buildup of greenhouse gases.

167

Such an increase would also increase the emissions of CO_2. Overall, the response from the ship emissions was small, and the magnitude of the response was in general agreement with the results presented in Schreier et al., [2007] and Campmany et al., [2009]. Aerosol-cloud feedbacks involving the cloud depth and free-tropospheric humidity were ignored in this study, and an average value of the susceptibility response was used for each cloud regime. As a consequence, this approach did not permit aerosol indirect cancellation effects and the results, small as they were, were likely overestimated.

Even if the number of ships was increased, it remains unclear as to whether cooling would actually take place. Results from the ship tracks presented in Part IV reveal that the impact of the particles on cloud albedo do not always enhance reflectivity of closed cellular clouds. Because closed cells are common, and are prone to a mixed cloud albedo response by the effluents from ships, significant cancellation of aerosol indirect effects probably occurs frequently on the climate scale. The extent to which this occurring is an outstanding problem that demands further investigation.

Marine stratocumulus cloud albedo is, in general, highly susceptible to changes in aerosol concentration, and in many oceanic regions these concentrations are greatly enhanced by the emissions from shipping trade routes (by up to 60%). The extent of the aerosol indirect effect from shipping remains highly uncertain and difficult to ascertain due to limits imposed by our ability to observe and model their effects on boundary layer clouds. Previous modeling studies (e.g., [Capaldo et al., 1999], [Lauer et al., 2007]) demonstrate that cloud brightening from shipping could contribute a significant portion of the total anthropogenic aerosol indirect radiative forcing or, as demonstrated by

satellite studies (e.g., [Schreier et al., 2007], [Campmany et al., 2009], and this study), have no impact at all. Because current GCM's poorly simulate the precipitation characteristics of clouds [Stephens, 2010], substantial doubt should be placed on their ability to represent aerosol-cloud feedbacks and hence provide an accurate measurement of the global aerosol indirect forcing. Further quantitative analysis is clearly needed. By using a hierarchy of state-of-the-art models, we may eventually close the gap of this uncertainty and provide bounds on the extent to which shipping influences the albedo of stratocumulus clouds in the climate system.

REFERENCES

Bretherton, C. S., J. McCaa, and H. Grenier, (2004b), A new parameterization for shallow cumulus convection and its application to marine subtropical cloud-topped boundary layers. Part I: Description and 1D results. Mon. Wea. Rev., 132, 864–882.

Campmany, E., R. G. Grainger, S. M. Dean, and A. M. Sayer (2009), Automatic detection of ship tracks in atsr-2 satellite imagery, J. Atmos. Chem. Phys., 9, 1899–1905, doi:10.5194/acp-9-1899-2009.

Capaldo, K., J. J. Corbett, P. Kasibhatla, P. Fischbeck, and S. N. Pandis, (1999), Effects of ship emissions on sulphur cycling and radiative climate forcing over the ocean, Nature, 400, 743-746.

Christensen, M. W., and G. L. Stephens (2011), Microphysical and macrophysical responses of marine stratocumulus polluted by underlying ships: Evidence of cloud deepening, J. Geophys. Res., 116, D03201, doi:10.1029/2010JD014638.

Coakley, J. A., Jr., et al. (2000), The appearance and disappearance of ship tracks on large spatial scales, J. Atmos. Sci., 57, 2765–2778.

Durkee, P. A., R. E. Chartier, A. Brown, E. J. Trehubenko, S. D. Rogerson, C. Skupniewicz, and K. E. Nielsen (2000), Composite ship track characteristics, J. Atmos. Sci., 57, 2542–2553.

Hobbs, P. V., et al. (2000), Emissions from ships with respect to their effects on clouds, J. Atmos. Sci., 57, 2570–2590.

IPCC (2007), Climate Change 2007: The Physical Science Basis. Contribution of Working Group I to the Fourth Assessment Report of the Intergovernmental Panel on Climate Change. [Solomon, S., D. Qin, M. Manning, Z. Chen, M. Marquis, K.B. Averyt, M.Tignor and H.L. Miller (eds.)], Cambridge University Press, Cambridge, United Kingdom and New York, NY, USA.

Klein, S. and D. L. Hartman (1993), The Seasonal Cycle of Low Stratiform Clouds, J. Atmos Sci., 6, 1587-1606

Latham, J. 1990 Control of global warming? Nature 347, 339-340. (DOI:10.1038/347339b0)

Lauer, A., V. Eyring, J. Hendricks, P. Jöckel, and U. Lohmann, (2007), Global model simulations of the impact of ocean-going ships on aerosols, clouds, and the radiation budget, Atmos. Chem. Phys., 7, 5061-5079

Lloyd's Maritime Information System (LMIS), (2002): The Lloyd's Maritime Database [CDROM], Lloyd's Register–Fairplay Ltd., London.

Peters, K., J. Quaas, and H. Grabl, (2011), A search for large-scale effects on ship emissions on clouds and radiation in satellite data, JGR, 116, D24205, doi:10.1029/2011JD016531

Platnick, S and coauthors, (2000), The role of background cloud microphysics in the radiative formation of ship tracks, J. Atmos. Sci., 57, 2607 – 2624

Schreier, M., H. Mannstein, V. Eyring, and H. Bovensmann (2007), Global ship track distribution and radiative forcing from 1 year of aatsr data, Geophys. Res. Lett, 34, L17814, doi:10.1029/2007GL030664.

Sedghi A., (2012), China GDP: how it has changed since 1980, The Guardian Datablog, 23 March.

Stephens, G. L, T. L'Ecuyer, R. Forbes, A. Gettlemen, J.C. Golaz, A. Bodas-Salcedo, K. Suzuki, P. Gabriel, and J. Haynes (2010), Dreary state of precipitation in global models, J. Geophys. Res., 115, D24211, doi:10.1029/2010JD014532.

Travis D. T, Carleton A. M.., and Lauritsen R, (2002). Contrails reduce daily temperature range. Nature 418: 601.

Twomey, S. (1974), Pollution and the planetary albedo, Atmos. Environ., 8, 1251–1256.

White, R. D. (2010), Ports of L.A. and Long Beach are surging back, Los Angeles Times, 30 December.

Wood, R., and D. L. Hartmann (2006), Spatial variability of liquid water path in marine low cloud: The importance of mesoscale cellular convection, J. Clim., 19, 1748–1764.

Wood, R., K. K. Comstock, C. S. Bretherton, C. Cornish, J. Tomlinson, D. R. Collins, and C. Fairall (2008), Open cellular structure in marine stratocumulus sheets, J. Geophys. Res., 113, D12207, doi:10.1029/ 2007JD009371.

PART VI: SUMMARY AND DISCUSSION OF THE DISSERTATION

1.1. Summary of key findings

"Ship tracks have been called the Rosetta Stone of aerosol-cloud-climate interactions because they serve as a striking example of the effects of increased CCN concentrations on the albedo of marine stratiform clouds" [Ackerman et al., 1995]. The goals of this dissertation were two fold: first, to examine processes on the local (cloud) scale that drive the response of aerosol-cloud interactions and, second, to infer how emissions from shipping impact Earth's top of atmosphere radiation budget. Parts II – IV were primarily focused on local scale interactions, while Part V took a global scale observation approach. The main findings from this body of work include the following.

1) Cloud top height measurements of several hundred ship tracks using the Cloud-Aerosol Lidar with Orthogonal Polarization (CALIOP) provided substantial evidence that aerosol plumes emitted from ships elevate the depth of the marine stratocumulus cloud layer. Aerosol-cloud deepening has been identified in simulations performed by Pincus and Baker [1994] and in recent observational studies of volcanic aerosol on trade wind cumulus clouds [Yuan et al., 2011]. However, an elevated cloud layer was only detected in ship tracks when they were detected in an open cell or a collapsed boundary layer convective regime presumably because the temperature inversion was comparatively weak in this cloud regime. One implication for these differences is that the local aerosol indirect radiative forcing was more than five times larger for ship tracks observed in the open cell regime (-59 W m^{-2}) compared to those identified in the closed cell regime (-12 W m^{-2}).

2) Several thousand ship tracks were meticulously logged by hand over the globe to test whether aerosol plumes suppress precipitation. Drizzle rates were calculated using

a path integrated attenuation approach from the measurements obtained from the cloud profiling radar (CPR) on CloudSat. The vast majority of the sampled clouds was considered non-raining (727 ship tracks), probably because the CPR was unable to estimate rain rates when the boundary layer was less than 750 m deep. Of those cases in which drizzle was detected (258 cases), the increased aerosol burden from the ship plume was found to decrease rainfall in 72% of the ship tracks. Most of the cases in which aerosol enhanced the drizzle rates were those belonging to the open cellular cloud regime, a cloud regime that is deficient in cloud condensation nuclei [Wood et al., 2008] and highly susceptible aerosol-cloud brightening.

3) Ship plumes primarily decreased average rain rates through reducing the spatial coverage of precipitation. Although, larger liquid water paths in ship tracks seldom coincided with the reduced cloud water sink from the suppression of precipitation (in less than 20% of cases). The enhancement in cloud top entrainment brought about by the smaller cloud droplets may have been primarily responsible for depleting liquid water paths and drizzle rates in the polluted clouds as suggested by Ackerman et al. [2004]. Differences in precipitation (caused by the plume) had a higher degree of correlation with the changes in liquid water path compared to the changes in droplet size. This suggests that macrophysical (liquid water path and cloud depth) changes play a significant role in the direction and magnitude of the drizzle rate response in stratocumulus clouds.

4) Processes governing the macrophysical and cloud albedo responses of marine stratocumulus were investigated by separating the response by those ship tracks in which cloud brightening and cloud dimming occurred. The response was found to depend mostly on the relative humidity in the free troposphere, depth of the marine boundary

layer, and the size of the cloud droplets and optical thicknesses of the clouds. Aerosol-cloud dimming tended to occur when the free-troposphere was sufficiently dry. This observation is consistent with the in-situ measurements of four ship tracks sampled during the Eastern Pacific Emitted Aerosol Cloud Experiment (E-PEACE) and in the large eddy simulations reported in Ackerman et al., [2004] and Xue et al., [2008].

Four cloud regimes were examined in detail: the collapsed marine boundary layer, open cells, shallow closed cells, and thick closed cells. These regimes encompassed 70% of the ship track cases. Cloud brightening was always found to occur in collapsed boundary layers and in open cellular cloud systems. Polluted clouds in the closed cell regime were likely to be less reflective than unpolluted clouds, particularly when the precipitation was detected. Based on simulations by Liu et al., [2000], it is hypothesized that when the cloud layer becomes decoupled from surface moisture, polluted clouds are prone to significant losses in liquid water path.

5) The global economic recession that took place in 2008 provided an excellent opportunity to examine the effects of the changes in ship traffic on the microphysical and macrophysical responses of low-level clouds across the global oceans. Across the north Pacific and north Atlantic, a 10% decrease in shipping was reported to occur between 2007 and 2009. As a consequence, vast reductions in sulfur emissions (about 200 KT) occurred, however, the effect had no discernable impact on the average radiative properties of the low-level clouds. In the southern Atlantic Ocean, where shipping increased, significant cloud optical thickening was observed off the coast of Africa where the radiative forcing was estimated to be approximately -1.8 W m^{-2} between 2007 and 2009. Presumably the extent of this forcing was related to shipping, however this result

remains shrouded with uncertainty. The radiative signature of the changes in shipping could have been washed out by the interannual climate variability and the variability in the background aerosol concentrations between 2007 and 2009. Therefore, a modeling study focusing on this time period is recommended to isolate the radiative response from the changes in meteorology and background aerosol concentrations.

6) In the second approach, a method was developed to assess the radiative forcing from "ship tracks" by convolving the lanes of densely populated ships onto the global distributions of closed and open cells. Closed cells were observed nearly 2.5 times more frequently than open cells. Despite the smaller abundance of open cells, a large fraction of the radiative forcing by shipping was claimed by this regime. On the whole, the global radiative forcing from ship tracks was tiny (approximately -0.45 mW m^{-2}) compared to the forcing associated with the buildup of atmospheric CO_2. The results demonstrate that aerosol effects in open cellular cloud regimes probably contribute a great deal to the global aerosol indirect forcing given that they are highly susceptible to aerosol-cloud brightening.

1.2. Pathways for future research

The results from this body of work open the door to many potential research pathways. Much can still be learned from analyzing ship tracks at the local cloud scale. Data from past in situ research campaigns has been underutilized and would enable testing of the various hypotheses put forward by the work presented here. The data could elucidate processes related to ship track formation and the role of mesoscale convection, free-tropospheric humidity, and boundary layer coupling on the cloud albedo and

precipitation responses in ship tracks. The recent success of the Eastern Pacific Emitted

Aerosol Cloud Experiment (E-PEACE) provided evidence for some of these processes;

however, the results were based on four ship track cases. Many more cases are likely

needed to characterize these responses in ship tracks. An expansion of this analysis could

be achieved by incorporating data from past field campaigns, such as the Monterey Area

Ship Track (MAST) experiment [Durkee et al., 2000]. The MAST experiment includes in

situ measurements of dozens of individual ship tracks using a comprehensive payload of

state-of-the-art aerosol and cloud instrumentation on multiple research platforms. Phillip

Durkee, principal investigator of MAST, has expressed an interest in making this dataset

available.

In a recent workshop held by the Keck Institute for Space Studies, major gaps in

our understanding of low-cloud feedbacks were examined. One of the key questions

posed was is it possible to brighten and/or increase the abundance of low-level clouds

significantly enough to offset the global radiative forcing associated with increasing

concentrations of greenhouse gases? The ability to deliberately brighten low-level clouds

through solar radiation management (SRM) strategies ultimately depends on two factors:

whether the cloud is receptive to the aerosol plume and if an aerosol-cloud-brightening

effect will actually occur. Based on the observations of the ship tracks presented here,

substantial doubt should be placed on the ability to brighten low clouds due to numerous

cloud feedbacks that can mute or possibly even cancel the cloud brightening response.

During E-PEACE, the effluents from 45 ships were sampled and, surprisingly only four

of plumes interacted with the overlying cloud layer. This suggests that boundary layer

clouds are difficult to seed and, may not be very receptive to producing ship tracks by the

emissions from ships. Based on the simulations from Liu et al., [2000], the response is probably related to the degree of cloud-surface coupling. Measurements from this campaign therefore offer an opportunity to investigate the atmospheric conditions that promote the direct contact of the aerosol plume with the cloud layer.

Occasionally, vast regions of stratocumulus are flooded with ship tracks where as much as ten percent of a 1000 km^2 region can be covered by them (e.g., see Figure 3.7 in Part IV). Under these unique conditions, the emissions from ships produce several distinct types of ship tracks, the net effect of which is increased albedo, cloudiness, and an aerosol indirect forcing that can be on the order of several watts per square meter [Schreier et al., 2006]. A thorough study analyzing the spatiotemporal frequency of these high-density ship track events has yet to be performed on the global scale. These events are commonly associated with the clouds in a collapsed boundary layer. By utilizing the large ensembles of ship tracks in the satellite data presented here and those used in Segrin et al., [2007] (over 4,000 ship tracks were logged by hand), we may begin to understand the degree in which the large-scale meteorology is correlated to the collapse of the marine boundary layer. Global distributions of these cloud systems and the closed cell clouds that have an can have an opposite aerosol-brightening influence may provide insight into efficacy of SRM strategies to deliberately brighten low clouds.

The Marine Environment Protection Committee (MEPC) of the International Maritime Organization (IMO) recently approved regulations to progressively reduce harmful emissions from ships over the next couple of decades. How these changes will manifest in the Earth's radiation budget remains highly uncertain. Modeling studies (e.g., [Capaldo et al., 1999], [Lauer et al., 2007]) demonstrate that cloud brightening from

shipping could contribute a significant portion of the total anthropogenic aerosol indirect radiative forcing or, as demonstrated by satellite studies (e.g., [Schreier et al., 2007], [Campmany et al., 2009], [Peters et al., 2011]), have no impact at all. The recent global economic recession of 2008 provides a test bed to analyze the radiative response associated with the reduction in shipping. While A-train observations offer a glimpse of the magnitude of this response, it was difficult to isolate the interannual climate variability that may have masked the shipping signal. Examining the response using a state-of-the-art 3D chemical transport model would provide a way to tease out the radiative signature from the changes in shipping. Combining A-train observations with an independent modeling study could thus improve radiative forcing estimates and provide projections for the potential effects of the changing emission standards in the decades to come.

REFERENCES

Ackerman, A. S., O. B. Toon, and P. V. Hobbs (1995), Numerical modeling of ship tracks produced by injection of cloud condensation nuclei into marine stratiform clouds, J. Geophys. Res., 100, 7121–7133.

Ackerman, A. S., M. P. Kirkpatrck, D. E. Stevens, and O. B. Toon (2004), The impact of humidity above stratiform clouds on indirect aerosol climate forcing, Nature, 432, 1014–1017.

Albrecht, B. A. (1989), Aerosols, cloud microphysics, and fractional cloudiness, Science, 245, 1227–1230.

Campmany, E., R. G. Grainger, S. M. Dean, and A. M. Sayer (2009), Automatic detection of ship tracks in atsr-2 satellite imagery, J. Atmos. Chem. Phys., 9, 1899–1905, doi:10.5194/acp-9-1899-2009.

Capaldo, K., J. J. Corbett, P. Kasibhatla, P. Fischbeck, and S. N. Pandis, (1999), Effects of ship emissions on sulphur cycling and radiative climate forcing over the ocean, Nature, 400, 743-746.

Durkee, P. A., K. J. Noone, and R. T. Bluth (2000a), The Monterey area ship track experiment, J. Atmos. Sci., 57, 2523–2541.

Lauer, A., V. Eyring, J. Hendricks, P. Jöckel, and U. Lohmann, (2007), Global model simulations of the impact of ocean-going ships on aerosols, clouds, and the radiation budget, Atmos. Chem. Phys., 7, 5061-5079

Liu, Q., Y. L. Kogan, and D. K. Lilly (2000), Modeling of ship effluent transport and its sensitivity to boundary layer structure, J. Atmos. Sci., 57, 2779–2791.

Peters, K., J. Quaas, and H. Grabl, (2011), A search for large-scale effects on ship emissions on clouds and radiation in satellite data, JGR, 116, D24205, doi:10.1029/2011JD016531

Pincus, R., and M. B. Baker (1994), Effect of precipitation on the albedo susceptibility of clouds in the marine boundary layer, Nature, 372, 250–252.

Schreier, M., A. A. Kokhanovsky, V. Eyring, L. Bugliaro, H. Mannstein, B. Mayer, H. Bovensmann, and J. P. Burrows (2006), Impact of ship emissions on the microphysical, optical and radiative properties of marine stratus: a case study, Atmos. Chem. Phys, 6, 4925—4942.

Schreier, M., H. Mannstein, V. Eyring, and H. Bovensmann (2007), Global ship track

distribution and radiative forcing from 1 year of AATSR data, Geophys. Res. Lett., 34, L17814, doi:10.1029/2007GL030664.

Segrin, M. S., J. A. Coakley Jr., and W. R. Tahnk (2007), MODIS observations of ship tracks in summertime stratus off the west coast of the United States, J. Atmos. Sci., 64, 4330–4345. Stephens, G. L. (1978), Radiation profiles in extended water clouds. Part II: Parameterization schemes, J. Atmos. Sci., 35, 2123–2132.

Wood, R., K. K. Comstock, C. S. Bretherton, C. Cornish, J. Tomlinson, D. R. Collins, and C. Fairall (2008), Open cellular structure in marine stratocumulus sheets, J. Geophys. Res., 113, D12207, doi:10.1029/ 2007JD009371.

Xue, H., G. Feingold, and B. Stevens (2008), Aerosol effects on clouds, precipitation, and the organization of shallow cumulus convection, J. Atmos. Sci., 65, 392–406.

Yuan, T., Remer, L. A., and Yu, H. (2011): Microphysical, macrophysical and radiative signatures of volcanic aerosols in trade wind cumulus observed by the A-Train, Atmos. Chem. Phys. Discuss., 11, 6415-6455, doi:10.5194/acpd-11-6415-2011.